Stacking of various Flow-Cells for the CO_2 -to-CO Electrolysis

Stapeln verschiedener Flusszellen für die CO_2 -zu-CO Elektrolyse

Von der Fakultät für Mathematik, Informatik und Naturwissenschaften der RWTH Aachen University zur Erlangung des akademischen Grades eines Doktors der Ingenieurwissenschaften genehmigte Dissertation

vorgelegt von

Maximilian Quentmeier, M.Sc.

aus Saarbrücken, Germany

Berichter: Univ.-Prof. Dr. rer. nat. Rüdiger-Albert Eichel

Univ.-Prof. Dr.-Ing. Matthias Wessling

Tag der mündlichen Prüfung: 24.01.2025

Diese Dissertation ist auf den Internetseiten der Universitätsbibliothek online verfügbar.

Eidesstattliche Erklärung

Ich, Maximilian Quentmeier erkläre hiermit, dass diese Dissertation und die darin dargelegten Inhalte die eigenen sind und selbstständig, als Ergebnis der eigenen originären Forschung, generiert wurden.

Hiermit erkläre ich an Eides statt

1. Diese Arbeit wurde vollständig oder größtenteils in der Phase als Doktorand dieser Fakultät und Universität angefertigt;

2. Sofern irgendein Bestandteil dieser Dissertation zuvor für einen akademischen Abschluss oder eine andere Qualifikation an dieser oder einer anderen Institution verwendet wurde, wurde dies klar angezeigt;

3. Wenn immer andere eigene- oder Veröffentlichungen Dritter herangezogen wurden, wurden diese klar benannt;

4. Wenn aus anderen eigenen- oder Veröffentlichungen Dritter zitiert wurde, wurde stets die Quelle hierfür angegeben. Diese Dissertation ist vollständig meine eigene Arbeit, mit der Ausnahme solcher Zitate;

5. Alle wesentlichen Quellen von Unterstützung wurden benannt;

6. Wenn immer ein Teil dieser Dissertation auf der Zusammenarbeit mit anderen basiert, wurde von mir klar gekennzeichnet, was von anderen und was von mir selbst erarbeitet wurde;

7. Ein Teil oder Teile dieser Arbeit wurden zuvor veröffentlicht und zwar in:

Toward a stackable CO_2-to-CO electrolyzer cell design - impact of media flow optimization,

by Maximilian Quentmeier, Bernhard Schmid, Hermann Tempel, Hans Kungl and Rüdiger-A. Eichel published in *ACS Sustainable Chemistry & Engineering*, 11(2):679-688, (2023),

Modular CO_2 -to-CO Electrolysis Short-Stack Design – Impact of Temperature Gradients and Insights into Position-Dependent Cell Behavior,

by Maximilian Quentmeier, Bernhard Schmid, Hermann Tempel, and Rüdiger-A. Eichel published in *ACS Sustainable Chemistry & Engineering* , 12:3876-3885, (2024),

$\overline{Aachen, January 2025}$
Maximilian Quentmeier

Publications

Parts of this thesis are based on the following publications:

- **Toward a stackable CO_2-to-CO electrolyzer cell design - impact of media flow optimization**, Maximilian Quentmeier, Bernhard Schmid, Hermann Tempel, Hans Kungl and Rüdiger-A. Eichel, *ACS Sustainable Chemistry & Engineering*, **2023**, *11(2)*, 679-688.[1]

  Contributions: M. Quentmeier is the main contributor to this publication. He performed the literature review and created the graphs and tables. Schematic illustrations were designed in collaboration with B. Schmid and Sebastian C. Lehmann. M. Quentmeier wrote the text of the paper with contributions from all authors. This publication was written in consultation with B. Schmid.

  In this thesis, Chapters 3.5, 4.2, and 4.3 are based on this publication.

- **Modular CO_2-to-CO Electrolysis Short-Stack Design – Impact of Temperature Gradients and Insights into Position-Dependent Cell Behavior**, Maximilian Quentmeier, Bernhard Schmid, Hermann Tempel, and Rüdiger-A. Eichel, *ACS Sustainable Chemistry & Engineering*, **2024**, *12*, 3876-3885. [2]

  Contributions: M. Quentmeier is the main contributor to this publication. He performed the literature review and created the graphs and tables. Michael Schatz performed NMR analysis, all other experiments were performed by M. Quentmeier. M. Quentmeier wrote the text of the paper with contributions from all authors. This publication was written in consultation with B. Schmid.

In this thesis, Chapters 3.5, 4.3, and 4.4 are based on this publication.

Conference Contributions

- Poster: **CO_2-to-CO GDE-Flowcell From Lab-Test-Cell to Stack**, Maximilian Quentmeier, Bernhard Schmid, Hermann Tempel, Hans Kungl and Rüdiger-A. Eichel, *Electrochemistry 2022, Berlin, Germany*, **27 Sep 2022 - 30 Sep 2022.**
- Presentation: **Modification of media flow compartments in CO_2-to-CO electrolyzer**, Maximilian Quentmeier, Bernhard Schmid, Hermann Tempel, Hans Kungl and Rüdiger-A. Eichel, *243rd ECS Meeting, Boston, USA,* **28 May 2023 - 2 Jun 2023.**

Contents

Abstract xi

Kurzfassung xiii

Acknowledgements xvii

1 Introduction 1

2 Literature Discussion 5

2.1 CO_2 Electrolysis 5

2.1.1 Products 6

2.2 Process Evaluation 7

2.2.1 Selectivity 8

2.2.2 Current Density 8

2.2.3 Cell Voltage 9

2.2.4 Energy Efficiency 10

2.2.5 Electrical Power Consumption 10

2.3 Technological Readiness 11

2.4 CO_2 -to-CO Electrolysis 12

2.4.1 Application of CO_2 -to-CO Electrolysis 12

2.4.2 Cathodic and Anodic Reactions 13

2.5 Flow-Cells for CO_2 -to-CO Electrolysis 15

2.5.1 Gas-Diffusion-Electrode 16

2.5.2 Flow-Cell Architectures 16

2.5.3 Ion Exchange Membranes in Flow-Cells 18

2.6 Scaling in CO_2 -to-CO Electrolysis 25
2.6.1 Increasing Size of Single-Cells 26
2.6.2 Stacking of Flow-Cells 29

3 Materials and Methods 33
3.1 Cell Components and Electrolytes 33
3.2 Materials for Test Benches 34
3.3 Analytical Materials and Methods 35
3.4 Feed Gas Parameter 36
3.5 Experimental Protocols 37

4 Results and Discussion 43
4.1 Assessing Various CO_2 -to-CO Flow-Cell Concepts 43
4.2 Impact of Flow-Fields in GDE-Flow-Cell 53
4.3 Stacking of GDE-Flow-Cell 71
4.4 Modular Short-Stack Design for MEAs 79
4.5 Extending the Role of End- and Bipolar-Plates 97

5 Conclusion 109

A Supplementary Information and Results for GDE-Flow-Cell with PEM 113

B Supplementary Information and Results for Modular Short-Stack Design for MEAs 119

C Overview of Flow-Cell Performances 123

Abbreviations and Symbols 128

Bibliography 131

Abstract

Based on the highly selective and stable electrocatalyst Ag, the aqueous CO_2-to-CO electrolysis has emerged as a promising prospect for replacing fossil resources in the production chain of various chemical products. However, despite encouraging performances of single flow-cells in lab-scale size operating with gas-diffusion-electrodes (GDEs) at industrially relevant conditions, the discussion around the scaling of CO_2-to-CO electrolysis systems is underrepresented. In this work, studies are performed concerning the stacking of the most promising flow-cell concepts, which is a key enabling step in scaling electrolysis processes. In an initial study, a GDE-flow-cell with a proton exchange membrane and a flow-cell with a membrane electrode assembly (MEA) containing an anion exchange membrane (AEM) were singled out as the most promising cell designs. To the first one mentioned, performance-enhancing modifications on the media flow compartments were carried out. A gas flow-field was implemented, leading to an enhanced selectivity at diluted feed gas supply. An ionically conductive spacer was introduced in the catholyte chamber, which enhanced the process stability. To demonstrate, that the combination of the two modifications results in stackability, a two-cell short-stack is tested. While a general stackability of the concept is demonstrated, a limitation of the stack design regarding the investigation of stack-specific challenges becomes evident. Building upon the experience gained, a modular short-stack design and its operation as a three-cell short-stack with the MEAs is presented. Due to temperature effects, the short-stack surpassed its equivalent single-cell in cell voltage. Benefiting from the modular characteristic, temperature gradients, which led to a

position-dependent behavior of the individual cells in the stack, could be observed. Furthermore, the presented design enabled the quantification of shunt currents, which were identified to be negligible in the examined system. Once again, the modularity was exploited in a study concerning the anodic catalyst surface area, which was increased by the implementation of catalyst-coated flow-fields. While the functionality of two-material Bipolar-Plates was demonstrated, the impact of the catalyst surface increase was considered to be negligible.

Kurzfassung

Basierend auf dem stabilen und selektiven Katalysator Ag, hat sich die CO_2-zu-CO Elektrolyse zu einem vielversprechenden Prozess entwickelt, um fossile Ressourcen in Herstellungsverfahren von chemischen Produkten zu ersetzen. Jedoch ist die Skalierung des Prozesses trotz der guten Leistungen von einzelnen Flusszellen in Labormaßstab, die mit Gas-Diffusions-Elektroden (GDEs) unter industriell relevanten Bedingungen betrieben werden, bisher wenig betrachtet worden. Ein Schlüsselschritt in der Skalierung ist das Stapeln der einzelnen Zellen zu sogenannten Stacks. In dieser Arbeit wird das Stapeln verschiedener Flusszellkonzepte betrachtet. In einer ersten Studie wird eine GDE-Flusszelle mit einer Protonaustauschmembran, sowie eine Flusszelle mit einer Membrane-Electrode-Assembly (MEA), die mit einer Anionaustauschmembran aufgebaut ist, als vielversprechendste Konzepte identifiziert. Für das erstgenannte Konzept werden Räume der Stoffströme dahingehend modifiziert, dass sich ein stapelbares Design ergibt. Im Gasraum wird ein Flussfeld und im Elektrolytraum ein ionisch leitfähiger Spacer implementiert. Durch das Flussfeld wird eine erhöhte Selektivität des Prozesses bei verdünnter CO_2 Gaszufuhr erzeugt, während der Spacer den Prozess stabilisiert. Folglich zeigt sich durch die Modifikationen eine Leistungssteigerung der Zelle. Um zu zeigen, dass sich aus der Kombination der beiden Modifikationen auch eine Stapelbarkeit ergibt, wird im Anschluss ein zwei-Zellen Stack getestet. Während eine generelle Stabelbarkeit des Konzepts nachgewiesenwerden kann, wird eine Limitierung des Stack Designs hinsichtlich der Untersuchung von Stack spezifischen Gegebenheiten deutlich. Aufbauend auf den

gewonnenen Erkenntnissen, wird ein modulares Stack Konzept entwickelt und mit drei MEA Zellen betrieben. In Versuchen zeigt sich im Vergleich zu der Einzelzelle eine geringere Spannung der Zellen im Stack. Diese Leistungssteigerung ist die auf eine erhöhte Temperaturentwicklung im Stack zurückzuführen. Außerdem wird eine Abhängigkeit der Leistung zu der Position der individuellen Zellen im Stack deutlich. Durch die Ausschöpfung der modularen Charakteristik des Designs lässt sich diese Abhängigkeit auf Temperatur Gradienten innerhalb des Stacks zurückführen. Darüber hinaus ermöglicht das Design die Quantifizierung von Streuströmen, die für das untersuchte System als vernachlässigbar befunden werden konnten. Der Wert des modularen Stacks zeigt sich weiterhin in einer Studie, in der die Katalysatorfläche auf der Anoden Seite durch beschichtete End- und Bipolar-Platten erhöht wird. Während die generelle Funktionalität von Bipolar-Platten, die aus zwei verschiedenen Materialen bestehen, gezeigt wird, so verdeutlicht die Studie, dass die Erhöhung der Katalysatorfläche über die Platten zu gering ist um die Leistung der Zellen in Bezug auf die Spannung zu steigern.

Acknowledgements

Im Rahmen meiner Doktorarbeit und der vergangenen vier Jahre möchte ich mich herzlich bei all denjenigen bedanken, die mich sowohl beruflich als auch privat unterstützt haben. Ohne Ihre Hilfe wäre der erfolgreiche Abschluss dieser Arbeit nicht möglich gewesen.
Zunächst gilt mein besonderer Dank Professor Eichel für die Möglichkeit, am IEK-9 zu promovieren. Zudem möchte ich Bernhard Schmid für seine wertvolle Betreuung und die ehrliche Unterstützung sowie den Input in allen fachlichen Fragen danken.
Ein weiterer Dank geht an das gesamte Team des IEK-9, besonders an meine Kollegen und Kolleginnen aus meinem Büro sowie den angrenzenden Büros für die vielen anregenden fachlichen und persönlichen Diskussionen. Hier möchte ich besonders Michael Schatz und Julian Borowec hervorheben, deren Freundschaft mir nicht nur während meiner Zeit am IEK-9, sondern auch schon während meines Studiums und hoffentlich auch in der Zukunft eine wichtige Stütze war.
Ich danke auch meinen ehemaligen Mitbewohnern, die es immer geschafft haben unzählige schöne Augenblicke zu kreieren, um anstrengende Zeiten zu überstehen.
Ein großes Dankeschön geht an meine Familie, die mir stets ihr Vertrauen geschenkt und meine Ausbildung gefördert hat.
Abschließend möchte ich Clara danken, die mir auf den letzten Metern meiner Promotion beigestanden und mich auf Kurs gehalten hat.

Chapter 1

Introduction

Driven by the pressing need to mitigate climate change, a shift toward a circular carbon economy is emerging, encompassing the capture of the greenhouse gas CO_2, its storage, and its utilization as a carbon source. The latter is particularly interesting for the chemical industry, which traditionally relies on carbon-based products from fossil resources. Contemplated is a transition to electrified chemical production processes harnessing renewable energy sources and simultaneously utilizing CO_2 as a feed-stock for carbon-based products.[3–5] The core concept evolves around the CO_2 electrolysis, incorporating the electrochemical CO_2 reduction reaction, which enables the production of carbon-based intermediate chemicals from CO_2 with electrical energy. Considering renewable energy as the electrical energy source for this process, it can be anticipated that the carbon intensity of the end products formed by the intermediate chemicals is reduced. Through the storage of these products or their utilization in everyday applications, the carbon cycle can be closed and CO_2 emissions can be mitigated.[6–9]

This work focuses on the CO_2-to-CO electrolysis in aqueous media at ambient conditions, which is further advanced compared to other CO_2 electrolysis processes. Based on the development of materials and cell components including membranes, catalysts, and electrodes, stable and continuous operation of the CO_2-to-CO electrolysis in so-called flow cells

is possible. Nonetheless, most discussions on CO_2-to-CO electrolysis in the literature evolve around single-cells in lab-scale size.[8–11] In the study presented here, the transition from single-cell to stack assembly, a key enabling step toward industrial application, is to be investigated and discussed. For this purpose, promising electrolyzer concepts discussed in the literature need to be identified. In a shared set-up, these concepts are to be assessed. On this basis, promising prospects are to be highlighted and stacked. The objective here is to gain insights into the stacking process, the influence of the various cell components required for the stacking, and the behavior and interaction of the individual cells in the stack.

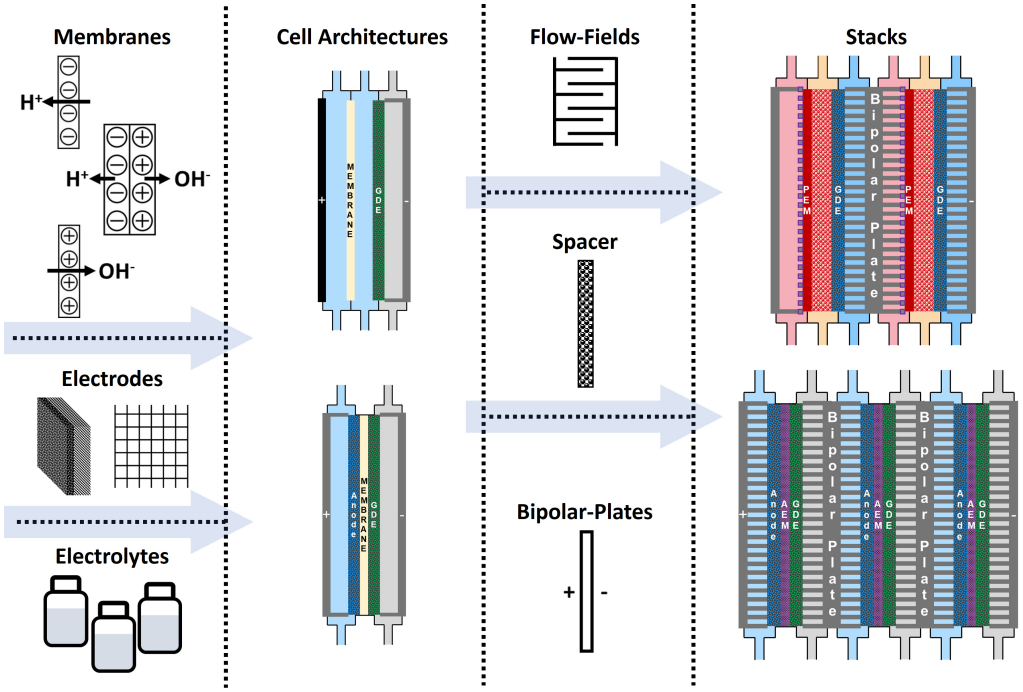

Figure 1.1: Objective of the thesis; Identification of potential CO_2-to-CO electrolyzer architectures for stacking and consecutive stack development.

Chapter 2

Literature Discussion

2.1 CO_2 Electrolysis

The CO_2 electrolysis is an electrocatalytic process based on the electrochemical CO_2 reduction reaction, which has already been discovered in the 19th century. Still, the CO_2 electrolysis is a rather young technology that has received increasing attention over the last decades.[12,13] The basis of the growing interest is the rising CO_2 level in the atmosphere and the consequence of global warming. As an act to mitigate CO_2 emission, the CO_2 electrolysis can be a key enabling step toward an economy with a closed carbon cycle. This entails using harvested CO_2 as a feedstock to produce value-added chemicals.[3,14,15] In the CO_2 electrolysis, the underlying electrochemical CO_2 reduction reaction for the production of platform chemicals is performed at the cathode of an electrochemical cell. Depending on the catalyst, which is applied on the cathode, various gaseous as well as different liquid products can be produced (Figure 2.1).[16]

2.1.1 Products

In the spectrum of possible products are CO, formate, and formic acid, as well as various multicarbon products. Non-noble heavy metals, for instance, indium, lead, and cadmium are active catalysts for the reduction of CO_2 to formic acid.[17,18] Electrochemical cells containing Au, Ag, and Zn as catalysts have demonstrated selective performances for the CO_2 of reduction to CO.[19,20] With Cu, CO is formed as an intermediate, and due to the intermediate binding energy of Cu for CO, various multicarbons such as ethylene, and different alcohols can be produced (Figure 2.1).[16,21–23]

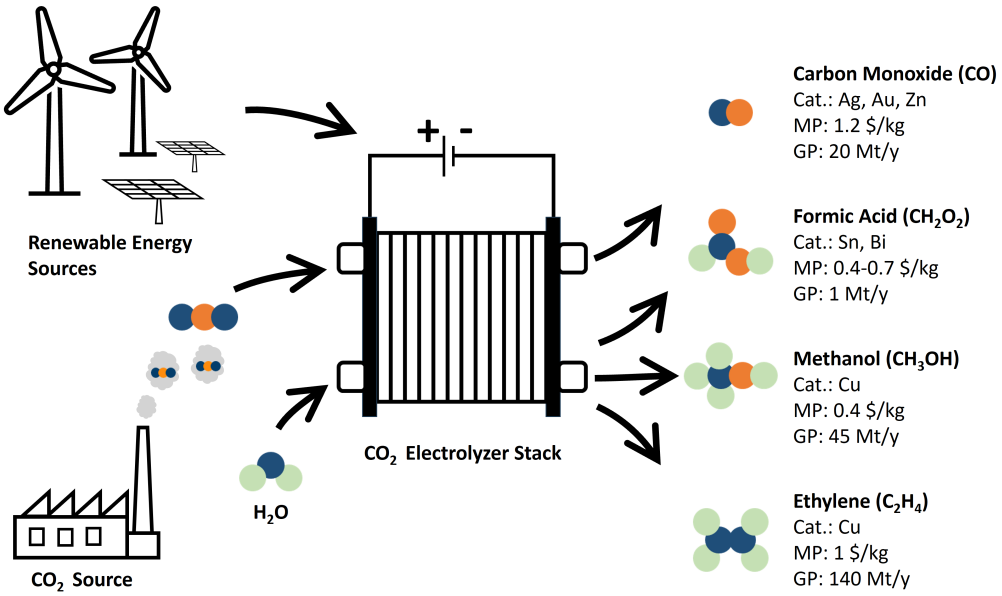

Figure 2.1: Overview of CO_2 electrolysis process in aqueous media including possible products, required catalysts for the specific product (Cat.), market price of the product (MP) and global annual production (GP). MP and GP are estimated values aggregated from O'Brien et al.[24] and Endrődi et al.[25].

The ability to produce different products demonstrates the variability and the potential of the CO_2 electrolysis. However, the different products impose distinct requirements on the electrolyzer as well as on the periphery of the process, leading to a multitude of considerable systems

for the various products.[25,26] So far no cell concept has been presented, that universally leads to a valuable process for all applications. Therefore, the development of a mature process around the CO_2 reduction reaction is fragmented into branches, which focus on different catalysts and products.[27] Even for the same products different systems with various electrolytes, membranes, electrodes, and cell architectures have been proposed, each with unique benefits and limitations.[25,28]

In terms of the different processes and various electrolyzer designs for the CO_2 electrolysis, performance indicators must be defined to compare the performances.[29]

2.2 Process Evaluation

The area of the cell components determines electrolysis processes. This implies, that the yield achieved by a specific active surface area over time is fundamental to evaluate the process. The thickness of the cells in contrast determines the space-time yield. In general, thinner cells lead to an increase in energy efficiency and thus to higher space-time yield. It must be emphasized, that the space-time yield and the yield of the active cell area over time are primarily influenced by whether or not the process can be carried out continuously and over a long period of time.[7,25] To achieve sufficient yields, continuously operating flow-cells are required containing robust components whose properties do not change when operating over a long period of time.[8]

A further aspect of process evaluation is the educt loss. Not all CO_2 entering the cell is converted to the desired product. A significant part is consumed in side reactions or does not participate in the reactions at all and exits the cell in the product gas flow. Thereby, the product gas is diluted.[30] The recovery of CO_2 from product gas flow or other media flow streams needs to be considered, specifically since the price for CO_2-capture from air (100-200 \$/t) or even from concentrated sources such as power and chemical plants (40-70 \$/t) is still high.[31] Minimizing the

educt loss increases the value of the process, but it is oftentimes accompanied by an increase in costs due to the addition of downstream processes or more complex and potentially less energy-efficient cell designs.[31]

Overall, the value of the process is not only determined by the economic value of the product but also by the concentration of the product stream, the energy consumption, and the educt consumption.[7,8,25,32] It is therefore crucial to describe the performance of an electrolyzer with well-defined figures of merit. For the CO_2 electrolysis, different figures of merit that are described in the following have been established.

2.2.1 Selectivity

The selectivity of the process characterizes its ability to prioritize the formation of the desired product while suppressing the formation of undesired side products. The selectivity can be described via the Faraday Efficiency (FE), which is calculated by the number of electrons (z) participating in the reaction, the molar flow rate of the product ($\dot{n}_{i_{out}}$), the Faraday Constant (F = 96487 C/mol) and the current applied to the cell I (Equation 2.1). The selectivity is therefore normalized to the applied charge.[33]

$$FE(i) = \frac{z \cdot \dot{n}_{i_{out}} \cdot F}{I} \cdot 100\,\% \tag{2.1}$$

2.2.2 Current Density

The current density (j) describes the electron flux per active cell area. High current densities are essential to reduce the size of the scaled electrolyzer, and the investment costs. For the CO_2 electrolysis, $j \geq 100\,\mathrm{mA/cm^2}$ are described to be industrially relevant.[6]

2.2.3 Cell Voltage

The cell voltage (U_{Cell}) can be described as the sum of the reversible voltage (E), the activation overpotential (U_{act}), the mass transport overpotential (U_{trans}), and the ohmic overpotential (U_{ohm}) (Equation 2.2).[34–36]

$$U_{Cell} = E + U_{act} + U_{trans} + U_{ohm} \tag{2.2}$$

E is the theoretical voltage that is required by the electrolyzer to drive the reactions and can be determined either with the application of the Gibb´s Free Energy (ΔG) (Equation 2.3) or by the Nernst equation (Equation 2.4).[35,36] Following the Nernst-Equation, E is calculated via the reversible cell potential at standard temperature and pressure (E^0_{rev}), the average temperature of the cell (T), the ideal gas constant (R = 8.3144 [$J/mol \cdot K$]), F, z, and the ratio of the concentration of the oxidized to the reduces species (c_{Ox}, c_{Red}).[37]

$$E = \frac{\Delta G}{z \cdot F} \tag{2.3}$$

$$E = E^0 + \frac{R \cdot T}{F \cdot z} \cdot ln \frac{[c_{Ox}]}{[c_{Red}]} \tag{2.4}$$

The activation overpotential defines the potential loss from the electrochemical reactions which is required to start the reactions. It is highly influenced by operating temperature, catalyst properties, and electrode morphology. With the Butler-Volmer Equation (Equation 2.5, 2.6, 2.7), which describes the dependency of the current on the voltage in the electrode, U_{act} can be calculated. In the Butler-Volmer equation, the activation overpotentials of the cathode ($U_{act,c}$) and the anode ($U_{act,a}$) are calculated by the current density (j), the exchange current density of the electrode (j_c, j_a), the temperature at the electrode (T_c, T_a), and the charge transfer coefficient (α_c, α_a).[35,36]

$$U_{act} = U_{act,a} + U_{act,c} \tag{2.5}$$

$$U_{act,a} = \frac{R \cdot T_a}{\alpha_a \cdot F} \cdot sinh^{-1}(\frac{j}{2 \cdot j_{0,a}}) \tag{2.6}$$

$$U_{act,c} = \frac{R \cdot T_c}{\alpha_c \cdot F} \cdot sinh^{-1}(\frac{j}{2 \cdot j_{0,c}}) \tag{2.7}$$

The mass transport overpotential is related to the transport of educts to, and the removal of products from the catalytic active sites. The blockage of these sites for instance can lead to voltage loss.[35,36]

The ohmic overpotentials are caused by the membrane resistance, the resistance of current collectors and bipolar plates, the interface resistance between electrode and membrane, and the resistance of the electrolyte.[35,36]

2.2.4 Energy Efficiency

The electrical energy input efficiency (ϵ) describes the efficiency of converting electric energy to chemical energy stored in the respective product. ϵ is calculated via the ΔG, the FE of the product, z, F and U_{Cell} (Equation 2.8).[34,38]

$$\epsilon = \frac{\Delta G \cdot FE}{U_{Cell} \cdot z \cdot F} \tag{2.8}$$

2.2.5 Electrical Power Consumption

The electrical power consumption (EPC) describes the electrical power that is needed to produce one Nm^3 of the desired product. The EPC is required to estimate cooling or heating needs and to evaluate the power supply. It is calculated by U_{Cell}, F, z, the FE of the desired product, and the molar volume of an ideal gas under standard conditions ($V_m = 24.47$ [l/mol]) (Equation 2.9). The EPC is therefore inversely proportional to the energy efficiency (Equation 2.8).[29]

$$\text{EPC} = \frac{U_{Cell} \cdot z \cdot F}{FE \cdot V_m} \tag{2.9}$$

2.3 Technological Readiness

In terms of the wide product spectrum, the CO_2 electrolysis finds itself at different stages of technological readiness.

For the production of multi-carbon products, ongoing efforts are being made to design a stable catalyst, with high selectivity for one product.[21,23,39] Most studies are therefore performed in H-Cells, which are lab-scale reactors with an anode and a cathode compartment that are connected via a circular channel. In these batch reactors, CO_2 gas is continuously fed to the cathode compartment.[40] Processes in flow-cells entailing continuously circulating electrolytes are rarely reported.[41,42]

The production of formic acid via the CO_2 electrolysis is closer to commercialization. While many studies report the production of formate salt, which needs to be converted to formic acid in a downstream process, flow-cell designs enabling direct formic acid production have been introduced.[43,44]

The CO_2-to-CO electrolysis is the most advanced in terms of commercialization. The progress made in this process is mostly based on Ag as a highly selective and stable catalyst for the CO_2-to-CO reduction reaction.[45] Stable performances with run-times over 3800 h at 200 mA/cm² and FE(CO)$\geq$ 90% have been demonstrated. The outstanding stability of the process has been demonstrated in on-off operation and at current densities $\geq$ 500 mA/cm².[9,46] Thus, the research focus is shifting from the reduction of cell voltage and CO_2 consumption toward the scaling of the process.[9,47] A prominent case in terms of scaling is a CO_2-to-CO electrolyzer in pilot scale (300 cm²) operating at 300 mA/cm² with an FE(CO) $\geq$ 90 % for more than 1000 h.[10,48]

2.4 CO_2 -to-CO Electrolysis

2.4.1 Application of CO_2 -to-CO Electrolysis

The main product in the CO_2-to-CO electrolysis is CO, which serves as a valuable resource for various industries. For instance, up to one million tons of pure CO per year are consumed to produce acetic acid (CH_3COOH) and formic acid via methyl formate ($C_2H_4O_2$).[49–51] In a reaction of CO with chlorine (Cl_2), phosgene ($COCl_2$) can be produced, which is an intermediate for the production of polyurethanes and polycarbonate plastics.[50] In Table 2.1, several products formed with pure CO, the chemical reaction to the desired product, and the industry in which the product is used are listed. It is noteworthy, that CO is also used in metallurgy to reduce oxides to metals and to produce Ni, FE, or Co in high purity. Moreover, as a constituent of syngas (CO +H_2) synthetic fuels can be produced via the Fischer-Tropsch synthesis.[19,29,52,53]

Table 2.1: Products produced with pure CO, the chemical reaction of CO to the desired product, and the industry in which the product is used.

Product	Chemical reaction	Industry
Acetic Acid	$CO + CH_3OH \rightarrow CH_3COOH$	Food, Textile
Phosgene	$CO + Cl_2 \rightarrow COCl_2$	Construction, Automotive
Propionic Acid	$CO + C_2H_4 + H_2O \rightarrow C_3H_6O_2$	Agrochemical, Plastics
Adipic Acid[54]	$2CO + C_4H_6 + 2H_2O \rightarrow HO_2C(CH_2)_4CO_2H$	Textile, Plastics
Methyl formate	$CO + CH_3OH \rightarrow C_2H_4O_2$	Agrochemical, Textile

Various fossil resources are being tapped to meet the demand for CO gas. In centralized large-scale plants up to 50 000 m^3/h of CO can be produced. Most of the traditional processes perform the gasification of coal, the steam reforming of natural gas, or the partial oxidation of hydrocarbons to produce CO.[29,50] The product gas from these processes needs to be purified in downstream processes and is subsequently transported to

the end-user. The transport of CO, which is carried out in pipelines, tube trailers, or gas cylinders, is rather expensive and hazardous due to the toxicity and flammability of CO.[29]

Considering the application and traditional production of CO, the CO_2-to-CO electrolysis offers a sustainable alternative. Fossil resources can be replaced by a process that combines the CO_2 utilization with renewable energy sources. Furthermore, the opportunity arises to decentralize the production of CO to an electrolyzer plant that can operate on-demand and close to the customer site, reducing not only the transporting cost but also improving plant safety, since large-scale tanks for CO gas storage are not required.[29]

2.4.2 Cathodic and Anodic Reactions

In the CO_2-to-CO electrolysis, CO_2 undergoes the electrocatalytic reaction to CO at the catalyst surface of a cathode within an electrochemical cell. CO_2 reacts with H_2O under the participation of electrons to CO and hydroxide ions (OH^-) (Equation 2.10). As a side product, H_2 forms at the cathode originating from the H_2 evolution reaction (HER), which describes the splitting of water under the participation of electrons to H_2 and OH^- (Equation 2.11). These two cathodic reactions compete for the electrons in the cathode, while the HER is thermodynamically favored and suppresses the CO_2 reduction reaction at low pH on all known catalysts.[25,55,56]

$$CO_2 + H_2O + 2e^- \rightleftharpoons CO + 2OH^- \tag{2.10}$$

$$2H_2O + 2e^- \rightleftharpoons H_2 + 2OH^- \tag{2.11}$$

Furthermore the side reactions of CO_2 with OH^- to bicarbonate (HCO_3^-) and carbonate (CO_3^{2-}) reactions appear at the cathode (Equation 2.12, 2.13).

$$CO_2 + OH^- \rightleftharpoons HCO_3^- \tag{2.12}$$

$$HCO_3^- + OH^- \rightleftharpoons CO_3^{2-} + H_2O \tag{2.13}$$

These exergonic side reactions, increase the cell voltage and simultaneously consume valuable educt. Thus, the CO_2-to-CO electrolyzer is forced to be operated with CO_2 in excess to sufficiently suppress the the HER.[30] The loss of CO_2 via the formation of HCO_3^- and CO_3^{2-} can be inhibited by operating in an acidic environment at the cathode. While the formation of HCO_3^- and CO_3^{2-} still appears in low pH regimes, it decomposes immediately back to CO_2 and is therefor not lost to the electrolyte.[57] The underlying issue with this approach is the aforementioned domination of the HER that suppresses the CO_2 reduction reaction at low pH values.[56] It is noteworthy, that researchers presented a CO_2 electrolyzer producing multi-carbon products in a flow-cell operating with an acidic catholyte. It was shown, that high potassium concentrations accelerate the CO_2 reduction reaction in an acidic environment and enhance the selectivity of the CO_2 electrolyzer by forming a local alkaline environment, and hence suppressing the HER.[57]

Regarding the anode of the CO_2-to-CO electrolyzer, the CO_2 reduction reaction is most frequently paired with the oxygen evolution reaction (OER) at the anode.[58] The OER describes the oxidation of H_2O to O_2 and H^+ (Equation 2.14).

$$H_2O \rightleftharpoons \frac{1}{2}O_2 + 2H^+ + 2e^- \tag{2.14}$$

Employing the OER as the anode reaction facilitates the designing of the CO_2-to-CO electrolyzer, as the anode can be adapted from the more mature PEM water electrolysis.[25] However, O_2 is a product with a negligible economic value and the OER contributes to a majority of the energy demand of the CO_2 electrolyzer. Efforts are being made to replace the OER and couple the CO_2 reduction reaction with a more favorable anodic reaction. A highly discussed approach is to couple the CO_2 reduction reaction with the chlorine evolution reaction at the anode (Equation 2.15), leading to the production of valuable products at both electrodes.

$$2Cl^- \rightleftharpoons Cl_2 + 2e^- \tag{2.15}$$

Nonetheless, the chlorine evolution reaction requires a higher energy input (1.36 V vs. RHE) in comparison to the OER (1.23 V vs. RHE).[59] Oxidation reactions of aldehyde, ethanol, methanol or other organic compounds, in contrast, lower the energy input and overpotential loss while simultaneously producing value-added products.[58,60,61] However, this approach is limited by the complexity of downstream processes for product purification and by the market mismatch of anodic and cathodic products.[61] When pairing the CO_2 reduction reaction with the hydrogen oxidation reaction (Equation 2.16) the aforementioned challenges can be circumvented. Here, the energy input is reduced but the product of the cathodic reaction is the single valuable product of the process. Regarding the economic value of this process, the input of energy in the production of the sacrificed H_2 needs to be considered.[61]

$$H_2 \rightleftharpoons 2H^+ + 2e^- \tag{2.16}$$

2.5 Flow-Cells for CO_2 -to-CO Electrolysis

To realize an economically viable CO_2-to-CO electrolysis process, the CO_2 reduction reaction needs to be performed continuously. Reactants need to be fed to the reaction sites continuously, and simultaneously the products need to be removed. For this continuous process, flow-cells are designed, through which the liquid media is circulated continuously. In comparison to their batch counterparts, the flow-cells benefit from enhanced mass- and heat transfer as well as better control over the resident time of reactants in the cell.[25]

For the CO_2-to-CO electrolysis, various flow-cell concepts have been demonstrated, while most promising performances have been shown with flow-cells operating with gas diffusion electrodes (GDEs) as cathodes.[24]

2.5.1 Gas-Diffusion-Electrode

In terms of the media flow supply and removal, a challenge associated with the CO_2 electrolysis is the supply of reactants in different physical states. Following the equation 2.10 and 2.14, H_2O is a necessary educt for the CO_2-to-CO electrolyzer. While the delivery of H_2O to the anode via an aqueous electrolyte is straightforward, the cathode requires the delivery of two reactants, one gaseous (CO_2) and one liquid (H_2O) at ambient conditions. It is possible to combine the two reactants in one media flow, by solving the gaseous CO_2 in an aqueous catholyte. However, this option is limited in terms of the selectivity at high current density due to the relatively slow diffusion and low solubility (34 mM) of CO_2 in water.[7,62] A prominent solution that circumvents the low solubility is the GDE. These electrodes have widely replaced solid electrodes in the field of the CO_2 electrolysis. In terms of the structure of the GDE, a porous catalyst layer is deployed along with a diffusion media.[62–64] This structure enables the GDE to separate a liquid media flow from the vapor CO_2 feed gas flow, which is commonly fed from the rear side of the electrode.[65]

2.5.2 Flow-Cell Architectures

Among various cell designs for the CO_2-to-CO electrolysis, the GDE-flow-cell and flow-cells with membrane electrode assemblies (MEAs) are the most prominent concepts.[38,66] These flow-cells are illustrated in Figure 2.2, depicting the flow of the electrolytes and the CO_2 feed gas, as well as the placement of the membranes, the anode, and the GDE.

In the GDE-flow-cell a GDE is applied as a cathode, separating the gas compartment from the catholyte compartment. The catholyte is, similar to the anolyte, in most demonstrated cases an aqueous electrolyte that is circulated through the flow-cell. A polymer electrolyte membrane is implemented to separate the catholyte from the anolyte. In terms of the media flows, the CO_2 feed gas is fed from the top to the bottom of the cell, while the electrolytes are fed from the bottom to the top of the cell.[67,68]

In flow-cells with MEAs, a polymer electrolyte membrane is sandwiched between a cathode and an anode, while in most cases both electrodes possess the structure of a GDE. An aqueous anolyte is circulated through the flow-cell. Similar to the GDE-flow-cell, the electrolyte is fed from the bottom to the top and the CO_2 feed gas is fed from top to bottom.[38]

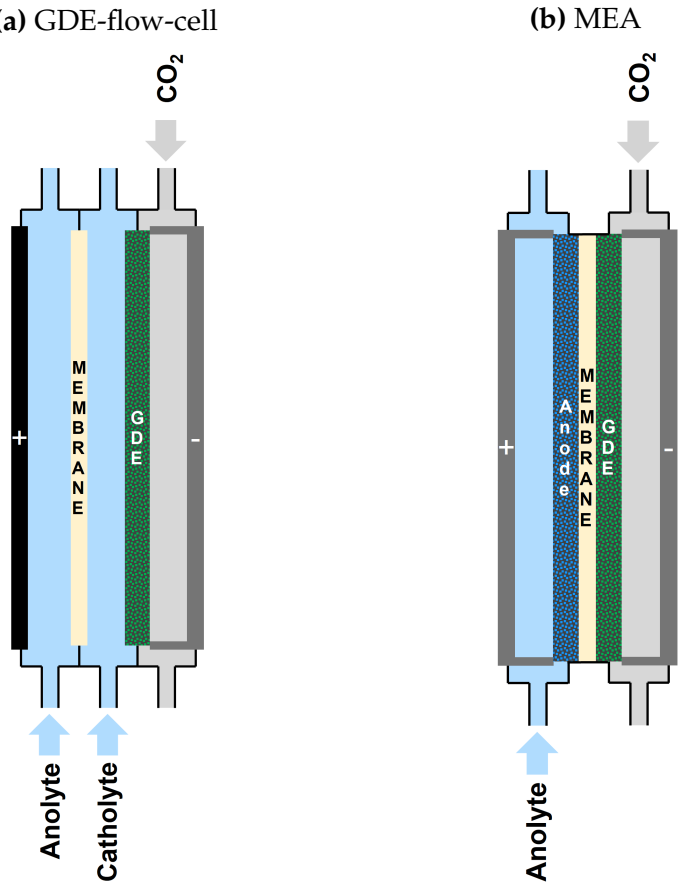

Figure 2.2: Illustrations of architecture, component position and media flow management in (a) GDE-flow-cell and (b) flow-cell with MEA.

In terms of the complexity of the flow-cell designs, the flow-cell with the MEA is beneficial, since the management of the catholyte is omitted. However, one naturally sacrifices flexibility since liquid byproducts can no longer be transported without the catholyte.[7] Without consider-

ing the type of membrane that is implemented into the different flow-cell architecture, one can already estimate the ratios of energy efficiency between the two flow-cells given an equal selectivity of the process. The energy efficiency of the process is dependent on the cell voltage at an applied current density (Equation 2.8). While for the GDE-flow-cell the distance of the electrodes is defined by the thickness of the electrolyte chambers and the thickness of the membrane, the distance of the electrodes in the flow-cell with the MEA is minimized to the thickness of the membrane. Hence, ohmic losses occurring in the electrolyte chambers in the GDE-flow-cell are avoided in the flow-cell design with the MEA. As these ohmic losses increase the cell voltage, higher energy efficiencies can be expected when operating with an MEA.[69]

This hypothesis is only valid when achieving similar selectivity for both flow-cell designs, which is highly dependent on the type of membrane that is used.[38] For the CO_2-to-CO electrolysis, ion exchange membranes have become predominant, widely replacing other membranes.[40,53,69]

2.5.3 Ion Exchange Membranes in Flow-Cells

Ion exchange membranes are polymeric membranes with charged functional groups in the polymer matrix. These membranes selectively support the transport of ions with the opposite charge of the functional group (counter-ions), while at the same time blocking the transport of ions with a similar charge to the functional group (co-ions).[70,71] The permselectivity for counter-ions of ion exchange membranes, also known as the Donnan effect, is the distinctive attribute of the ion exchange membranes, that has led to the implementation of these membranes in various industrial processes including electro dialysis, diffusion dialysis, and electrolysis.[70,71] Regarding the CO_2-to-CO electrolysis, the type of ion exchange membrane determines the architecture of the flow cells.[38] Proton exchange membranes (PEMs), Bipolar membranes (BPMs) as well as anion exchange membranes (AEMs) have been utilized in GDE-flow-cells

and have demonstrated high selectivity for the CO_2-to-CO electrolysis. In flow-cells with MEA, AEMs have shown high selectivity, while MEAs with implemented PEMs or BPMs suffer mainly from insufficient suppression of the HER.[40,53,69]

Proton Exchange Membrane

PEMs utilized in the CO_2-to-CO electrolysis are classified as strong acid membranes that contain sulfonic acid as charged groups. Most common example is the Nafion membrane.[71,72] Via the PEM, protons are transported from the anodic to the cathodic side of the CO_2-to-CO electrolyzer. The transport of protons to the cathode is in terms of the CO_2 reduction reaction problematic since an acidic environment at the cathode favors the HER. Hence, a buffer layer with an alkaline to neutral pH is required between the membrane and the cathode to enable a selective process for CO formation.[38,48,73]

Considering the presented flow-cell designs (Figure 2.2), the GDE-flow-cell provides such a buffer layer in the form of the catholyte chamber. In many cases, the catholyte is a $KHCO_3$ solution, which enables a process in a steady state at the cathode side, when paired with an acid as anolyte.[74] The HCO_3^- and CO_3^{2-} ions are consumed in the reaction with H^+ to CO_2 and H_2O at the interface of the catholyte and the membrane (Equations 2.17 and 2.18). Simultaneously, the HCO_3^- and CO_3^{2-} ions are reproduced by the reaction of CO_2 with OH- at the cathode surface (Equations 2.12 and 2.13). An equilibrium can be reached leading to a stable alkaline to neutral pH value in the catholyte chamber.

$$HCO_3^- + H^+ \rightleftharpoons CO_2 + H_2O \tag{2.17}$$

$$CO_3^{2-} + 2H^+ \rightleftharpoons CO_2 + 2H_2O \tag{2.18}$$

In Figure 2.3 the chemical reactions in a GDE-flow-cell for the CO_2-to-CO electrolysis containing a PEM and operating with the OER at the anode are illustrated.

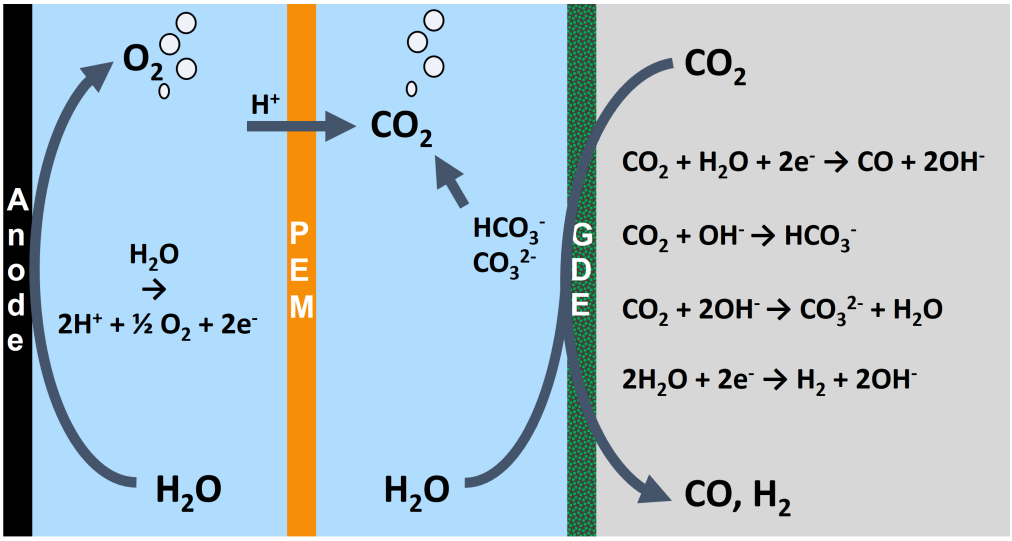

Figure 2.3: Illustration of ion transport through PEM in GDE-flow-cell and reactions at membrane, anode, and cathode.

Regarding the anode side of the presented flow-cell, the choice of electrolytes is limited regarding a process in a steady state. When operating the flow-cell with the OER at the anode and the PEM, protons are produced at the anode and transported to the cathode side. Hence to maintain a stable pH value an acid needs to be used as the anolyte.[28] A drawback accompanying the operation of the OER in an acidic environment is the limitation to noble and therefore expensive metals acting as catalysts for the OER.[53] Ir for instance serves as a stable and selective catalyst for the OER in an acidic environment. However, with annual mining of four tons per year and its application in various electro-catalytic processes, the availability of this catalyst is limited.[28] Alkaline anolytes enable the use of earth-abundant catalysts. In theory, alkaline pH values are even beneficial for the process, since the electrode potential at the anode shifts toward the cathodic electrode potential (Equation 2.4). However, alkaline anolytes are consumed by the produced protons, preventing a process in

a steady state.[28]

In the proposed cell configuration gas bubbles form in the electrolytes acting as non-conductive areas, and are reported to create voltage instabilities.[75] At the anode a counteracting measure can be the implementation of a zero gap anode, describing the placement of a porous anode structure directly on the PEM. The gas bubbles in the anolyte, that are created by the OER, are accordingly no longer in the current path. A further benefit of the zero gap anode is the closing of the anolyte gap, which reduces the distance between the electrode, thereby increasing the energy efficiency.[75] The zero gap anode even allows the usage of low-concentrated anolytes, however, the concentrations of the anolyte and catholyte are interdependent since osmotic pressure between the electrolyte chambers needs to be avoided.[73]

In the catholyte, the gas bubbles originate from the CO_2 formation at the membrane surface. Closing the catholyte gap is not possible without removing the buffer layer. The CO_2 formation in the catholyte can be advantageous for the process, since it is feasible to recover the CO_2 from the catholyte reducing the total educt consumption of the process.[10,48,55]

With the GDE-flow-cell containing the PEM, highly selective processes with FE(CO) between 97-80 % at current densities of 100-500 mA/cm² have been demonstrated. In terms of energy efficiency, flow-cells with the PEM are limited by the buffer layer. A workaround by implementing the PEM in an MEA has been demonstrated, however, the process suffered from poor selectivity compared to the GDE-flow-cell.[38,56]

Anion Exchange Membrane

In comparison to the PEM, the AEM does not create an acidic environment on the cathode-facing surface. A buffer layer between the cathode and the membrane is therefore not necessary to suppress the HER. While the application of the AEM is possible in a GDE-flow-cell, researchers focus on the development of MEAs with AEMs, based on possible higher

energy efficiencies.[32,69,76–81] The ion transport and the respective reactions for the CO_2-to-CO electrolysis in a MEA with an AEM are illustrated in Figure 2.4.

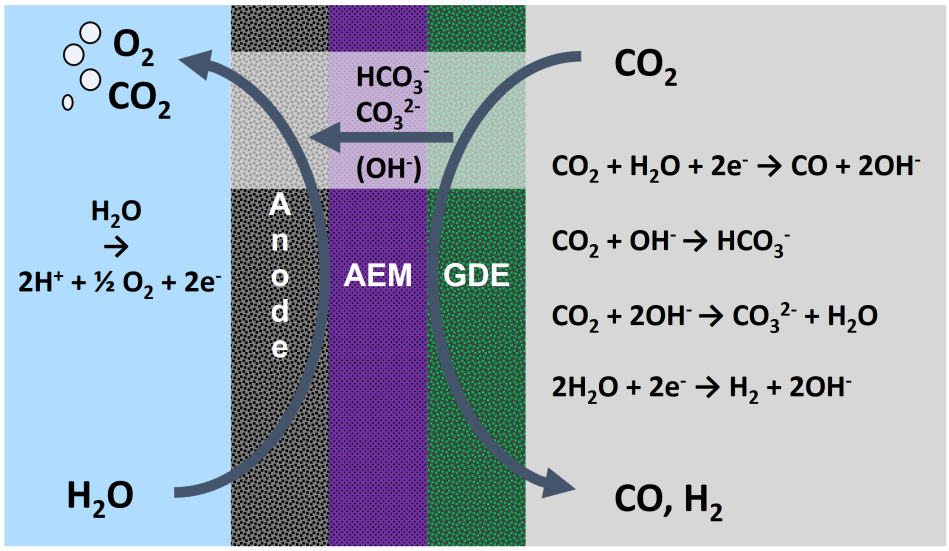

Figure 2.4: Illustration of ion transport through AEM in flow-cell with MEA and reactions anode and cathode.

With AEMs, anions are transported from the cathode to the anode side of the CO_2-to-CO electrolyzer. The ion transport is dominated by $HCO3^-$ and CO_3^{2-} ions that originate from the side reaction of CO_2 with OH^- (Equation 2.12, 2.13). The shuttling of the $HCO3^-$ and CO_3^{2-} ions leads to the formation of CO_2 at the anode, and consequently, a CO_2/O_2 mixture occurs at the anode when applying the OER.[32,80,82–85]

Despite the expectation that AEMs prevent the transport of cations, a transport of cations (e.g. K^+) from the anode to the cathode side is observed in MEAs. The cation transport contributes to salt precipitation (e.g. K_2CO_3) at the cathode GDE, which blocks the catalyst sites as well as the gas flowfield and destroys the hydrophobic characteristic of the GDE with the consequence of flooding.[86] The salt precipitation can be mitigated by flushing the cathode in defined time intervals with H_2O to wash the salt from the GDE.[11] However, this method does not prevent the cation transport via the AEM. A more straightforward solution is to

operate the flow-cell with pure H_2O as anolyte, but this leads to a decrease of selectivity toward CO, indicating that cations are beneficial for the CO_2 reduction at the cathode. The influence of cations on the CO_2 reduction reaction has been the subject of several studies, demonstrating that larger cations, promote the CO_2-to-CO reduction by local electrostatic effects at the catalyst.[69,87–91]

In the CO_2-to-CO electrolysis, most outstanding performances have been demonstrated with the MEAs containing AEMs.[32] Cell voltages of 3 V at 200 mA/cm² and FE(CO) $\geq$ 90 % have been demonstrated.[73] However, the MEAs with AEMs suffer from low CO_2 utilization in comparison to the GDE-flow-cells with PEM or BPMs. The CO_2 participating in the formation of $HCO3^-$ and CO_3^{2-} can not be recovered without an elaborate downstream process, which performs the separation of the CO_2/O_2 mixture. Considering this aspect increasing investment and operating costs must be anticipated when designing a process around the MEA flow-cell.[85,92]

Bipolar Membrane

The BPM is a two-layered membrane combining an AEM and a PEM, which has been utilized in the CO_2 electrolysis in two different orientations[93,94]:

- Forward bias: The PEM side of the membrane faces the anode
- Reverse bias: The PEM side of the membrane faces the cathode

When the forward bias mode is applied, protons from the anode side and bicarbonate from the cathode side react to CO_2 at the bipolar junction. In the forward bias operation, the BPM can be implemented in an MEA, however, commercially available BPMs are here limited by salt precipitation at the cathode and delimitation of the membranes.[93,94] When operating a CO_2-to-CO electrolyzer in reverse bias, H_2O is split to H^+ and OH^- an the internal interface (Equation 2.19).[93,95]

$$H_2O \rightleftharpoons H^+ + OH^- \tag{2.19}$$

The positively charged ions are transported toward the cathode, and the negatively charged ions are transported toward the anode. Similar to the flow-cells with PEMs, flow-cells with BPMs in reverse bias require a buffer layer between the membrane and the cathode to suppress the HER sufficiently.[69,80,96,97] In terms of the OH^- transport to the anode, the BPM offers the unique opportunity to operate a CO_2-to-CO electrolyzer in a steady state with an alkaline or neutral anolyte. The OER can therefore be performed with an earth-abundant metal catalyst which is beneficial in terms of investment cost and sustainability of the process.[83,96–98] Furthermore, higher pH values at the anode benefit the energy efficiency by reducing the equilibrium electrode potential (Equation 2.4).

In Figure 2.5 the reactions appearing in a GDE-flow-cell operating with a BPM in reverse bias are illustrated, including the reactions occurring at the electrodes and in the electrolytes.

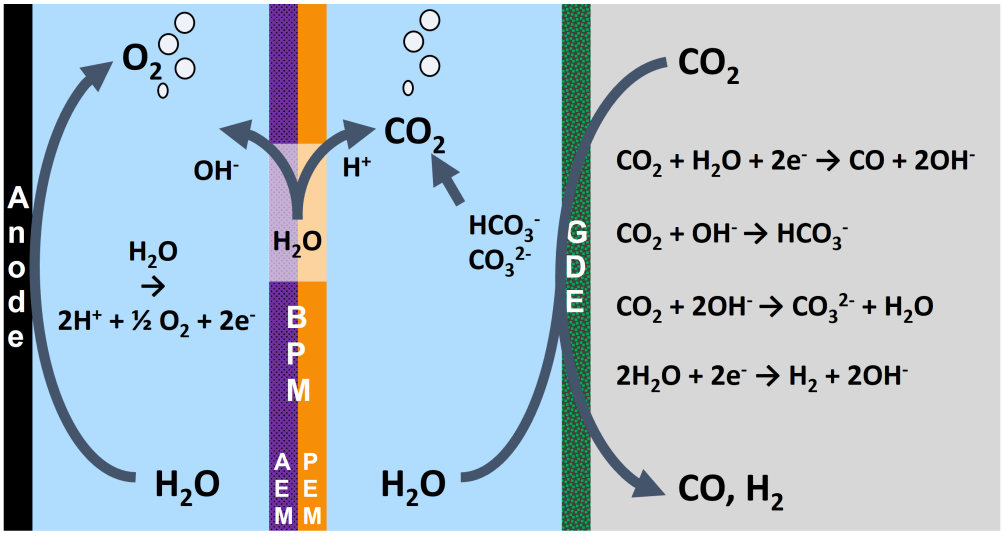

Figure 2.5: Illustration of ion transport through a BPM in GDE-flow-cell and reactions at membrane, anode, and cathode.

Addressing the process performance of flow-cells operating with the BPM, stable processes have been demonstrated with GDE-flow-cells for

24 h. Extended operations have been demonstrated to be challenging, as the BPM is still in an early stage of development.[69,82] FE(CO) $\geq$ 90 % have been achieved at 100-200 mA/cm² for a GDE-flow-cell design operating with a BPM membrane. However, high cell voltages were determined with the BPM originating from the large potential ($\approx$ 820 mV/mol_{H_2O}) that is required to split H_2O within the BPM.[69] It is noteworthy, that the BPM has been implemented in an MEA cell design, producing CO directly from a carbonate solution at the cathode. Lower cell voltages were obtained in this cell design, however, a FE(CO) of only 35 % has been achieved.[99,100]

2.6 Scaling in CO_2 -to-CO Electrolysis

The majority of publications around the CO_2-to-CO electrolysis concern the performance and design of single-flow-cells in lab-scale size, however, the scaling of the process attracts increasing attention. The scaling procedure is derived from more mature electrolysis processes. In general, the active cell area needs to be increased to increase the product volume flow of the electrolysis process. The most straightforward method is to increase the size of the cells by increasing the size of electrodes, membranes, and other components. Increasing the size of a CO_2-to-CO electrolyzer has been demonstrated in several publications. Most prominent is the aforementioned design of a CO_2-to-CO GDE flow-cell in pilot scale (300 cm²).[10] Another possibility is to increase the number of cells. As it is not practical to operate multiple single-cells in parallel with individual peripheries, it is common practice to assemble multiple cells into stacks. The stacking of the electrolyzer, however, has received little attention despite being a key enabling step toward the industrial application of the process. To scale electrolysis processes, the increase in cell size and the stacking are applied simultaneously.[10,25,101–103]

2.6.1 Increasing Size of Single-Cells

Increasing the size of an electrolyzer is the most straightforward way to scale the electrolysis process. In an optimized system, the current increases with increasing cell size, while the cell voltage remains constant. Higher currents and larger areas imply, that media flow management needs to be adjusted toward supplying a larger area with an increased amount of reactants. Therefore, studies concerning flow-fields that enable homogeneous reactant distributions over large cell areas need to be emphasized.

Flow-Fields

In recent studies, it has been demonstrated, that the feed gas delivery on the GDEs surface influences the performance of the CO_2-to-CO electrolyzer. When introducing the feed gas via a meandering channel (Figure 2.6), CO_2 is consumed along the media flow channel, and the products are concentrated. Hence a concentration gradient for CO_2 forms along the gas channel. This gradient can lead to an insufficient feed gas supply toward the lower part of the GDE, which favors the HER. The catalyst surface area is therefore only partially exploited for the CO_2 reduction reaction. Counteracting by increasing the feed gas supply is a possible solution, but is disadvantageous in terms of the increased educt consumption and the dilution of the product gas.[104]

In more mature electrolysis processes, such as the PEM water electrolysis, the issue of concentration gradients is well documented. Supported by models and experimental data, flowfield designs with different lengths, channel numbers, channel thicknesses, and various patterns have been investigated to optimize the media flows toward a more homogeneous distribution.[105]

Among other flow-field designs, the Meander flow-field and the interdigitated flow-field (Figure 2.6) are objects of the investigations in PEM water electrolysis. The Meander flow-field has demonstrated an effective coverage of entire active cell areas when applied in small active area

applications. When increasing the active area, multiple parallel meander channels need to be implemented to ensure complete coverage.[105,106] Similar to the investigation in the CO_2-to-CO electrolyzer, the Meander generates concentration gradients leading to an uneven reactant distribution. Furthermore, a high-pressure drop and water buildup in the bends are disadvantages.[104,105] The interdigitated flow-field provides several interlocking branches which are not connected. These dead ends force the gas through the electrode to pass from the inlet to the outlet channel. In PEM water electrolyzers, these flow-fields demonstrate enhanced mass transport, and a homogeneous reactant distribution and prevent flooding of the electrode at higher current densities. However, the interdigitated flow-field has not been extensively used, as long-term damage to the electrodes is anticipated and a high-pressure drop is generated.[105]

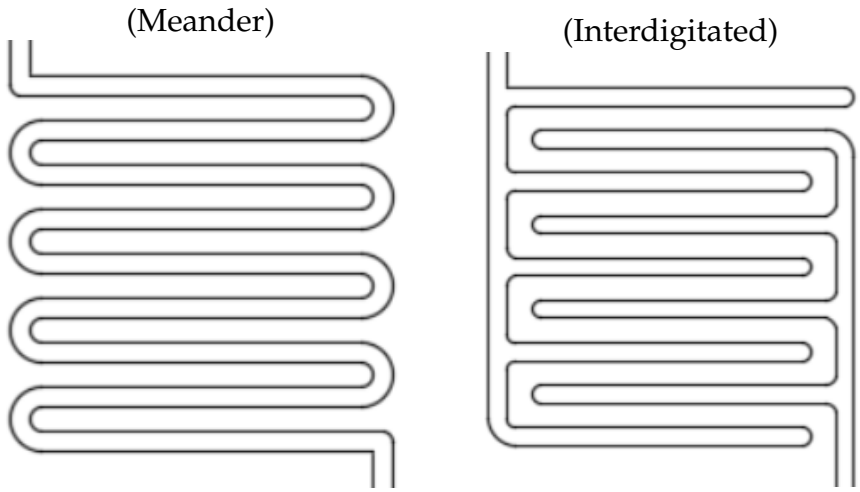

Figure 2.6: Illustration of Meander and Interdigitated flow-field.

Since the CO_2 electrolysis is a rather young technology, the gained understanding of media flow management has been barely transferred to the CO_2 electrolysis. However in terms of the pending and in parts already ongoing scaling of the process, specifically regarding the CO_2-to-CO electrolysis, an advanced media flow management is required.[25]

Management of Electrolyte Flow

A challenge associated with the increase in cell size is the increase in hydrostatic pressure in the media flow chambers. At the bottom of the media flow chamber, higher pressure occurs, than at the top of the chamber. While there has not been a demonstration of adverse impacts on flow-cells with MEAs, since the membrane blocks water permeation through the GDE, the scaling of the GDE-flow-cell is limited. Here, the differential pressure in the media flow chambers causes flooding at the bottom of the GDE. It is possible to mitigate the flooding by applying pressure in the gas chamber, however, the pressure in the gas compartment can only be applied uniformly. Meaning, that at the bottom of the cell, flooding might be prevented by pressurizing the gas chamber, however at the top of the cell gas permeates through the GDE to enter the catholyte. In both cases, the performance of the GDE-flow-cell is diminished.[68]

A possible workaround is to manage the electrolyte flow by feeding the cell from top to bottom. Reactors operating with these electrolyte flows are referred to as Falling-Film-Reactors. The Falling-Film-Reactor is designed similarly to the GDE-flow-cell, however instead of entering the catholyte chamber from the bottom of the cell, the catholyte is introduced from the top of the cell. While this process mode eliminates the hydrostatic pressure in the catholyte chamber, a structure needs to be implemented to ensure a homogeneous catholyte distribution.[68] The application of the falling film reactor is only possible in special cases. As described in chapter 2.5.3 GDE-flow-cells operating with BPMs or PEMS induce gas bubble formation in the catholyte chamber. When introducing the catholyte from the top in these cells, two opposing media flows are present, with the gas bubbles flowing upwards and the catholyte flowing downwards. To oppose this effect, the environment at the anode needs to be changed. For instance, an anolyte that consumes the protons produced at the anode (1M $KHCO_3$) can be used, however, the steady state of the process is diminished.[28,68] Pairing the cathode reaction with another anode reaction than the OER or implementing an AEM into the

GDE-flow-cell are other possible solutions.[58,107]

2.6.2 Stacking of Flow-Cells

Assembling multiple cells into an electrolyzer stack is a common practice to scale electrochemical processes. In an electrolyzer stack, multiple cells are connected in series via bipolar plates. At the End-Plates, which serve as current collectors for the terminal cells in the stack (the terminal anode provides the global anode and the terminal cathode provides the global cathode), a voltage is applied.[25,108] In contrast to the scaling by size increase, the voltage that needs to be applied to a stack to maintain a constant current density increases proportionally to the number of cells, when operating in an optimized system, leading to lower ohmic losses in the periphery.[108]

The stacking of flow-cells is associated with several challenges, such as the design of end-plates and bipolar-plates. These plates serve as supporting structures to membranes and electrodes and act as current collectors to the electrodes.[25,108] Furthermore, the plates provide flow-fields and therefore manage the media flow distribution over the electrodes.[105]

A special challenge is the design of the bipolar-plates which serve a cathode and an anode simultaneously. Regarding the material of bipolar-plates and end-plates, main properties such as corrosion resistance, high thermal conductivity, and low resistivity need to be fulfilled. Titanium (Ti) meets the aforementioned requirements, however, the use of Ti flow-fields and bipolar-plates can be limited. In PEM water electrolysis, for instance, the materials are confronted with anode or cathode-specific challenges. While these challenges have not been investigated in CO_2 electrolysis yet, it is reported, that the cathode, where hydrogen is produced in PEM water electrolysis, Ti components suffer from the hydrogen embrittlement. The thereby destroyed mechanical properties of Ti in long-term operation leads to performance loss. At the anode, the OER takes place, forming passive oxide layers at the Ti surface, which increases the inter-facial conductive resistance and diminishes the cells' performance.

By applying a coating, for instance, Ir, on the Ti components, these effects can be suppressed.[73,105,109]

Aside from the components materials, media flow management, and manifolding need to be taken into account when stacking flow-cells. Active or passive cooling of the stack via the electrolyte is crucial since an accelerated heat development can be anticipated in stacks.[9,105,110] In terms of the manifold, shunt current formation is an issue in stacks. These parasitic currents form in electrolytes, that are flowing parallel to the current path in the stack. Thus, part of the applied current flows through the electrolyte from the positive to the negative side of the stack, resulting in accelerated degradation and corrosion processes as well as in diminished cell performances.[108,111]

Regarding the stacking in CO_2-to-CO electrolysis, a multi-layer short-stack has been presented in the literature. The short-stack operated successfully with three MEA cells at elevated temperatures (50 °C) under different pressures in the feed gas compartment.[11]

Chapter 3

Materials and Methods

The materials used in the experiments of the presented work as well as generally applied methods valid for all experiments are presented in the following. A description of specific materials and methods and the individual test benches designed for individual experiments can be found in this chapter.

3.1 Cell Components and Electrolytes

In the presented study, PEM, AEM, and BPM were used in different experiments. A Nafion® 212 membrane (Sigma-Aldrich®) was used as a PEM, the Sustainion® purchased from Dioxide Materials™ was employed as an AEM and the fumasep® FBM was used as the BPM in the experiments.

In all experiments the GDE with an Ag catalyst layer from Dioxide Materials™ for carbon dioxide electrolyzer[112] was used as the cathode. Three different anodes were used throughout the study, (a) a Ti-plate coated with Ir-MMO purchased from ElectroCell® (Europe, Denmark) and used as a planar anode, (b) a titanium mesh with an Ir-MMO coating and a mesh width of 4x2 mm was purchased from ©Metakem and used as a zero-gap anode, (c) a GDE type electrode with an Ir-MMO catalyst layer was purchased from Dioxide Materials™[112] and was used as the

anode in experiments with MEAs. In all experiments, the active cell area was 10 cm^2.

Electrolytes were prepared with ultrapure water (PURELAB® flex). H_2SO_4 or $KHCO_3$, both from Honeywell Fluka™ in the purity of 97 % were used as well as KOH from ©Merck.

3.2 Materials for Test Benches

The different test benches in this study were assembled with FEP pipes with an inner diameter of 4 mm for the electrolytes and an inner diameter of 1/8 inch for the feed gas. Peristaltic pumps and piston pumps from Ismatec were used to pump the electrolytes through the cells. MFCs were used to control the feed gas and the sweep gas volume flows. For pressure control in the feed gas pipes a back pressure regulator. In all experiments, the CO_2 feed gas was fed through a membrane humidifier before entering the gas chamber in the cells.

In all electrochemical experiments, the potentiostat PGSTAT302N with PX1000s modules was used. In individual experiments, the potentiostat was combined with a 20 A booster.

In Table 3.1 the manufacturer as well as the specifications of the instruments are listed.

Table 3.1: Instruments

Instrument	Manufacturer	Specification
Peristaltic pump	Ismatec	Masterflex Reglo Miniflex Digital Pump
Piston Pump	Ismatec	Masterflex Reglo Digital Piston Pump
MFC	Bronkhorst	
Vacuum Pump	KNF	LABOPORT N 86 KT.18
Membrane contactor	3M™	3M™ Liqui-Cel
Humidifier	Permapure	Model PPMH-110-12P
Potentiostat	Metrohm	PGSTAT302N
20 A Booster	Metrohm	

3.3 Analytical Materials and Methods

The product gas from the cathode, the separated gas from the catholyte, and the gas produced at the anode side were analyzed separately via a Trace 1310 Thermo Scientific gas chromatograph (Thermo Fischer) with 3 parallel gas analyzer channels. Atmospheric gases and CO were separated on a 3m x 1mm ShinCarbon ST packed column with He carrier gas coupled to a thermal conductivity detector (TCD). H_2 was separated on a 2 m x 1 mm 5Å molecular sieves packed column with Ar carrier gas coupled to a TCD. Hydrocarbon products were separated on a 30m x 0.32 mm RG-bond Alumina (KCl) capillary column with He carrier gas coupled to a flame ionization detector (FID). Samples were injected from sample loops coupled directly to the experiment via a heated transfer line.

The gases were quantified via a drum-style gas counter or a MilliGas counter (for gas flows below 20 ml/min). For the gas in the anolyte and the gas from the catholyte, Ar was applied as a sweep gas. pH values and temperatures were measured in the electrolytes with the Unitrode from Metrohm, which could either be used with the PX1000s modules on the potentiostat or with the Almemo 710 datalogger from Ahlborn. Other analytical devices such as temperature probes (NiCr) from Ahlborn as well as differential pressure transmitters from Ahlborn to determine differential pressures in electrolytes were used with the Almemo datalogger. The conductivity of the electrolytes was determined with a conductivity meter from Mettler Toledo. In Table 3.2 the manufacturer as well as the specifications of the instruments are listed.

Table 3.2: Analytical materials

Instrument	Manufacturer	Specification
Datalogger	Ahlborn	Almemo
pH and temperature probe	Metrohm	Unitrode with pt1000
Differential pressure transmitter	Ahlborn	FDA 602 D
Pressure sensor	Ahlborn	FDAD33/35M
Gas counter	Ritter	TG0.5-PP-PP
Small Gas counter	Ritter	MilliGascounter MGC-1 V3.4 PMMA
Conductivity meter	Mettler Toledo	SevenCompact Cond meter

3.4 Feed Gas Parameter

In all experiments, the CO_2 feed gas supply was connected to the experimental parameter λ, which has been introduced in the literature to describe the CO_2 excess in experiments[48]. The definition of λ is the ratio of the volumetric amount of CO_2 ($\dot{V}_{CO_2}$) supplied to the cell, to the theoretical maximal producible volumetric amount of CO ($\dot{V}_{COmax}$) (Eq.:3.1). The maximum volumetric formation rate of CO is thereby calculated with the Faraday constant, the number of transferred electrons, the molar volume of CO ($V_{CO_{mol}}$ = 24.41/mol), and the total cell current I (Eq.:3.2). According to the literature, an electrolyzer operating with neutral to alkaline catholyte buffers requires a $\lambda \geq 3$ to sufficiently suppress the HER in CO_2.[48]

$$\lambda = \frac{\dot{V}_{CO_2}}{\dot{V}_{CO_{max}}} \tag{3.1}$$

$$\dot{V}_{CO_{max}} = \frac{V_{CO_{mol}}}{z \cdot F} \cdot I \tag{3.2}$$

3.5 Experimental Protocols

In this section, specific materials, methods, and individual test benches designed for the experiments are described.

Various Flow-Cell Concepts

In this section, the experimental protocol is described for the experiments with various flow-cell concepts presented and discussed in Chapter 4.1.

A GDE-flow-cell and a flow-cell with an MEA were both assembled with the Micro Flow Cell from ElectroCell® (Europe, Denmark). In Figure 3.1, a flowsheet of the test bench used for the experiments is illustrated with an exemplary illustration of an implemented GDE-flow-cell.

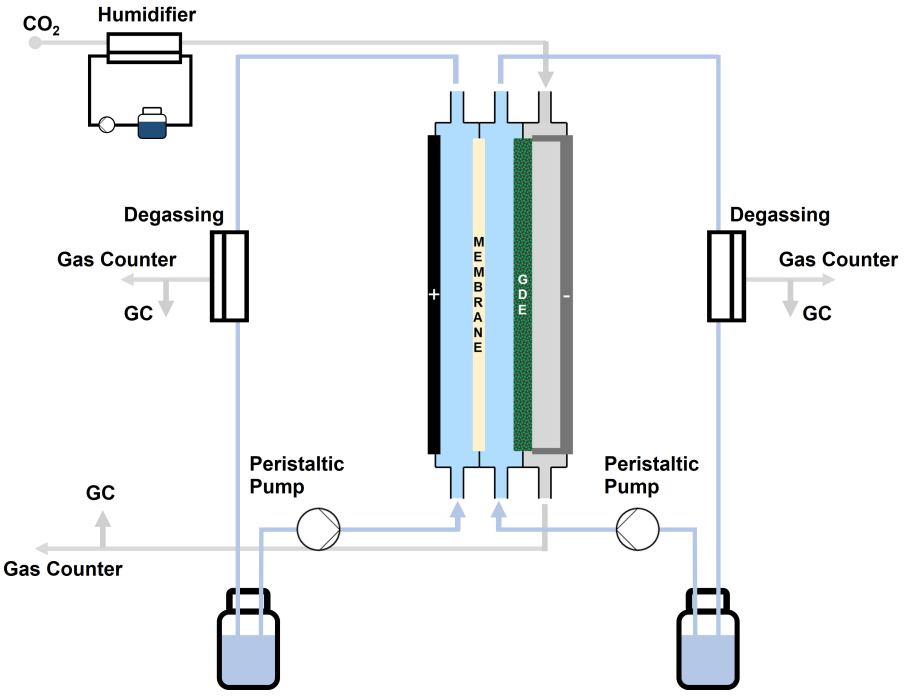

Figure 3.1: Flowsheet of test bench for testing cell configurations with an exemplary illustration of an implemented GDE-flow-cell.

The GDE-flow-cell contained an anolyte and a catholyte chamber, sep-

arated by a membrane. The electrolyte chambers had a depth of 2 mm each. The planar anode, that was used in these experiments was 6 mm apart from the cathode. 1M $KHCO_3$ solution was used as catholyte and was circulated through the cell with a volume flow of 50 ml/min from reservoirs containing 250 ml of the electrolytes. Similar volume flow and reservoir were used for the anolyte, while in different experiments either 1M H_2SO_4 or 1M KOH was used as anolyte.

For the experiments with the MEA, the Dioxide materials anode (3) and the cathode GDE were mated on the Sustainion AEM. Meander flow-fields made from titanium (Grade 1) and purchased from ElectroCell® (Europe, Denmark) were implemented to press the components on each other. A 10 mM $KHCO_3$ solution was used as an anolyte in experiments with the MEA. Similar to experiments with the GDE-flow-cell, the gas appearing in the anolyte was separated from the liquid via a membrane contactor in combination with a vacuum pump.

The product gases from the anolyte, the cathode, and the catholyte were analyzed via the gas chromatograph and the gas counters described in Chapter 3. The gases present in the electrolytes were separated from the liquid via membrane contactors in combination with vacuum pumps. The data presented are average values of three individual measurements in the same experiments. One of these measurements consisted of one GC Analysis of each of the three gas streams from the cell, which were measured consecutively via a switching valve. Each GC analysis took 12 min resulting in a measurement time of 36 min for the cell and 108 min for a statistically supported data point.

The BPM, the Fumatech AEM, and the PEM described in Chapter 3 were implemented in individual experiments into the GDE-flow-cell. The Sustainion AEM was not implemented as a separator in a GDE-flow-cell, due to the membrane´s low mechanical stability. For experiments with the MEA, the Sustainion AEM was chosen over the Fumatech AEM, to enable a marriage of the membrane and the Ag-GDE.

With flow-cells in different configurations, experiments were per-

formed at 100 mA/cm^2 (1 A) for 200 min with a constant $\lambda = 4.5$.

The performance of the cells was measured in their selectivity, energy efficiency, CO_2 conversion, and the formation of CO_2 at the anode. The indicators are given by the FE(CO), U_{Cell}, $\epsilon_{(CO)}$, and the ratio of CO_2 to O_2 in the anolyte gas ($\frac{CO_2}{O_2}$). For completeness, the EPC is given for all cells but not discussed since it is inversely proportional to $\epsilon_{(CO)}$.

GDE-Flow-Cell Operating with Different Flow-Fields

In this section, the experimental protocol is described for the experiments with a GDE-flow-cell operating with different flow-fields presented and discussed in Chapter 4.2.

The cell design as well as the electrolyte configuration used in this chapter was similar to the ones used for GDE-flow-cell with the PEM tested in Chapter 4.1. A unique variation was the implementation of the zero gap anode instead of the planar electrode, thus the anode and cathode were 4 mm apart.

The test bench was assembled similarly to the experiments in Chapter 4.1, with the additional implementation of differential pressure sensors between the cell´s entrance and exit of the catholyte chamber.

The product gases from, the cathode and the catholyte were analyzed via the gas chromatograph and the gas counters described in Chapter 3. The gas appearing in the catholyte was separated from the liquid via a membrane contactor in combination with a vacuum pump. A total quantification for one gas stream took 12 minutes, thus generating a full data point for two gas flows took 24 min. Three full data points were averaged into one measurement. The gas appearing in the anolyte was not analyzed since no traces of CO_2 or cathodic products were observed in previous experiments.

All experiments were performed with a PGSTAT302N potentiostat (Metrohm), operating in galvanostatic mode at 1 A (100 mA/cm^2).

Experiments were conducted under different CO_2 supply rates in connection to the experimental parameter λ. λ was varied by two different

methods: 1. varying the partial pressure of CO_2 (p_{CO_2}) in the feed gas by the substitution of Ar, while maintaining a constant feed gas volume flow at 35ml/min, 2. operating with pure CO_2 gas and varying the feed gas volume flow.

For all experiments, one measurement point was generated for the λ-values 4.5, 3, 2, and 1, while $\lambda = 4.5$ was the starting value, and λ was subsequently reduced. In experiments with pure CO_2 supply λ was additionally reduced to 0.5.

The experiments were conducted with cells containing various structures in the gas chamber or flow-fields (titanium grade 1) with different gas path architectures.

The concentrations of CO (φ_{CO}) and CO_2 (φ_{CO_2}) in the product gas of the cathode were used to describe the performance of the cell. φ_{CO} and φ_{CO_2} in the product gas from the cathode were calculated via the volume flow of CO/CO_2 ($\dot{V}_{CO_{out}}$ / $\dot{V}_{CO2_{out}}$) based on the data obtained by the gas chromatograph and the total volume flow of the product gas ($\dot{V}_{tot_{out}}$) determined by the gas counters (Eq.:3.3).

$$\varphi_{CO/CO_2} = \frac{\dot{V}_{CO_{out}/CO_{2out}}}{\dot{V}_{tot_{out}}} \cdot 100\% \tag{3.3}$$

Modular Short-Stack Operating with an MEA

In this section, the experimental protocol is described for the experiments with a modular short-stack operating with an MEA presented and discussed in Chapter 4.3.

The short-stack was assembled with bipolar-plates and end-plates, each providing a meander media flow channel. The single-cells contained two end-plates. The end-plates and bipolar-plates were manufactured from Ti (Grade 1). PTFE sheets with a thickness of 300 µm, and with a rectangular window of 10 cm^2 were integrated to seal the cells around the electrodes and to function as insulators. The MEA was assembled similar to the one described in Chapter 4.1 and a 10mM $KHCO_3$ solution was used as anolyte. The anolyte was circulated via a peristalic

pump with a volume flow of 50 ml/min and 150 ml/min through the single-cell and short-stack from vessels containing 250 ml and 500 ml of the electrolyte, respectively.

The product gas from the cathode and the anode were analyzed via the gas chromatograph and the gas counters described in Chapter 3.

Experiments were conducted in two systems, (1) single-cell and (2) three-cell short-stack. For both systems, experiments were performed at 200 mA/cm^2 for 300 min. Additionally, the current density was stepwise increased from 100 to 200, 300, and 400 mA/cm^2. Each current density was applied for 100 min. For each current density step, a galvanostatic electrochemical impedance spectroscopy (EIS) measurement was performed under load in a frequency range from 40 kHz to 100 mHz and an amplitude of 10 % of the applied current density.

To provide a sufficient CO_2 supply to the cell, $\lambda = 5$ was applied in all experiments.

To characterize the single-cell and the short-stack, the listed performance indicators are utilized:
(1) FE(CO) of the single-cell, (2) FE(CO) of the complete short-stack, as all the entering and exiting gas shared the same manifold in the short-stack, (3) single-cell voltage, measured between the anode and the cathode, (4) short-stack voltage, measured between the anode of the TA and the cathode of the TC, and (5) voltage of the individual cells in the short-stack, measured between the anodes and cathodes of the respective cells. Additionally, ΔVoltage, defined in Chapter 3.5, is used to compare the single-cell and short-stack voltages.

To facilitate the comparison of the single-cell and short-stack voltages, the differential voltage (ΔVoltage) between the absolute value of three times single-cell voltage ($U_{\text{single-cell}}$) minus the absolute value of the short-stack voltage ($U_{\text{short-stack}}$) is used (Equation 3.4). A value of zero corresponds to the same performance of short-stack and single-cell regarding the cell voltages.

$$\Delta\text{Voltage} = 3 \cdot \mid U_{\text{single-cell}} \mid - \mid U_{\text{short-stack}} \mid \tag{3.4}$$

Chapter 4

Results and Discussion

4.1 Assessing Various CO_2 -to-CO Flow-Cell Concepts

As discussed in the preceding chapter, various flow-cell designs can be used to perform the CO2-to-CO electrolysis, each with individual characteristics in terms of the performance indicators. Most frequently discussed are the flow-cell concepts with an MEA and the GDE-flow-cell.

In this chapter, hard data for these flow-cell concepts are generated to evaluate their performances based on the performance indicators introduced in Chapter 2.2. Different configurations of the flow-cell concepts are tested following the experimental protocol presented in Chapter 3.5.

Flow-Cell Concepts

All experiments were performed with flow-cell configurations that enabled a steady process. Non-steady-state configurations using sacrificial agents or consumable electrolytes were not evaluated as the chosen performance indicators are not suited to account for the added cost of these consumables and the result would be falsified.

Hence, the PEM was implemented in a GDE-flow-cell operating with H_2SO_4 as an anolyte. The same electrolyte configuration enables a

steady-state process with the BPM. Since the water dissociation also allows the use of alkaline electrolytes the experiment with the BPM is performed with 1M KOH as anolyte as well.

The AEM was tested as a separator in the GDE-flow-cell operating with 1 M $KHCO_3$ as anolyte and catholyte. The configuration with similar electrolytes at the anode and cathode can be beneficial since the conversion of the charge carrier (HCO_3^-, CO_3^{2-}) at the membrane surfaces does not appear. However, the investigation of CO_2 formation at the anode is rather difficult with this configuration. It is not possible to determine if the CO_2 that appears in the anolyte originates from the anolyte or the HCO_3^-/CO_3^{2-} transport from the cathode to the anode. Therefore, an experiment is performed with the AEM in a GDE-flow-cell operating with H_2SO_4 as anolyte. In this configuration, the CO_2 formation can be traced to the cathode side of the cell.

Furthermore, the AEM was implemented in the MEA, in which it acts as an electrolyte. This MEA design was tested with a 10 mM $KHCO_3$ solution as anolyte. The low-concentrated electrolyte was chosen to reduce the risk of salt precipitation at the cathode. In terms of stacking in further studies, the low-concentrated anolyte can be favorable to reduce the formation of shunt currents. The BPM and the PEM create in contrast to the AEM, an acidic environment at the cathode, which leads to low selectivity toward CO. Thus, the MEA was solely tested with the AEM.

Assessing the Performance

In Table 4.1, the flow-cell configurations, the reversible voltage E calculated according to Equation 2.3, and the results of the electrochemical experiments are presented.

Table 4.1: Flow-cell configurations, the reversible voltage E calculated according to Equation 2.3, and the values of the performance indicators at 100 mA/cm².

GDE flow-cell								
Membr.	Anolyte	Catholyte	FE(CO) [%]	U_{Cell} [V]	E [V]	$\epsilon_{(CO)}$ [%]	EPC [$\frac{kWh}{Nm^3}$]	$\frac{CO_2}{O_2}$
PEM	1 M H_2SO_4	1 M $KHCO_3$	93.63	-4.69	-1.59	26.35	10.98	-
BPM	1 M H_2SO_4	1 M $KHCO_3$	92.31	-5.39	-1.59	22.59	12.81	0.1
BPM	1 M KOH	1 M $KHCO_3$	92.70	-4.83	-1.17	25.36	11.42	-
AEM	1 M H_2SO_4	1 M $KHCO_3$	92.77	-4.28	-1.59	28.56	10.13	2.30
AEM	1 M $KHCO_3$	1 M $KHCO_3$	93.02	-4.63	-1.33	26.52	10.92	3.02
Flow-cell with MEA								
AEM	0.01M $KHCO_3$	-	93.74	-2.99	-1.59	41.39	6.99	2.08

Selectivity

With FE(CO) $\geq 90\,\%$, the obtained results show similar selectivity for all flow-cell configurations with sufficient suppression of the HER. It must be emphasized that no other products than CO and H_2 were detected in the gas phase. For all experiments a total FE (CO + H_2) of 98 % $\pm 3\,\%$ was determined. The FE(CO) is primarily influenced by the cathode, and since the cathode side of the GDE-flow-cells is similar for all configurations, the CO_2 reduction reaction is not visibly influenced by the change of the anode side of the reactors.

Cell Voltage

Taking the GDE-flow-cell with the PEM as a reference, the configurations with the BPM operate at higher U_{Cell}, and the configurations with the AEM operate at lower U_{Cell}.

Regarding the BPM, higher U_{Cell} results from the larger overpotential of the BPM, which is driven by the thicker membrane compared to the

PEM and by the formation of OH^- within the two layers of the BPM. The impact is most visible in the comparison of the GDE-flow-cell with the PEM and the BPM configuration with the same electrolytes. In both configurations, the reaction environments at the electrodes are similar, with a $pH = 0$ at the anode (1 M H_2SO_4) and a $pH = 8.7$ (1 M $KHCO_3$) at the cathode. For both configurations, a $E = -1.59$ V can be calculated (Equation 2.4) when considering the OER (Equation 2.14) at the anode and the reduction of CO_2 to CO at the cathode (Equation 2.10). Hence, only the exchange of the membrane leads to an U_{Cell} increase.
Regarding the pH shift performed at the anode to $pH = 14$, a lower electrode potential at the anode is generated. Following Equation 2.4, a reversible cell voltage of $E = -1.17$ V can be calculated for the cell. Accordingly, the GDE-flow-cell with the BPM operates at lower U_{Cell}, when the alkaline anolyte is present (Equation 2.4). However, the reduction of the anodic electrode potential is insufficient in compensating for the larger overpotential of the BPM in comparison to the PEM.

In terms of the GDE-flow-cells, the swapping from the PEM to the AEM reduces U_{Cell}. This is particularly unexpected, since the conductivity of the AEM for the charge carriers HCO_3^- or CO_3^{2-} is lower than the conductivity of the PEM for the H^+ ions. Thus, the membrane resistance for the charge carriers is not dominating U_{Cell} in the investigated cell design. A more significant impact can be attributed to the ionic conductivity of the electrolytes, considering the two times 2 mm thick electrolyte chambers. As for the catholyte, the same electrolyte was used for all experiments with the GDE-flow-cell, however, differences in pH values have been determined, which can influence the conductivity of the catholyte. In Figure 4.1 the pH value of the catholyte in experiments with the PEM and the AEM in the GDE-flow-cell are illustrated over time.

In all experiments, an initial pH value of 8.6 is observed, which increases over time. For experiments with the PEM, a pH = 9.25 is determined at the end of the experiment, while in experiments with the AEM, the pH increases to 9.5 with H_2SO_4 as anolyte and to 9.9 when $KHCO_3$ is used as anolyte.

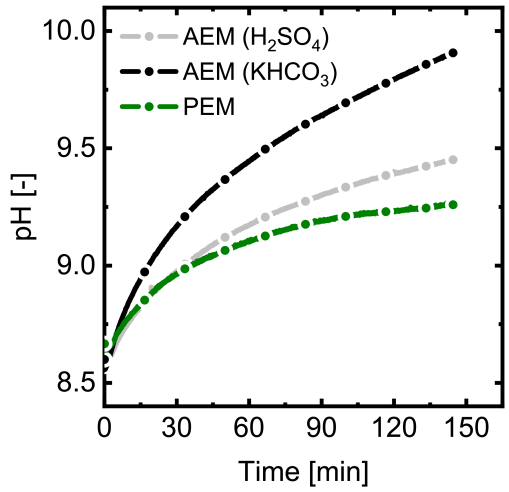

Figure 4.1: pH values of catholyte over the time for the experiments with GDE-flow-cell containing the PEM, or the AEM with H_2SO_4 and $KHCO_3$ as anolytes.

The results demonstrate, that the swapping from the PEM to the AEM leads to a higher pH of the catholyte, which increases the conductivity of the catholyte. It can be assumed, that this increase of conductivity compensates for the higher resistance of the AEM and thus reduces U_{Cell} in comparison to the GDE-flow-cell with the PEM. As for the configuration with the AEM and the H_2SO_4 as anolyte, this effect is mitigated by the low pH of the anolyte, however, U_{Cell} is lower than for the GDE-flow-cell with the $KHCO_3$ solution as anolyte. This observation is attributed to the higher ionic conductivity of 1M H_2SO_4 ($\sigma = 400\,\mathrm{mS/cm}$) compared to 1 M $KHCO_3$ ($\sigma = 73\,\mathrm{mS/cm}$). It is noteworthy, that a pH shift from pH = 0 to pH= 8.6 appears at the anode when using 1 M $KHCO_3$ instead of 1 M H_2SO_4, which leads to a reduction of $E = -1.59\,V$ to $E = -1.33\,V$. By the pH shift, E, and hence U_{Cell} is reduced, however, this effect is not visible due to the U_{Cell} increase caused by the low conductivity of the $KHCO_3$ solution at the anode.

The discussion around the conductivity indicates the significant impact of the electrolyte gaps on U_{Cell}. Their influence is even more highlighted when comparing U_{Cell} of the GDE-flow-cells with the AEM and

for the flow-cell with the MEA. With the MEA, the electrolyte gaps are eliminated, and the electrode distance is reduced to the thickness of the membrane, leading to the lowest U_{Cell}. However, the MEA operated at a voltage of 2.99 V at a $j = 100\,\mathrm{mA/cm^2}$. In a different study, an MEA assembled with the same electrodes and membrane was operated with 3 V at $j = 200\,\mathrm{mA/cm^2}$.[112] Unfavorable impact can be attributed to the flow-fields, which possess an entrance and exit channel for the media flows at the front side of the plates. These channels reduce the current collector contact area to the GDE and cause leakage of the flow-cell, possibly leading to higher voltages. An image of the flow-fields is provided in the Appendix C Figure C.1.

Energy Efficiency

Considering Equation 4.1 as the overall reaction in the CO_2-to-CO electrolyzer, a $\Delta G = 255\,\mathrm{kJ/mol}$ can be derived for the calculation of $\epsilon_{(CO)}$. Based on this assumption, $\epsilon_{(CO)}$ is mainly influenced by the FE(CO) and U_{Cell}. Since only minor differences in FE(CO) are visible between the different cell configurations, U_{Cell} dominates the variation in $\epsilon_{(CO)}$. In this manner, the GDE-flow-cells with the BPM show the lowest $\epsilon_{(CO)}$, while the flow-cell with the MEA outperforms the other configurations. It must be emphasized, that only the flow-cell with the MEA is approaching the theoretical maximum of $\epsilon_{(CO)}$ = 62 % that has recently been introduced for alkaline CO_2-to-CO reduction coupled with the OER[34].

$$\mathrm{CO_2} \rightleftharpoons \mathrm{CO} + \frac{1}{2}\mathrm{O_2} \tag{4.1}$$

CO_2/O_2

The values of the CO_2/O_2 ratio given in Table 4.1, indicate a CO_2 evolution at the anode for all cell configurations containing an AEM, and for the configuration with the BPM operating with H_2SO_4 as anolyte. The CO_2/O_2 ratio calculated for the BPM is with 0.1 significantly lower than for the experiments with the AEMs ($\geq$ 2.08). In experiments with the

BPM and the KOH solution as anolyte as well as in experiments with the PEMwith the PEM, no traces of CO_2 were determined in the anode gas.

In terms of the BPM, the CO_2 evolution at the anode originates from the transport of ions from the cathode to the anode side. HCO_3^- ions cross through the PEM side of the BPM due to the low pH value within the membrane, to thereupon cross the AEM side of the BPM as CO_3^{2-} ions.[72,93] Given an acidic environment at the anode, such as in the experiments with H_2SO_4 as anolyte, these ions react to CO_2, which can be determined in the GC measurement. Whereas in experiments with the KOH solution as anolyte, these ions remain in the solution and can not be traced by the applied analytical methods.

In experiments with the AEMs, larger amounts of CO_2 were detected in the anolyte gas. While one can argue, that the CO_2 formation at the anode in experiments with $KHCO_3$ solutions originates from the active degassing of the anolyte, the cathode side of the reactor represents the only CO_2 source in experiments with H_2SO_4 solution as anolyte. This indicates that the CO_2 formation at the anode is generated by the HCO_3/CO_3^{2-} transport through the AEM from the cathode to the anode side. A CO_2/O_2 value of two, which has been observed in experiments with the MEA, describes a dominating transport of CO_3^{2-} ions through the AEM. This observation is in alignment with results presented in the literature for similar MEAs at the same current density.[82]

Overall, the calculated CO_2/O_2 ratios reflect a limitation of the AEMs, which is the transport of valuable CO_2 from the cathode to the anode side, which leads to the formation of a CO_2/O_2 mixture. This phenomenon has not been observed with the PEM, and has been suppressed by the BPM to a large extend. Thus, for flow-cells with AEMs, an energy-intensive downstream process to recover the CO_2 from the anode gas and its impact on the overall energy efficiency of the process needs to be considered.

Conclusion on Flow-Cell Concepts

In the performed study, various flow-cell designs for the CO_2-to-CO electrolysis are tested in the same setup to provide a basis for comparing the performances in terms of selectivity, U_{Cell}, energy efficiency, and CO_2 to O_2 ratio in the anode gas. A GDE-flow-cell was investigated with a PEM, a BPM, and an AEM. Furthermore, an MEA with an AEM was tested in a flow-cell.

Similar selectivity with sufficient suppression of the HER was observed for all tested flow-cells. In all configurations, the cathode was provided with an alkaline to neutral environment, thus the selectivity was not influenced by the different variations of the flow-cells.

In contrast, U_{Cell} was influenced by various factors. For one, the membranes´ overpotential and resistances generally increased U_{Cell} with growing values. However, the ion exchange capacity of the membranes affects the electrolytes, which determined U_{Cell} to the largest extent due to the thick electrolyte gaps. For instance, the swapping from PEM in a GDE-flow-cell led to a decrease in U_{Cell} despite the higher membrane resistance of the AEM. The impact of the membrane resistance on U_{Cell} was less significant than the change of pH value of the catholyte, and hence of its conductivity. A similar observation was made when performing a pH shift at the anode to higher pH values, to reduce the electrode potential of the anode and thus to decrease U_{Cell}. As for the pH shift, the higher pH value decreased U_{Cell}, however, once again the conductivity of electrolytes, which were introduced for the pH shift, influenced the U_{Cell} to a larger extent.

Overall, the experiments revealed, that the electrolyte gaps and their properties mostly define U_{Cell}. This hypothesis was confirmed in the experiment with the MEA, which outperformed all other configurations in terms of U_{Cell} due to eliminating the electrolyte gaps.

The evaluation of the performance via the CO_2/O_2 ratio on the anode gas aligns with findings in the literature and demonstrates the limitation of the flow-cells with AEMs. While for the GDE-flow-cell with the

PEM no CO_2, and for the BPM only small amounts were detected in the anode gas, a CO_2/O_2 ratio of larger than two was detected when using the AEMs. An energy-intensive recovery of the CO_2 from the anode gas needs to be considered in the process design, possibly diminishing the energy efficiency of the overall process.

4.2 Impact of Flow-Fields in GDE-Flow-Cell

This study aims to elevate the performance of a GDE-flow-cell under the boundary condition of creating a stackable flow-cell architecture. The GDE-flow-cell containing a PEM, which has been presented in Chapter 4.1 is investigated (Figure 4.2). This flow-cell configuration is chosen, since it operates at lower U_{Cell} than the configuration with the BPM, and the crossover of CO_2 to the anode side is prevented. Furthermore, the GDE-flow-cell is more flexible than the MEA, which facilitates the swapping of cell components.

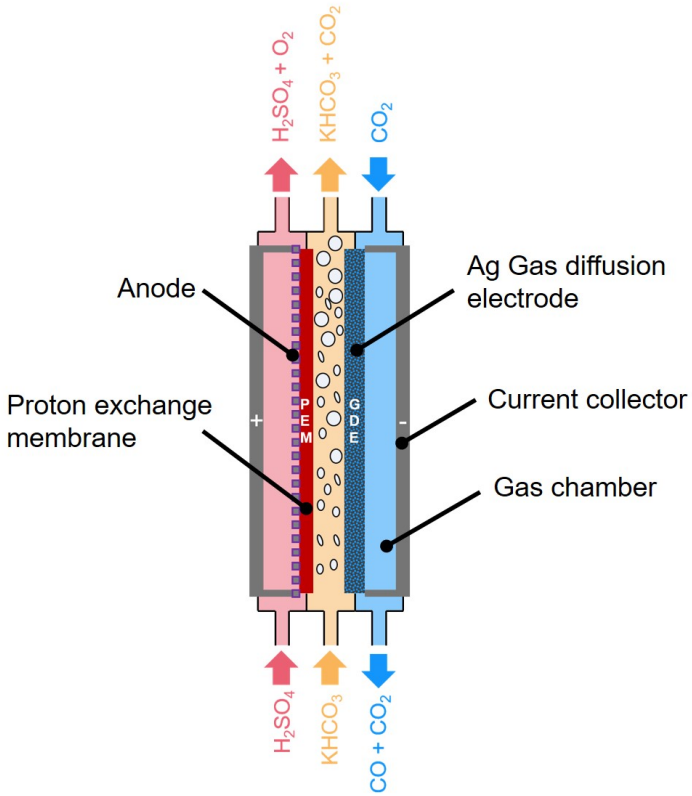

Figure 4.2: Illustration of a flow-cell assembled with a zero-gap anode, proton exchange membrane, and an Ag GDE, operating with H_2SO_4 as anolyte and $KHCO_3$ as catholyte. This figure is adapted from [1].

In the presented study, a zero gap anode is introduced to reduce U_{Cell}, and different gas flow-fields are investigated to stabilize the GDE mechanically and to reduce the excessive use of CO_2. Experiments with diluted and reduced feed gas supply were performed to accent the effect of the flow-field architecture. The experiments with diluted CO_2 feed gas are also reminiscent of the direct CO_2-to-CO conversion in flue gas and it can portray the cell's behavior towards the cell's exit, where the feed gas is diluted due to the formation of products. The experiments with pure CO_2 gas were performed to increase the product concentrations in the product gas and to detect possible mass transport limitations at low feed gas volume flows. The experimental protocol is presented in Chapter 3.5. The influence of the flow-fields was measured in the selectivity, U_{Cell}, and CO_2 conversion of the flow-cell. The indicators are given by the FE(CO), U_{Cell}, and the concentrations of CO (φ_{CO}) and CO_2 (φ_{CO_2}) in the product gas of the cathode.

Flow-Field Designs

To design a stackable flow-cell, flow-fields providing a supporting structure to the GDE and managing the feed gas distribution were implemented at the gas side of the flow-cell. In experiments, two flow-fields with different gas path architectures were investigated and their influence was compared to the cell's performance with an open frame current collector ($Chamber_1$) (Figure 4.3(a)).

One flow-field provides a meander gas path (Meander), and the other one ($Rake_1$) contains a disconnected gas path with several interlocking branches similar to the interdigitated flow-field presented in Chapter 2.6. The open frame current collector contacts the GDE via the GDE's edges and thereby provides a gas chamber over the full active GDE area with a volume of 4 ml. The maximized GDE-gas contact area given by $Chamber_1$ enables the feed gas to have a minimal diffusion length to the entire electrocatalyst area and can thus increase the conversion of CO_2-to-CO. But it also implies the reduction of the GDE-current collector contact

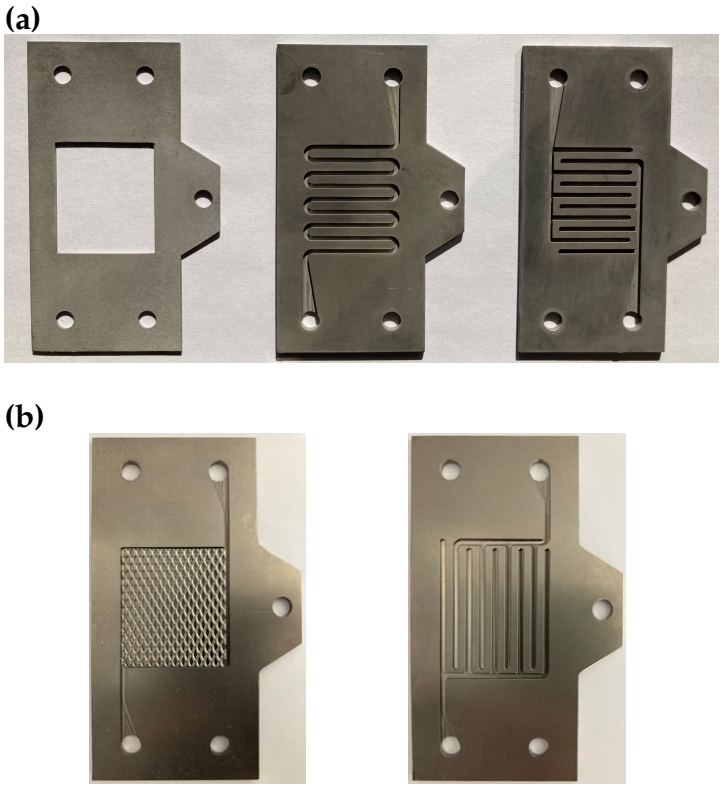

Figure 4.3: (a) Images of the first generation of the current collector providing a gas chamber ($Chamber_1$, (a)-left), the flow-field with a meander gas path (Meander, middle) and the flow-field with interlocking gas path branches ($Rake_1$, (a)-right), (b) Images of the second generation of the open frame current collector providing a gas chamber with an implemented titanium mesh (Chamber2, (b)-left) and the second generation of the rake flow-field providing the interlocking branches in a vertical orientation ($Rake_2$, (b)-right). The figure is adapted from [1].

area to the edges of the GDE, causing the GDEs' electric in-plane resistance to influence U_{Cell} to a greater extent. The GDE-current collector contact areas of Meander and $Rake_1$ are about 45 % and 50 % of the active GDE area, and are thus larger than the one of $Chamber_1$. Consequently, the impact of the GDEs' electric resistance on U_{Cell} can be reduced with these flow-fields. For Meander, the GDE-gas contact area can be determined to be 55 % of the GDE's active area and is thus considerably lower than with $Chamber_1$. The reduction of the GDE-gas contact area could

diminish the CO_2-to-CO conversion, by hindering the transport of CO_2 to and the products from the electrocatalyst layer. Evaluating the GDE-gas contact area for $Rake_1$ is less straightforward. The disconnected gas path forces the feed gas through the back side of the GDE and generates at best a GDE-gas contact area over the full active GDE area. Furthermore, the branches in $Rake_1$ essentially segment the gas compartment, each bearing individual concentration gradients. Hence, $Rake_1$ induces positive effects on FE(CO) and U_{Cell} simultaneously, by creating a more efficient trade-off between the GDE-gas contact and GDE-current collector contact area.

In addition, a second generation of the open frame current collector (Chamber2) and the rake flow-field ($Rake_2$) (Figure 4.3(b)) were designed and tested based on the results obtained with the first generation. Chamber2 provides a gas chamber with a depth of 1 mm and a volume of 1 ml, in which a titanium expanded metal (1 mm thick) with a mesh width of 4x2 mm was inserted as a baffle. To reduce the cell voltage and to reduce the formation of concentration gradients possibly forming in $Chamber_1$, Chamber2 provides a larger GDE-current collector contact area and a gas chamber with a smaller volume. $Rake_2$ was designed similarly to $Rake_1$ but with a vertical orientation of the branches, to accelerate the removal of possible permeate in the gas chamber, which, if not removed from the gas chamber, reduces the cell performance by blocking the GDE-gas contact area[113].

Influence of Flow-Fields

The results of the electrochemical experiments with the flow-cell operating with diluted feed gas and containing $Chamber_1$, $Rake_1$, and Meander are depicted in Figure 4.4, showing the determined FE(CO) (left) and U_{Cell} (right) over λ and p_{CO_2} in the feed gas. In every experiment, a decreasing FE(CO) for decreasing λ-values can be observed. With $Chamber_1$ and $Rake_1$, FE(CO) maintained over 90 % for $\lambda \geq 3$, with Meander FE(CO) $\geq 90\%$ was determined for $\lambda = 4.5$. At $\lambda = 1$ FE(CO) de-

creased to a value of 35 % in every experiment. In all experiments U_{Cell} increased with decreasing λ. Similar U_{Cell} were measured in experiments with $Rake_1$ and $Chamber_1$, increasing from $U_{Cell} = 4.1V$ at $\lambda = 4.5$ to $U_{Cell} = 4.3V$ at $\lambda = 1$. Lower U_{Cell} can be observed for Meander decreasing from $U_{Cell} = 3.75V$ at $\lambda = 4.5$ to $U_{Cell} = 3.9V$ at $\lambda = 1$.

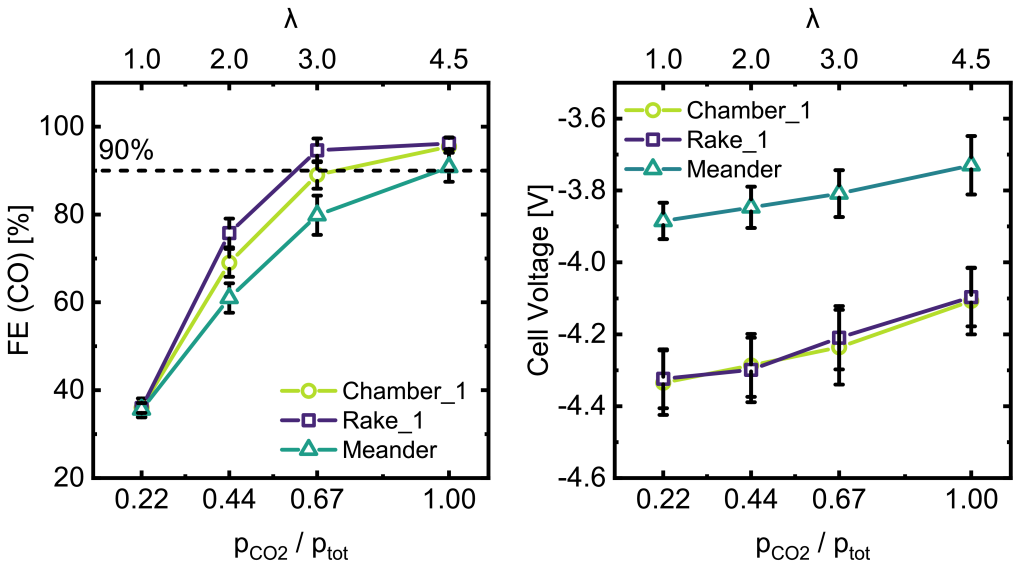

Figure 4.4: FE(CO) (left) and cell voltage (right) over different λ-values and p_{CO_2} in feed gas for experiments with $Chamber_1$, $Rake_1$ and Meander at 100 mA/cm^2. The figure is adapted from [1].

The results in Figure 4.4 show a relation between the GDE-gas contact area and FE(CO) for diluted CO_2 supply. $Rake_1$ and $Chamber_1$ provide the largest GDE-gas contact area and show the highest FE(CO). A sufficient suppression of the HER (FE(CO) $\geq 90\%$) could be maintained for $Rake_1$ and $Chamber_1$ for $\lambda \geq 3$ ($p_{CO_2} \geq 0.67$). Further reduction of CO_2 supply led to an increase of the HER. Hence, higher U_{Cell} were determined with decreasing λ in every experiment. Minimal U_{Cell} were determined with Meander. As Meander provides a comparatively large GDE-current collector contact area, the electrical current, following the lowest electrical resistance, is led along the titanium flow-field rather than along the in-plane area of the GDE (Figure 4.5a). The electrical ohmic losses

and thus the sum of the ohmic losses are reduced. The ohmic losses can be considered as a part of the loss mechanisms in an electrolyzer affecting the cell voltage (Figure 4.5d), hence a lower U_{Cell} is determined for Meander than for $Chamber_1$. With $Rake_1$ however, the determined U_{Cell} are similar to U_{Cell} determined for $Chamber_1$ despite the larger GDE-current collector contact area provided by $Rake_1$. As illustrated in Figure 4.24b, it is possible, that forcing the gas through the GDE with $Rake_1$ increases the pressure on the gas side, the GDE is then pushed towards the catholyte chamber, and the GDE-current collector contact area is reduced. This effect forces the electric current along the in-plane area of the GDE rather than along the titanium flow-field and increases the electrical ohmic losses. To verify this hypothesis, a spacer needs to be implemented inside the catholyte chamber. This spacer needs to complete the force closure within the cell to ensure full contact of the GDE to $Rake_1$ (Figure 4.5c).

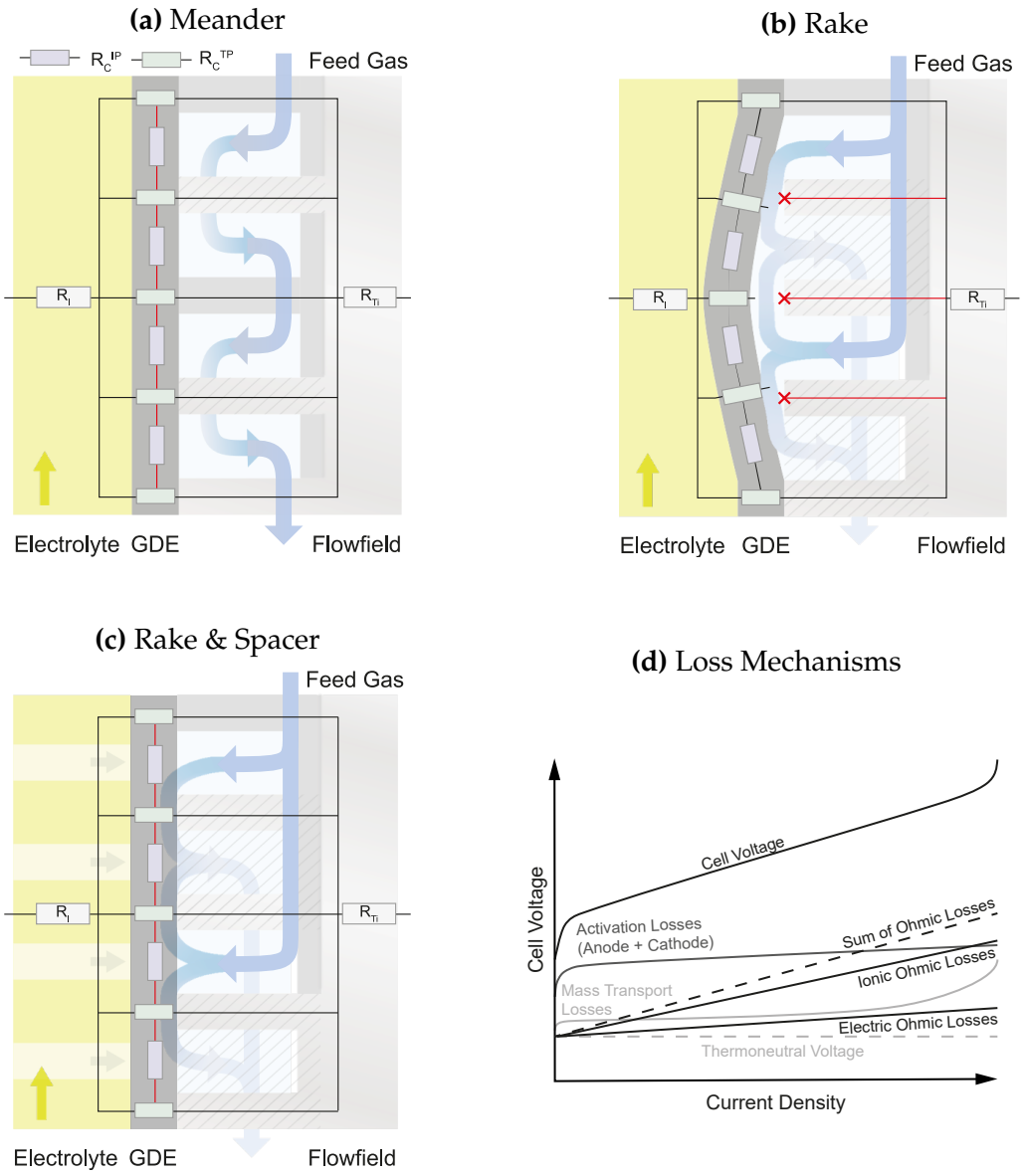

Figure 4.5: (a-c) Schematic illustration of the electrical resistances of the titanium flow-field (R_{TI}), the GDE in plane resistance (R_C^{IP}), the GDE through plane resistance (R_C^{TP}), the ionic resistance of the electrolyte (R_I) and the behavior of GDE on different flow-fields a) GDE lies vertical on the meander, electrical current can pass along the flow-field b) pressure generated by feed gas in $Rake_1$ pushes GDE towards electrolyte and decreases GDE-current collector contact area, electrical current path is forced through in plane area of the GDE c) force induced by a spacer pushes GDE onto $Rake_1$, electrical current can pass along flow-field d) influence of loss-mechanisms possibly effecting the cell voltage of electrolyzers over current density, expanded adaption from Endrődi et al. The figure is adapted from [1].

Spacer Implementation

In electrochemical cells, spacers are implemented in open areas, in which force transmission is occurring. The main function of the spacer is to fixate cell components in their position, however, the spacer can simultaneously enhance the mixing of media flows in the open areas. A widespread challenge is the spacer shadow effect, which describes the blockage of the ion transport when non-conductive spacers are used.[114] Furthermore, spacers in electrolyte chambers can hinder the removal of gas bubbles by blocking their path toward the chamber's exit. This causes a reduction of the ionic conductivity through the electrolyte chamber, leading to an increase in cell voltage and a decrease in the overall cell performance.[114,115]. To minimize this issue and to avoid the spacer shadow effect, an ionically conductive hydrophilic spacer was implemented. Ion exchange resin (IER) beads were used to fill the catholyte chamber.

The use of IERs in electrodionization processes or electrodialysis, to increase the conductivity in electrolyte chambers to reach cell voltage reduction, has already been shown in literature[116–119]. Regarding CO_2 electrolysis, a hydrophilic and strongly acidic cation exchange resin was employed in CO_2 to formic acid electrolysis[17]. The IER was implemented as a flow-through polymer electrolyte, to increase conductivity in the electrolyte chamber. In this work, the same IER was implemented as a spacer. Its effect on the electrolyte's conductivity was measured. The exact procedure of the conductivity measurement is described in Appendix A. A conductivity of 55 mS/cm was measured in a test tube with a 1M $KHCO_3$ solution, and the IER, for a pure 1M $KHCO_3$ solution a conductivity of 73 mS/cm was determined. As observed in Chapter 4.1 the conductivity of the media in the electrolyte gaps significantly influences U_{Cell}, thus an increase in U_{Cell} can be expected when the spacer is implemented.

The results obtained in the electrochemical experiments with the cell containing the spacer and operating with diluted feed gas are illustrated in Figure 4.6. For the first and the second series of flow-fields, the determined FE(CO) and U_{Cell} are shown over λ and p_{CO_2}. In all experiments a

decrease of FE(CO) with decreasing λ can be observed, starting at FE(CO) $\geq 90\%$ for $\lambda = 4.5$. With Rake_1, Rake_2 and Chamber_1, FE(CO) remained over 90 % until $\lambda = 3$ and decreased with further reduction of λ to 35 % (Rake_1, Chamber_1) and 37 % (Rake_2) for $\lambda = 1$. A more rapid decrease of FE(CO) can be observed for Meander and Chamber2, with a determined FE(CO) = 80 % for $\lambda = 3$ decreasing to 30 % and 28 % for $\lambda = 1$.

In every experiment U_{Cell} increased with decreasing λ. With Rake_1 and Rake_2, $U_{Cell} = 3.88V$ and $U_{Cell} = 3.9V$ was determined for $\lambda = 4.5$ increasing to $U_{Cell} = 4V$ and $U_{Cell} = 4.05V$ for $\lambda = 1$. Higher cell voltages were determined with Meander and Chamber2 increasing from $U_{Cell} = 3.95V$ and $U_{Cell} = 4V$ for $\lambda = 4.5$ to $U_{Cell} = 4.1V$ at $\lambda = 1$. Similar to previous experiments, the highest cell voltages were determined with Chamber_1 increasing from $U_{Cell} = 4.1V$ at $\lambda = 4.5$ to $U_{Cell} = 4.3V$ at $\lambda = 1$.

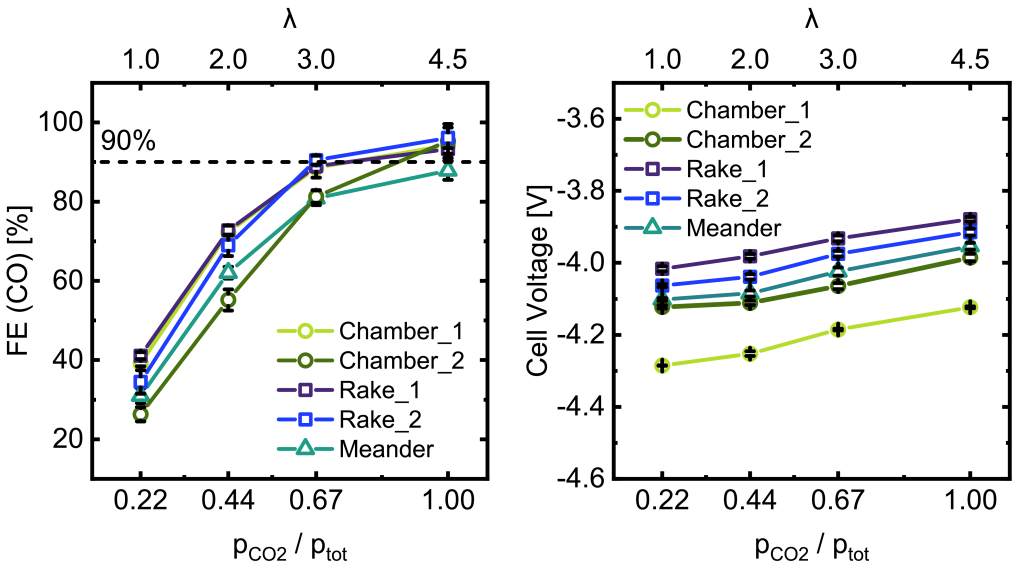

Figure 4.6: FE(CO) (left) and cell voltage (right) over different λ-values and p_{CO_2} in feed gas for experiments with Chamber_1, Chamber2, Rake_1, Rake_2 and Meander in cell with spacer at 100 mA/cm^2. The figure is adapted from [1].

The determined FE(CO) values for Chamber_1, Rake_1, and Meander show similar characteristics to the previous results without the spacer

(Figure 4.4). In both cases, higher FE(CO) values were obtained when larger GDE-gas contact areas were provided. $Rake_2$ provides a similar GDE-gas contact area to $Rake_1$ and similar FE(CO) values were obtained. Despite the large GDE-gas contact area, given by Chamber2, a stronger decrease of FE(CO) can be observed compared to the other experiments. Due to the mesh structure in Chamber2, it is possible, that the permeate accumulates in the gas chamber, blocks part of the GDE-gas contact area, and thereby diminishes the conversion of CO_2-to-CO. It can be assumed that the CO_2 feed gas is not distributed over the entire GDE area by the mesh structure. Nevertheless, the mesh structure increases the GDE-current collector contact area of Chamber2 compared to $Chamber_1$ and reduces U_{Cell}. However, the low FE(CO) indicates an increased appearance of the HER resulting in higher U_{Cell} for Chamber2 compared to the flow-fields.

Comparing the U_{Cell} values for $Rake_1$ obtained with (Figure 4.6) and without (Figure 4.4) the spacer, a significant decrease of U_{Cell} from $4.1V$ to $3.88V$ for $\lambda = 4.5$ can be observed with the spacer implementation. As illustrated in Figure 4.7, the spacer provides a structure in the catholyte chamber which enables force closure through the entire cell area. The GDE is pressed onto $Rake_1$ and the electric current is distributed in the metallic flow-field rather than in the carbon-based GDE (Figure 4.5c). This reduces the electrical ohmic losses and U_{Cell} for the cell with the spacer compared to the cell without the spacer.

The measurement of U_{Cell} determined with the spacer shows significantly reduced noise, than the ones without the spacer. For a better illustration of this effect, U_{Cell} is shown in figure 4.8 over the full time for the experiments with Meander. The results of the experiment without the spacer are depicted for different λ in Figure 4.8a and with the spacer in Figure 4.8b. Without the spacer, the cell operated at an average $U_{Cell} \leq 3.8V$ for $\lambda = 4.5$, with the implemented spacer an average value of $U_{Cell} = 3.95V$ was determined. Comparing U_{Cell} at lower λ, similar differences between the two experiments can be observed.

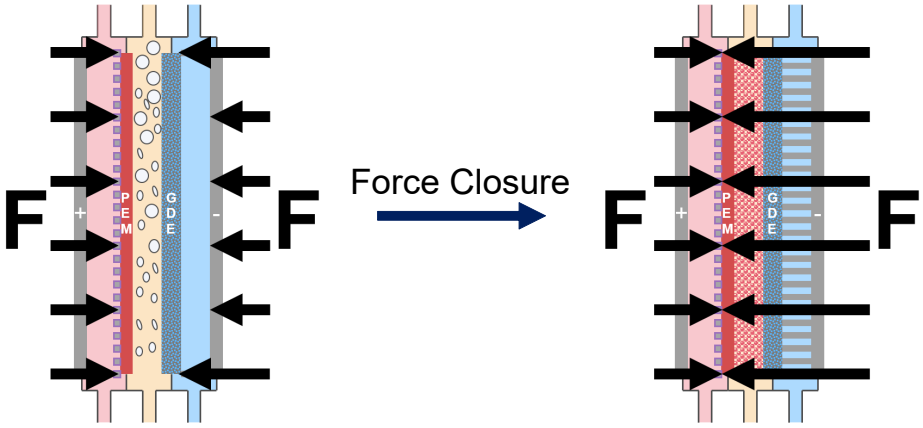

Figure 4.7: Illustration of the force closure through the cell. Non-complete force closure for a cell without the spacer and open frame current collector (left) and complete force closure through the cell with spacer and flow-field (right). The figure is adapted from [1].

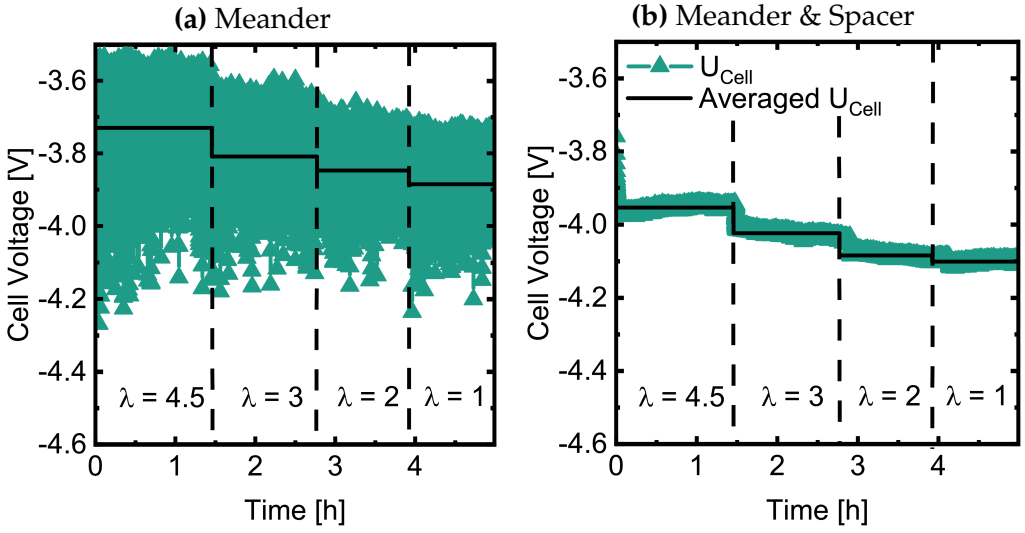

Figure 4.8: Voltage measurements and averaged U_{Cell} over time for experiment with Meander for different λ at 100 mA/cm^2.(a) Voltage measurement on a cell without the spacer, (b) voltage measurement with an ionically conductive spacer shows a reduction of bubble-induced noise in the measurement of cell voltage. The figure is adapted from [1].

Figure 4.8a shows extreme noise (e.g. Standard-deviation = 0.08 V ($\lambda = 4.5$)) in the voltage measurements, which indicate the voltage instabilities caused by the bubble formation in the catholyte chamber. Figure 4.8b shows in contrast a more stable (e.g. Standard-deviation = 0.01 V ($\lambda = 4.5$)) but higher U_{Cell}. To describe the effect of the spacer on U_{Cell}, the current flow is illustrated in figure 4.9a for a cell containing $Chamber_1$ without a spacer and for a cell containing a flow-field and the spacer. Without the spacer, the current flow is forced to evade around the formed bubbles in the catholyte chamber and is afterward led along the GDE to $Chamber_1$. These deflections of the current flow lead to a local increase of the current density and voltage instabilities observed in Figure 4.8a. As illustrated in Figure 4.9b, the deflections of the current flow can be avoided by implementing the ionically conductive spacer, which bridges the bubbles and provides a linear current flow through the catholyte chamber. U_{Cell} is therefore dependent on the conductivity of the IER, which was determined in this work to be lower in combination with the 1M $KHCO_3$ solution, than the conductivity of the pure 1M $KHCO_3$ solution. This accompanies the observation of the higher U_{Cell} determined with the spacer compared to the experiment without the spacer. Furthermore, the linear current flow is completed by the flow-field implementation, which provides a larger GDE-current collector contact area and thereby prevents the deflection of the current flow along the GDE.

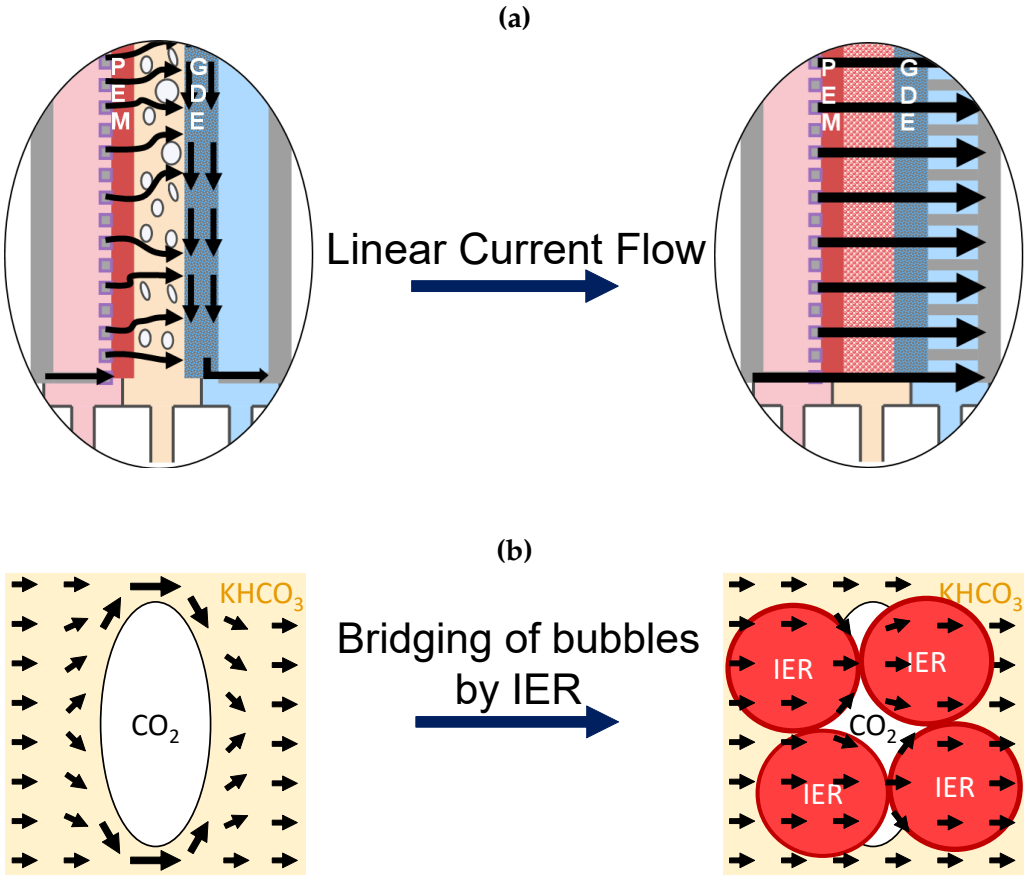

Figure 4.9: (a) Illustration of the current flow through the cell. ((a)-left) Non-linear current flow for cell with open frame current collector and without the spacer, ((a)-right) linear current flow for cell with spacer and flow-field. (b) Illustration of current flow through part of the catholyte chamber, ((b)-left) current flow in the chamber without a spacer evades around a CO_2 gas bubble, ((b)-right) Ion exchange resin (IER) bridges the CO_2 gas bubble and enables a more linear current flow. The figure is adapted from [1].

The results of the experiments performed with pure CO_2 supply and different λ are illustrated in Figure 4.10. For Chamber_1, Meander, Rake_1 and Rake_2, FE(CO) remained over 90 % for $\lambda \geq 2$ and decreases to 40 % for $\lambda = 0.5$. While Meander and Chamber_1 decline more rapidly, reaching only a FE(CO) of 67 % for $\lambda = 1$, for Rake_1 and Rake_2 a FE(CO) = 79 %

could be determined. The most rapid decrease of FE(CO) can be observed for Chamber2, decreasing from under 90 % for $\lambda = 2$ to 40 % for $\lambda = 0.5$. The results show an increase of U_{Cell} for decreasing λ for every experiment. Similar U_{Cell} were determined for $Rake_1$ and $Rake_2$, increasing from $U_{Cell} = 4.01V$ for $\lambda = 4.5$ to $U_{Cell} = 4.2V$ for $\lambda = 0.5$. For $\lambda = 0.5$ the same U_{Cell} was determined for Meander and Chamber2, but in both cases U_{Cell} increased from $U_{Cell} = 4.1V$ for $\lambda = 4.5$. The highest U_{Cell} were measured in experiments with $Chamber_1$, increasing from $U_{Cell} = 4.3V$ at $\lambda = 4.5$ to $U_{Cell} = 4.45V$ at $\lambda = 0.5$.

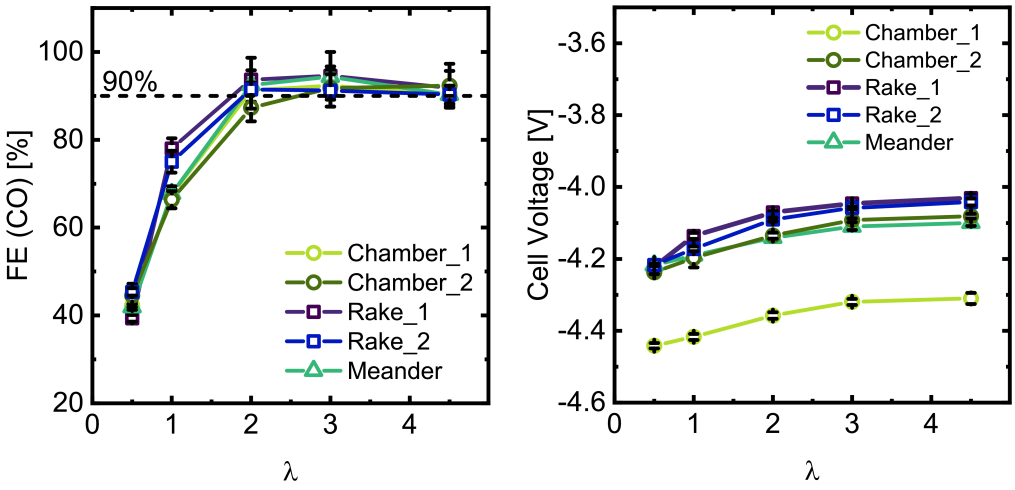

Figure 4.10: FE(CO) (left) and U_{Cell} (right) over λ for experiments with pure CO_2 feed gas for experiments with $Chamber_1$, Chamber2, $Rake_1$, $Rake_2$ and Meander in cell with spacer at 100 mA/cm^2. The figure is adapted from [1].

The results in Figure 4.10 show the positive effect of the optimized feed gas distribution over the GDE, performed by $Rake_1$ and $Rake_2$, on FE(CO) and U_{Cell} for low CO_2 supply ($\lambda = 1$). The effect becomes apparent in the comparison of the results obtained with $Rake_1$ and $Rake_2$ to the results obtained with $Chamber_1$. With $Chamber_1$ the maximum GDE-gas contact area is provided, however, with $Rake_1$ and $Rake_2$ a higher FE(CO) is determined for $\lambda = 1$. Possible mass transport limitations, appearing with $Chamber_1$, cause the formation concentration gradients in

the gas chamber not only along the GDE but also perpendicular to the GDE. Other than with $Rake_1$ and $Rake_2$ not all of the CO_2 which enters the $Chamber_1$ gas chamber is transported to the electrocatalyst surface and can be potentially converted to CO.

For the same experiments, the determined concentrations φ_{CO} and φ_{CO_2} in the product gas are illustrated over λ in figure 4.11. In all experiments a $\varphi_{CO} = 20\%$ for $\lambda = 4.5$ was determined, increasing with decreasing λ. At $\lambda = 1$ the highest φ_{CO} were measured for every experiment, with $Rake_2$ and Meander values of $\varphi_{CO} \geq 60\%$ were obtained. A further reduction of λ to 0.5 leads to a decrease of φ_{CO} with a maximum value of $\varphi_{CO} = 50\%$ obtained with $Rake_2$. A decrease of φ_{CO_2} with decreasing λ can be observed for all experiments. In all experiments, the highest values were measured with $\varphi_{CO_2} \geq 80\%$ for $\lambda = 4.5$. The fastest decrease of φ_{CO_2} was observed with Meander, decreasing under 10 % for $\lambda = 1$ and under 5 % for $\lambda = 0.5$. For $Rake_1$ and $Rake_2$ similar φ_{CO_2} were determined, decreasing to 20 % for $\lambda = 1$ and under 10 % for $\lambda = 0.5$ With $Chamber_1$ and Chamber2 the highers values of φ_{CO_2} were determined, decreasing to 30 % for $\lambda = 1$ and to 20 % for $\lambda = 0.5$.

φ_{CO} increases and φ_{CO_2} decreases with decreasing λ due to the reduction of the total feed gas volume flow and the high conversion rates. With φ_{CO_2} decreasing under 10 % in experiments with $Rake_1$, $Rake_2$, and Meander one can derive an increase of CO_2 consumption compared to experiments with $Chamber_1$ and Chamber2. In the case of $Rake_1$ and $Rake_2$, the increased consumption is accompanied by the higher FE(CO) determined in the experiments. Forcing the gas through the GDE with the interdigitated flow-fields thus enhances the CO_2 gas distribution to the catalytically active sites. For Meander the increased CO_2 consumption is related to an increase in HCO_3^- and CO_3^{2-} formation. It is reasonable to assume, that $Rake_1$, $Rake_2$, and Meander can overcome the aforementioned mass transport limitations anticipated for the $Chamber_1$ and Chamber $_2$. For the sake of complete perspective, it must be pointed out, that the higher CO_2 concentration in the product gas when implementing $Chamber_1$ and $Chamber_2$ not only hints at mass transport limitations

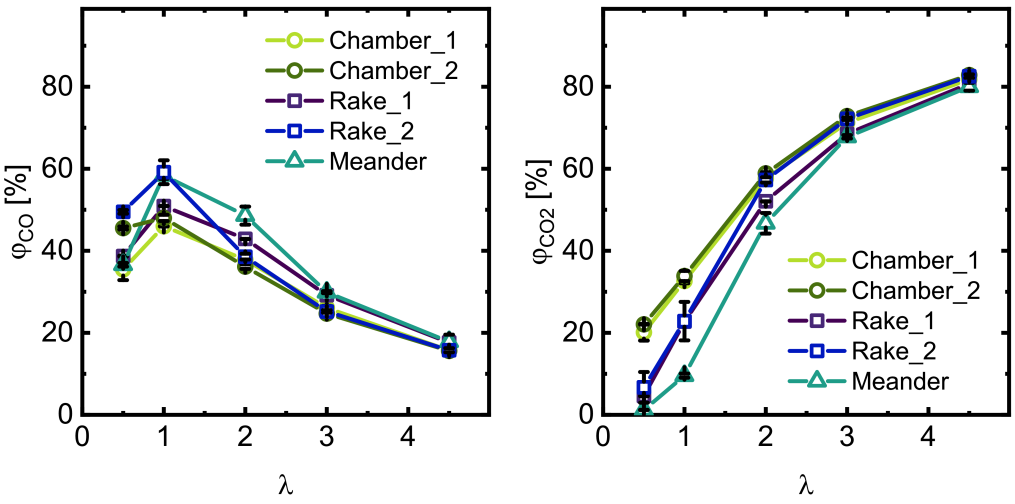

Figure 4.11: Concentration of CO (φ_{CO}) (left) and concentration of CO_2 (φ_{CO_2}) (right) in the product gas over λ for experiments with $Chamber_1$, Chamber2, $Rake_1$, $Rake_2$ and Meander in cell with spacer operating with pure CO_2 feed gas at 100 mA/cm^2. The figure is adapted from [1].

but also implies that bicarbonate formation is more dominant than the carbonate formation. Considering that the reaction of CO_2 with OH^- to HCO_3^- is faster than the reaction to CO_3^{2-}, one can conclude that the formation of CO_3^{2-} is reduced or does not appear at all.

Performance Evaluation

Considering the performance indicators, the modifications to the cell design increased the cell performance. Most evident becomes the performance enhancement when comparing the values of the performance indicators for the modified GDE-flow-cell in its different stages and the GDE-flow-cell from Chapter 4.1. For this purpose the extension of Table 4.1 is presented in Table 4.2. When dividing the different stages of modifications into (1) the implementation of the Zero-Gap anode (2) the implementation of the flow-fields and (3) force closure by spacer implementation, an enhancement of the performance indicators U_{Cell} and consequently $\epsilon_{(CO)}$ and EPC can be observed. The most significant impact can be observed for stages (1) and (3), while the impact of stage (3) has

already been discussed. In stage (1) ohmic losses in the cell are reduced by removing the anolyte gap with the Zero-Gap anode. Thus, the GDE-flow-cell operates at lower U_{Cell} which simultaneously increases $\epsilon_{(CO)}$ and reduces EPC. The FE(CO) in all stages vary in a range within the standard deviations ($\pm 3\,\%$), however, as already discussed, the modifications elevated FE(CO) when operating under reduced CO_2 supply.

Table 4.2: GDE-flow-cell configurations and performances at $100\,mA/cm^2$.

GDE-flow-cell with Zero-Gap anode						
Membrane	Flowfield	Spacer	FE(CO) [%]	U_{Cell} [V]	$\epsilon_{(CO)}$ [%]	EPC [$\frac{kWh}{Nm^3}$]
PEM	$Chamber_1$	-	95.47	-4.11	30.69	9.43
PEM	$Rake_1$	-	96.17	-4.09	31.07	9.31
PEM	$Rake_1$	IER	94.3	-3.88	32.12	9.01
GDE-flow-cell from Chapter 4.1 with planar anode						
PEM	$Chamber_1$	-	93.63	-4.69	26.36	10.98

Conclusion on the Impact of Flow-Fields

This chapter demonstrates the potential of improving the GDE-flow-cells performance by optimizing the feed gas distribution over the GDE area and the media flow in the catholyte chamber. It was demonstrated, that the increase of the GDE-gas contact area leads to an increase of the selectivity under diluted and reduced CO_2 supply, but it conditions a trade-off with the GDE-current collector contact area which, when increased, leads to a reduction of U_{Cell}. An optimization towards a more efficient version of this trade-off was demonstrated by an enhanced distribution of the feed gas over the GDE with an interdigitated path architecture, which forces the feed gas through the GDE creating large GDE-gas and GDE-current collector contact areas simultaneously. The optimized feed gas distribution additionally led to an increase of FE(CO) in experiments with reduced feed gas volume flow, where mass transport limitations are most severe. These characteristics influence the CO_2 consumption

of CO_2-to-CO electroyzers by generating high selectivity under reduced CO_2 supply and by keeping this high selectivity even under diluted supply. Regarding the modification of the catholyte chamber, the implementation of an ionically conductive spacer reduced the non-conductive areas which appeared in the form of gas bubbles. A more linear current flow through the catholyte chamber was created resulting in a more stable process. Aside from the enhanced process parameters, the combination of the modifications formed a cell architecture with mechanically stable support for the components, an even force distribution, and enabled ionic and electric contact through the entire active cell area. Thus, the modifications may form the basis for assembling a short-stack.

Information for Appendix

In Appendix A the preparation of the IER, the conductivity measurements with the IER, and the effect of the IER in the differential pressure in the catholyte chamber is described. The temperature development and the development of the pH value in the catholyte are presented.

4.3 Stacking of GDE-Flow-Cell

The modifications on the media flow compartments provided a GDE-flow-cell architecture with mechanical integrity and a secured electrical and ionic connection between the cell components. To investigate whether this formed cell architecture fulfills the prerequisites for stacking, the assembly and performance of a two-cell short-stack are presented and discussed.

Short-Stack Assembly

Two cells were connected in series via a bipolar plate to a two-cell short-stack (Figure 4.12). A titanium (grade 1) bipolar-plate connected the cathode of the terminal anode to the anode of the terminal cathode. The terminal anode (TA) is here defined as the cell that provides the global anode to the short-stack, while the terminal cathode (TC) provides the global cathode. The bipolar-plate provided a gas path architecture similar to Rake_1 to the cathode and an electrolyte path similar to Meander to the anode. The global cathode was assembled with Rake_1, the global anode was assembled similarly to the previous experiments, and the catholyte chambers were filled with the IER beads. The catholyte was introduced to the cell using two different pumps, each of them fed only one catholyte chamber with a volume flow of 50 ml/min. The CO_2 feed gas was supplied parallel to both cathodes sharing the same entrance and exit of the short-stack. The anolyte chambers were supplied parallel with anolyte over a shared entrance and exit with 100 ml/min.

Experiments were conducted in the test bench described in Chapter 3.5 at a constant current of 1A (100 mA/cm^2) and a $\lambda = 6.5$ to ensure a sufficient supply of CO_2 to both cathodes. The performance of the short-stack was evaluated by the selectivity and the stack voltage. The product gases from both gas chambers and both catholytes were analysed via the gas chromatograph and FE(CO) was determined. The voltage was measured between the anode of the first cell (Figure 4.12 (left)) and the

cathode of the second cell (Figure 4.12 (right)).

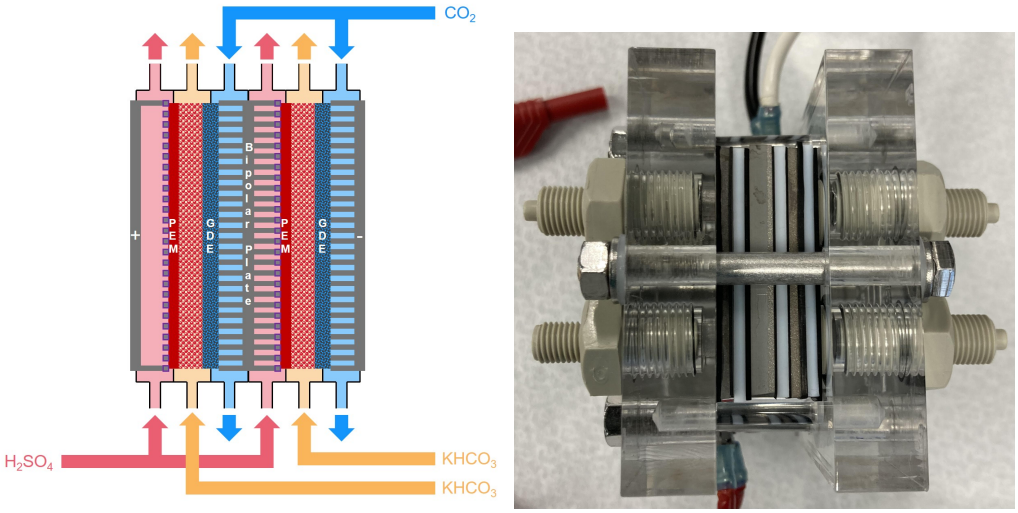

Figure 4.12: Illustration of the two-cell short-stack including the flow-sheet of electrolyte and feed gas (left) and image of the top view of the assembled stack (right). The two cells are connected via a bipolar-plate, which provides a gas path architecture similar to Rake_1 to the cathode of the TA (left) and a meander for the anolyte to the TC. The catholyte chambers were filled with the IER beads. The figure is adapted from [1].

Experiments with Short-Stack

In Figure 4.13 the obtained FE(CO) (left y-axis) and U_{Cell} (right y-axis) are depicted over time. Additionally U_{Cell} of two single-cells is illustrated in the figure at 7.8 V (2 x 3.9 V). The stack was operating for over 150 min at a minimum cell voltage of $U_{Cell} \leq 7.8V$. The determined FE(CO) increased over time to maximum values of $\geq 70\,\%$ after 100 minutes.

Based on the results obtained from experiments with the short-stack and in comparison to the performance of the individual single-cells, the stackability of the designed flow-cell can be deducted. By implementation of the mechanically stable flow-fields and spacer, force closure through the individual cells and hence through the short-stack could be provided. Thereby, an electric and ionic contact is given through the active stack area resulting in a stack voltage similar to the cell voltage of

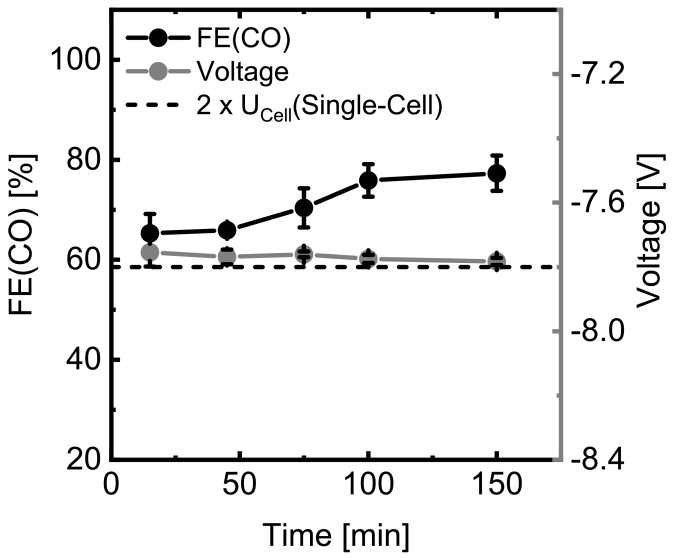

Figure 4.13: FE(CO) (left y-axis) and U_{Cell} (right y-axis) over time for experiment with stack at 100 mA/cm^2 and $\lambda = 6.5$ and U_{Cell} of two single cells at 7.8 V (2 x 3.9 V). The figure is adapted from [1].

two individual cells operating with Rake$_1$. However, the short-stack assembly requires optimization regarding the manifold of the media flows. For instance, the separation of the CO_2 supply into two individual feed gases could regain control over the pressure and volume flows in the gas chambers. Due to the limitation in the number of media flow entrances in the flow-cell, this separation was not possible and a sufficient and equal supply of CO_2 to the cathodes could not be ensured. The subsequent uneven distribution may cause FE(CO) to be lower with the short-stack, than with the single-cell (Figure 4.10), despite operating with a higher λ in the experiment with the short-stack.

An effect on the short-stack performance, that needs to be discussed is the possible formation of shunt currents. In general and in this work, cells in stacks are connected in series, and media is supplied in parallel.[108,111] This creates a conductive connection between electrodes, which do not serve the same cell. A consequence can be a parasitic current formation, the so-called shunt current, between these two electrodes, which reduces

the current density in the cells that are bypassed. Thus, the shunt current formation in the short-stacks can be displayed by a reduction in cell voltage of individual cells in the short-stack or by the reduction in the Faraday efficiency.[108,111] In the two-cell short-stack presented here, two separate catholyte circuits are used due to the given cell design. Thus, shunt-current formation in the anolyte is possible and needs to be discussed in detail.

Shunt Current Effects

For a detailed description of shunt current effects in short-stacks, circuit diagrams of three-cell short-stacks are illustrated in Figure 4.14.
The depicted short-stacks operate:
(a) with individual electrolyte circuits for each individual cell,
(b) with one joint anolyte circuit for all individual cells and no catholyte; or with one joint anolyte circuit for all individual cells and individual catholyte circuits for all individual cells,
(c) with one joint anolyte circuit for all individual cells and one joint catholyte circuit for all individual cells.

The anolyte circuit is illustrated in blue, and the catholyte circuit is in green. The diagrams in Figure 4.14(a)-(c) depict the measuring locations for the TA, MC, and TC voltages (U_{TA}, U_{MC}, U_{TC}), and provide the position of the membrane resistances (R_M) as well as the resistances of the anolyte and catholyte (R_C, R_A). The chemical reactions at the anode and cathode are illustrated as voltage sources. This representation was chosen instead of a (non-linear) resistor, to reflect the negligible change in electric potential observed in the experiment. Furthermore, for every circuit diagram, the absolute value of the current passing through the short-stack (I_{Cell}) is schematically illustrated over the length of the short-stack.

In scenario (a), the initial current (I_0) enters the short-stack at the cathode of the TC and flows through the short-stack to exit the short-stack at the anode of the TA. Hence I_{Cell} is similar to I_0 along the entire short-stack

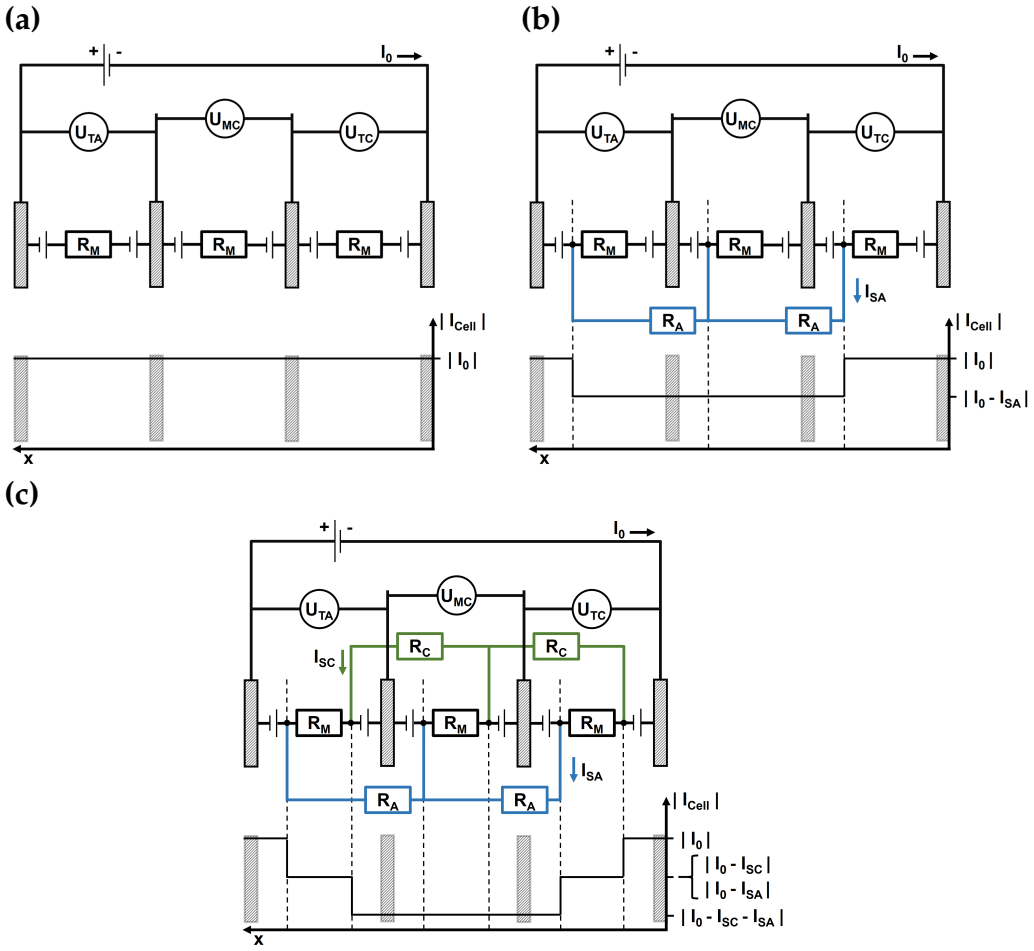

Figure 4.14: Circuit diagrams and graphs describing the behavior of the current (I_{Cell}) in three-cell short-stacks with (a) Separate electrolyte circuits for each individual cell in the short-stack to prevent shunt current formation, (b) A joint anolyte circuit for entire short-stack with ionically conductive anolyte and no catholyte (c) Two electrolyte circuits for ionically conductive anolyte and catholyte. (Membrane resistance: R_M ; Anolyte and catholyte resistance: R_A, R_C ; Voltages of individual cells: U_{TA}, U_{MC}, U_{TC}; Initial current: I_0; Shunt currents in anolyte and catholyte: I_{SA}, I_{SC}. The figure is adapted from [2].

length, leading to a constant current density in the short-stack. Therefore, in scenario (a), U_{TA}, U_{MC} and, U_{TC} are equal.

When operating with one anolyte circuit and an ionically conductive anolyte, I_{Cell} is divided to a certain extent at the entrance and exit of the

anolyte. The anolyte provides a bypass for the current, resulting in the parasitic shunt current formation I_{SA} at the anode of the TC. The shunt current follows the anolyte to reenter the short-stack at the anode of the TA. Corresponding to this scenario, I_{Cell} is lower than I_0 between the anode of the TC and the anode of the TA, and the lowest load occurs in the middle of the short-stack. Therefore, when shunt currents form in scenario (b), U_{TA} and U_{TC} possess a higher absolute value than U_{MC}.

In a short-stack operating with one anolyte and one catholyte circuit, both containing ionically conductive media, the formation of shunt currents can have an even higher impact. As illustrated in the circuit diagram in Figure 4.14(c) the catholyte provides an additional bypass to the one provided by the anolyte. At the entrance and exit of the catholyte I_{SC} forms from I_{Cell} and similar to scenario (b) I_{SA} forms in the anolyte. The impact on I_{Cell} can therefore be even greater than in scenario (b). Only at the anode of TA and at the cathode of the TC I_{Cell} is equal to I_0. The cell voltage behavior for scenarios (b) and (c) is the same with U_{MC} showing lower values than U_{TA} and U_{TC}.

These three scenarios represent different applications. Scenario (a) is an operation mode that can prevent the formation of shunt currents but is associated with a significant increase in effort to set up the periphery and has therefore not been applied in this work. Nevertheless, the behavior of I_{Cell} for scenario (a) represents the desired case for the presented two-cell short-stack. From scenario (b) one can derive a circuit diagram for a three-cell short-stack operating with MEAs, thus only anolytes are present. Scenario (c) can describe the shunt current formation in chlor-alkali electrolyzer stacks or the shunt current formation in CO_2 electrolyzer stacks with cell architectures operating with a catholyte and an anolyte, similar to the one presented in this study. However the presented stack operates with two individual catholyte circuits, hence the circuit diagram of scenario (b) represents the two-cell short-stack of this study.

Regarding the presented two-cell short-stack, the formation of shunt currents in the anolyte is possible. This implies, that the reduction of the

FE(CO) can originate from a reduced current density in the second cell of the stack as well as from the uneven distribution of CO_2 in the stack.

Conclusion on the Short-Stack with GDE-Flow-Cells

In the presented study, it is demonstrated, that the modifications on the media flow chambers in the GDE-flow-cell discussed in Chapter 4.2 provide a stackable flow-cell architecture. A two-cell short-stack was assembled and tested in experiments. While the general functionality is shown, limitations of the short-stack design become apparent. The experimental results showed the expected stack voltage of two times the single-cell voltage, however, lower FE(CO) were observed for the short-stack than for the equivalent single-cell. Possible shunt current formation, which is a stack-related effect, can have diminished the FE(CO) of the short-stack. An examination of these parasitic currents in the electrolyte is not possible in this setup, since the architecture of the bipolar-plate does not provide a component for voltage measurements of the individual cells.

Information for Appendix

A flowsheet describing the process design for experiments with the short-stack is illustrated. Appendix C provides an overview of the stack's and the single-cell's performances in terms of the performance indicators.

4.4 Modular Short-Stack Design for MEAs

In this chapter, a modular short-stack design with a consistent manifold concept is presented. The modular design addresses the limitations of the short-stack design presented in the previous chapter (Chapter 4.3).

The modular short-stack design is tested in a three-cell configuration, with flow-cells operating with MEAs. These cells facilitate the manifolding of media flows since only one aqueous electrolyte is present. Moreover, the MEAs have outperformed the GDE-flow-cells in previous experiments in terms of energy efficiency (Chapter 4.1 and 4.2). A study is performed concerning the performance of the short-stack in comparison to its equivalent single-cell. The experimental protocol for the experiments with the modular short-stack design is given in Chapter 3.5.

Assembly of the Modular Short-Stack

The investigated systems were assembled with in-house designed endplates and bipolar-plates, which are illustrated in Figure 4.24a. The media were delivered to the meander channels via media flow channels on the rear side of the components, to enable the stacking of the cells. Furthermore, the entrance and exit channels on the front side of the plates reduced the GDE-current collector contact area and caused leakage in previous experiments with the MEA (Chapter 4.1). A more detailed discussion on the effect of the entrance and exit channels can be found in Appendix C.

The bipolar-plate contained two of the plates illustrated in Figure 4.24(a) (right), giving the bipolar-plate a modular characteristic. Furthermore, the bipolar-plates possess a jetty to enable the voltage measurement of the individual cells in the short-stack. Thus, in addition to the performance of the full three-cell short-stack, the performance of the individual cells could be evaluated and compared to the performance of the respective single-cell. The plates were configured, to lead the media flow into the flow-fields from the rear side of the plates. This design increases

the contact surface of the GDE to the current collector and simultaneously facilitates the sealing of the cell.

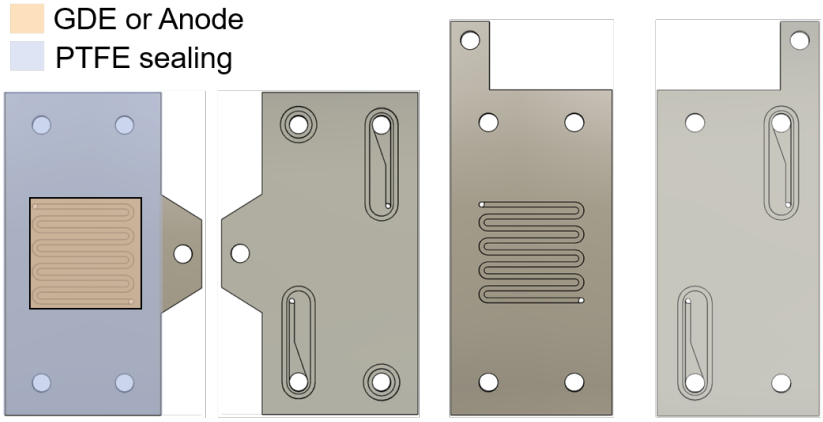

Figure 4.15: Illustration of the front and rear side of end-plates including the indicated position of the PTFE-sealing and the GDE (left); Illustration of the front and rear side of a modular bipolar-plate (right).[2]

The three-cell short-stack was assembled with two bipolar-plates and two end-plates. The cell providing the global anode to the short-stack was referred to as terminal anode (TA), the cell in the middle of the stack was defined as middle cell (MC), and the cell providing the global cathode was named terminal cathode (TC). In Figure 4.24(a) the assembled short-stack is illustrated in the test bench, and in Figure 4.24(b) an image of the short-stack is presented.

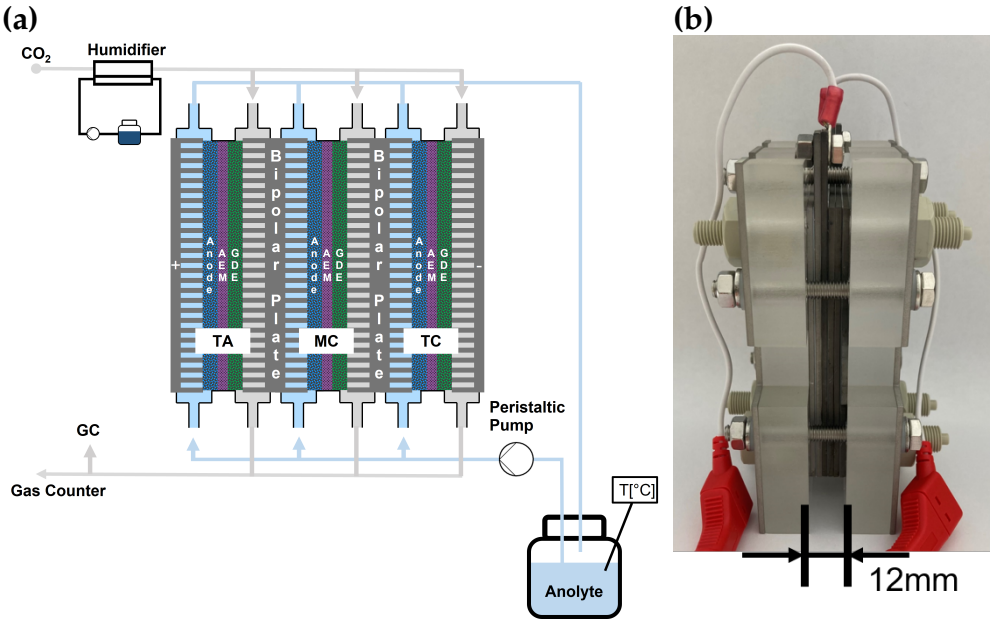

Figure 4.16: (a) Illustration of the short-stack in the test bench with the placement of the TA, MC, and TC, (c) Image of the three-cell short-stack indicating the thickness of three-cell short-stack (12 mm). The figure is adapted from [2].

Electrochemical Experiments

The results of the electrochemical experiments at 200 mA/cm^2 with the single-cell and the short-stack are illustrated in Figure 4.17. The voltages of the single-cell (Figure 4.17(a)), the short-stack (Figure 4.17(b)), and the individual cells in the short-stack (Figure 4.17(c)) are given over time. FE(CO) for the single-cell and the short-stack are shown in Figure 4.17a and 4.17b. To compare the voltages of the short-stack and the single-cell, ΔVoltage is illustrated in Figure 4.17d over time.

The obtained results demonstrate a stable process of the single cell and the short stack at 200 mA/cm2 for 300 min. In both experiments, FE(CO) was maintained over 90 %. It must be emphasized, that no other product than CO and H_2 was observed in relevant amounts. The results of ^1H NMR analysis measurement of an anolyte sample are provided in the Appendix B.

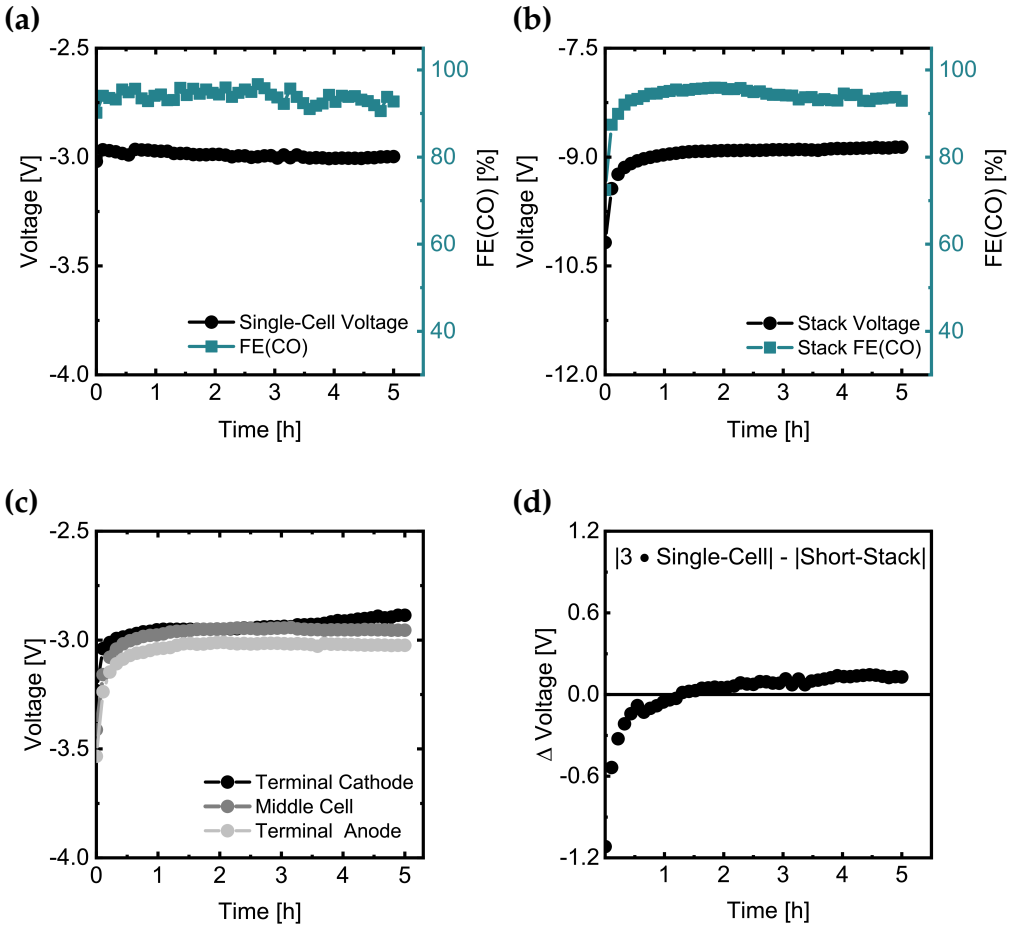

Figure 4.17: Over time at 200 mA/cm²: Cell voltage and FE(CO) for (a) single-cell, and (b) short-stack, (c) Cell voltages of individual cells in short-stack, and (d) differential voltage between the absolute value of three times single-cell voltage minus short-stack voltage. The figure is adapted from [2].

For the single-cell, a cell voltage of 3 V, and for the short-stack, a stack voltage of 9 V was observed. The voltage measurements of the individual cells showed values similar to the ones determined for the single-cell (3 V). It is noteworthy that a difference between the individual cells was observed. The TA operated at cell voltages higher than those of the middle cell (MC), and the voltage of the TC was observed to be the lowest of all three individual cells.

The short-stack voltage is the sum of the individual cell voltages,

and since these are similar to the single-cell voltage, ΔVoltage is close to zero (Figure 4.17(d)). Two hours after the start of the experiment, ΔVoltage shifts from a negative to a positive value and remains positive for the rest of the experiment. This behavior of ΔVoltage indicates that the individual cells in the short-stack operate on average, after an initial phase, at lower cell voltages than those of the single-cell. Regarding these results, the designed short-stack resembles the single-cell performance at 200 mA/cm².

The determined cell voltages as well as the FE(CO) for the discussed current density are consistent with values given in the literature for MEAs operating with the same material. Accordingly, the electrical energy input efficiency for the single cell ($\epsilon_{(CO)}$ = 41.25 %) and the short stack ($\epsilon_{(CO)}$) = 41.38 %) is in alignment with the literature. Thus, the performance of this stack is approaching the theoretical maximum of $\epsilon_{(CO)}$ = 62 % for alkaline CO2-to-CO reduction coupled with the OER as recently discussed by Reichbauer et al..[34] $\epsilon_{(CO)}$) obtained for all single-cells and short-stacks can be found in the Appendix C.

The results obtained at current densities from 100 to 400 mA/cm² for the single-cell and short-stack ion are illustrated in Figure 4.18. In Figure 4.18(a), the FE(Total) describing the sum of the FE(CO) and the FE(H_2) is provided for the single-cell and the short-stack. In Figure 4.18(b), the FE(CO) for the single-cell and the short-stack is shown. Figure 4.18(c) illustrates the stack voltage and the value of three times single-cell voltage, and in Figure 4.18(d) the single-cell voltage and the voltage of the individual cells are depicted.

For the short-stack FE(Total) of 97 % at 100 mA/cm², 98 % at 200 mA/cm², 95 % at 300 mA/cm², and 94 % at 400 mA/cm² are obtained. In experiments with the single-cell total Faraday efficiencies of 97 % at 100 mA/cm², 95 % at 200 mA/cm², 97 % at 300 mA/cm², and 96 % at 400 mA/cm² are observed. Under consideration of the standard deviations (±4 %) the FE(Total) are close to 100 % at all applied current densities for both systems. Other products such as formate can form at the Ag

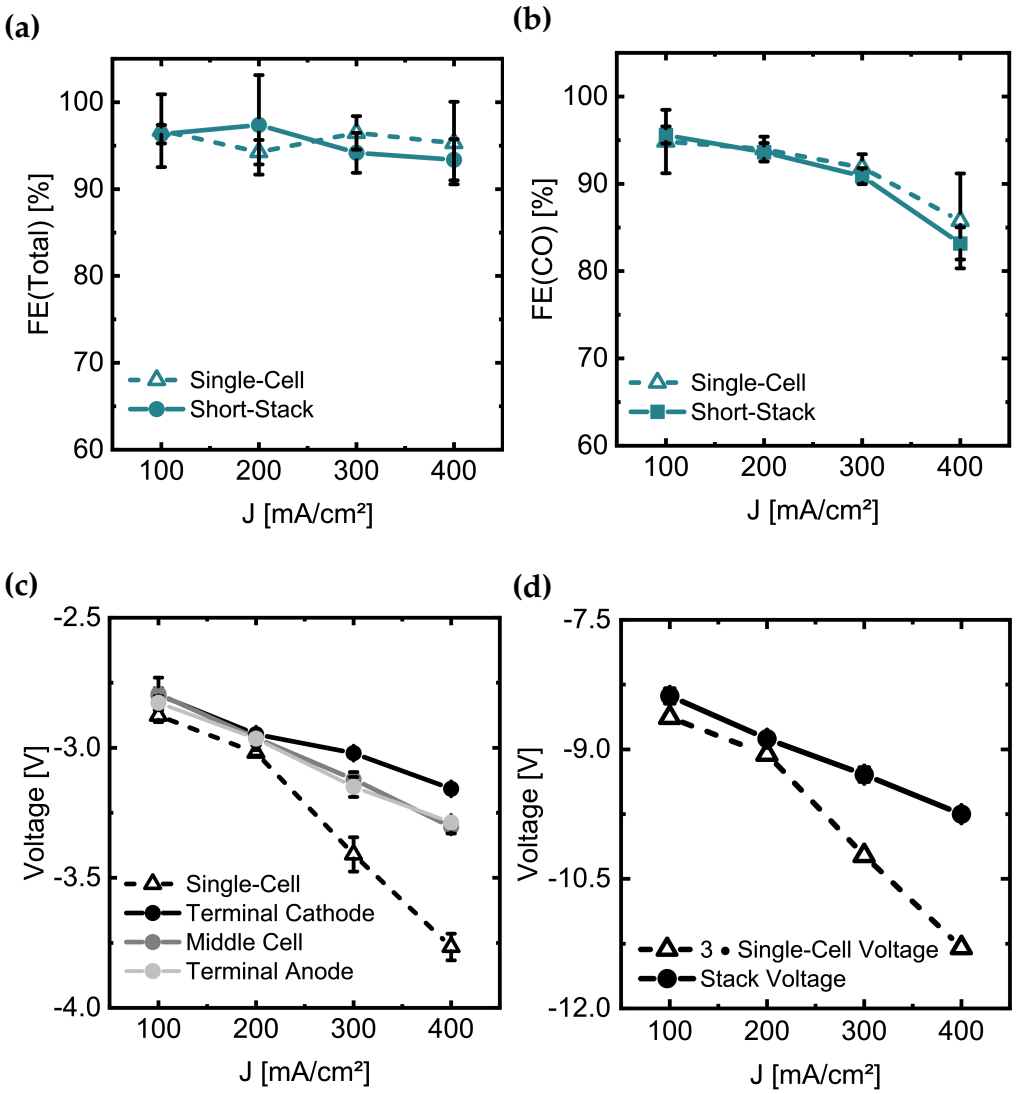

Figure 4.18: Over different current densities: (a) FE(CO) of single-cell and short-stack, (b) Stack voltage and three times single-cell voltage, and (c) Voltages of single-cell and individual cells in short-stack. The figure is adapted from [2].

catalyst GDE, however, formate is likely to be transported via the AEM to the anode side, to be oxidized to CO_2. Traces of products in relevant quantities other than H_2 and CO are therefore not expected.

For both systems, an increasing voltage and a decreasing FE(CO) can be observed with increasing current density due to the increasing cur-

rent load passing the systems. From 200 to 400 mA/cm² the curves are linear, indicating that the ohmic resistance of the cell dominates the cell voltage in this regime. While FE(CO) for the single-cell and the short-stack show similar behavior by decreasing from 95 % (100 mA/cm²) to 85 % (400 mA/cm²), the voltages differ in behavior. The voltage of the single-cell increases from 2.85 V at 100 mA/cm² to 3.6 V at 400 mA/cm². For the individual cells of the short-stack, a similar cell voltage of 2.82 V at 100 mA/cm² was observed, however higher cell voltages compared to the single-cell were observed at higher current densities. For instance at 400 mA/cm² cell voltages of 3.3 V, 3.3 V, and 3.2 V were determined for the TA, the MC, and the TC, respectively. Hence, the performance of the individual cells in the short-stack differs from the performance of the single-cell at higher current densities. It is noteworthy, that at all current densities, the lowest cell voltage was consistently observed for the TC.

Considering the stack voltages, the results obtained indicate a performance-increasing effect of the short-stack. In contrast to the free-standing single-cell, the cells in the short-stack touch each other with most of their surface area. Since each cell generates heat, different behavior of the temperature development in these two systems can be anticipated. Thus, temperature effects within the short-stack need to be investigated.

Temperature Effects

The ion conductivity of AEMs is temperature dependent and typically lower for HCO_3^- and CO_3^{2-} ions than for OH^- ions.[69,73,84,97,112,120,121] For instance the ionic conductivity of the Sustainion® membrane, increases from 24 mS/cm at 25 °C to 66 mS/cm at 80 °C when operating with 1 M $KHCO_3$.[73,112] As the ionic conductivity of the membrane increases at elevated temperatures, it is reasonable to assume, that temperature effects lead to an increase of the individual cell performances.

Illustrated in Figure 4.19 are the temperatures measured in the electrolytes for the single-cell and the short-stack. In Figure 4.19(a) the tem-

peratures measured in experiments at 200 mA/cm^2 are illustrated over time. The electrolyte temperatures increase at the beginning of the experiment from 25 °C and reach a steady state after one hour. In experiments with the single-cell the electrolyte reaches a temperature of 30 °C, with the short-stack a temperature of 33 °C was measured toward the end of the experiment. Figure 4.19(b) depicts the temperatures determined in experiments at different current densities. The electrolyte temperatures increase with increasing current densities and reach values of 38 °C (single-cell) and 43 °C (short-stack) at 400 mA/cm^2.

The plateau formation of the electrolyte temperatures over time at 200 mA/cm^2 indicates, that an equilibrium between the heat dissipation of the systems and the production of heat from ohmic losses and the reaction of OH^- with excess CO_2 is reached. In terms of the difference in steady-state temperatures for the single-cell and the short-stack, the periphery of the systems needs to be considered. For the single-cell a smaller electrolyte vessel is used compared to the short-stack. On one hand, the larger electrolyte vessel provides a larger surface area for cooling. On the other hand, a longer retention time of the electrolyte in the vessel can be calculated via the electrolyte volume flows for the single-cell (5 min single-cell; 3.5 min short-stack). Regarding the applied electrolyte flow rates, a similar volume flow is anticipated for the individual cells and the single-cell, enabling similar cooling of each cell. The discussed factors can have an impact on the temperature development in the different systems, however, it is plausible that the ratio of the active surface area to the exterior surface area, which is exposed to the air, has a more significant influence. In the short-stack, the active surface area triples compared to the single-cell, while the exterior surface area remains practically identical. Thus, a significantly increased amount of heat occurs at the same exterior surface area. The increase of the area ratio, therefore leads to a higher steady-state temperature in the short-stack.

The elevated temperatures increase the ionic conductivity of the Sustainion® membrane and thereby decrease the ionic resistance in the

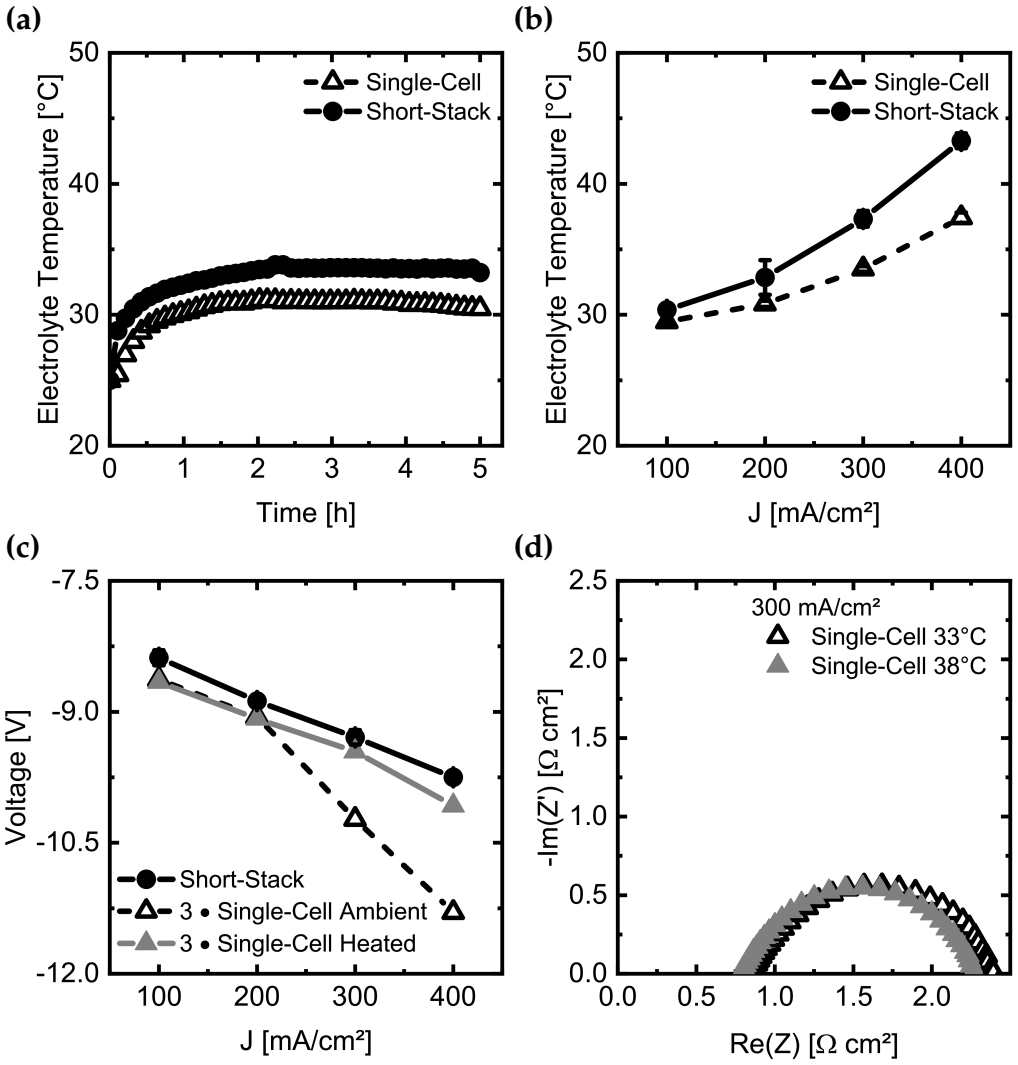

Figure 4.19: (a) Electrolyte temperature in experiments with single-cell and short-stack at 200 mA/cm^2 over time, (b) electrolyte temperature in experiment with single-cell and short-stack over different current densities, (c) single-cell voltage determined in experiments with heated electrolyte (30 °C at 100 mA/cm²; 33 °C at 200 mA/cm²; 38 °C at 300 mA/cm²; 43 °C at 400 mA/cm) versus single-cell voltage determined at ambient conditions and stack voltage over applied current densities, (d) Nyquist Plots for the single-cell obtained at 300 mA/cm² with a 300 mA excitation amplitude, in experiment at ambient conditions (33 °C) and in experiment with heated electrolyte (38 °C). The figure is adapted from [2].

individual cells. As the electrolyte temperature increase in the short-stack is more pronounced with increasing current density, the voltages of the individual cells are lower at higher current densities compared to the voltage of the single-cell.

To verify this hypothesis, an experiment at the different current densities was performed with the single-cell, where the electrolyte was heated to the electrolyte temperatures determined in experiments with the short-stack at the specific current density. The electrolyte was heated to 30 °C at 100 mA/cm², to 33 °C at 200 mA/cm², to 38 °C at 300 mA/cm², and to 43 °C at 400 mA/cm². In Figure 4.19(c) three times the cell voltage of the single-cell obtained at ambient conditions and with the heated electrolyte, as well as the short-stack voltage are presented over the different current densities.

Similar to the previous experiments at different current densities, the cell voltage increases with increasing current densities. The voltage increases from 2.85 V at 100 mA/cm^2 to 3.35 V at 400 mA/cm^2 (Figure 4.19(c)). While the voltages obtained in the experiments with the single-cell are similar at 100 mA/cm² and at 200 mA/cm², lower voltages are observed at higher current densities for the single-cell operated with the heated electrolyte. As illustrated in Figure 4.19(c) the multiplied voltages of the single-cell almost replicate the voltages obtained with the short-stack. Thus, the single-cell with the heated electrolyte operates at similar voltages to the average voltage of the individual cells in the short-stack. For a more detailed description of the temperature effects on the cell, the Nyquist plots obtained for 33 °C and 38 °C at 300 mA/cm² with an excitation amplitude of 300 mA are presented in Figure 4.19(d). In the Nyquist plots, a shift of the high-frequency resistance, from 0.86 Ω·cm² to 0.79 Ω·cm² can be observed. Since the high-frequency resistance can be attributed to the membrane resistance[122,123], a reduction of cell voltage with increasing temperature can be traced to membrane conductivity. In Figure 4.19(d) a shift of the low-frequency resistance from 1.52 Ω·cm² to 1.48 Ω·cm² can be observed with increasing temperature, which is at-

tributed to the charge transfer reactions.[122,123]. The Nyquist plots for the other current densities applied to the single-cell, as well as the Nyquist plots obtained for the short-stack are presented in the Appendix B.

Overall, the results obtained with the heated electrolyte demonstrate, that the reduced voltages in the short-stack at higher current densities originate from higher temperatures in the short-stack, influencing the membrane conductivity as well as the charge transfer.

Effect of Temperature Gradients

Furthermore, these results allow the conclusion that the heat distribution in the short-stack generates the reduction of cell voltage in the TC. The anticipated heat distribution of the short-stack is the accumulation of heat in the middle of the short-stack. Following this hypothesis, the highest temperatures and lowest cell voltages were to be determined for the MC and not, as observed in this work, for the TC. The cells making up the short-stack are asymmetrical, having a liquid and a gas side when compared to e.g. PEM-electrolysis cells where a liquid medium flows through both sides. If one ignores the minimal cooling effects by the gas, the cooling of the short-stack only occurs via the electrolyte, and the highest temperatures in the cells of the short-stack appear toward the cathode side of the MEA. While the TA and the MC are cooled by their anolytes and by the respective anolytes of their adjacent cells, the TC is only cooled by its anolyte and is, therefore, the only cell with liquid cooling from only one side. Hence, higher temperatures can be expected to appear in the TC resulting in the observed lower cell voltages. The performance of the individual cells is therefore influenced by their location in the short-stack.

To verify the hypothesis that the lower voltages determined for the TC arise from the asymmetrical heat distribution in the short-stack, an experiment with a modified short-stack is performed. The modularity of the bipolar plates enables the attachment of a half-bipolar plate on the TC (Figure 4.20. This additional compartment is a media flow chamber for

the electrolyte to cool the TC.

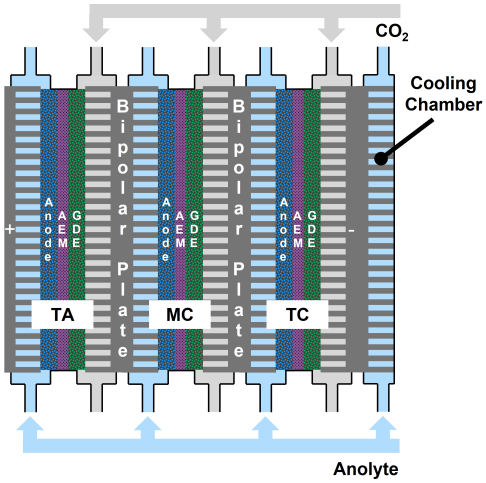

Figure 4.20: Modified short-stack with a half-plate of the bipolar plate on the adjacent side of the TC. The figure is adapted from [2].

An experiment is performed at the current densities 100, 200, 300, and 400 mA/cm². Figure 4.21(a) depicts the voltages of the short-stack and the modified short-stack over the current densities. The voltages for the short-stacks behave similarly with increasing current density, however at lower current densities (100-200 mA/cm²) higher voltages can be observed for the modified short-stack. In Figure 4.21(b) the obtained cell voltages of the individual cells in the short-stack, and the single-cell voltage of the previous experiment are illustrated over the different current densities.

As in previous experiments, the individual cell voltages are similar to the single-cell voltage at current densities of 100 and 200 mA/cm² (2.85 V at 100 mA/cm², 3 V at 200 mA/cm²). At higher current densities lower cell voltages are determined for the individual cells compared to the single-cell. The cell voltages of the individual cells are similar at 300 mA/cm² (3.15 V), but diverge at 400 mA/cm². While for the TA a cell voltage of 3.31 V is determined at 400 mA/cm², for the TC and the MC lower cell voltages with 3.25 V and 3.2 V are observed.

Regarding the voltages of the short-stacks, the additional cooling in

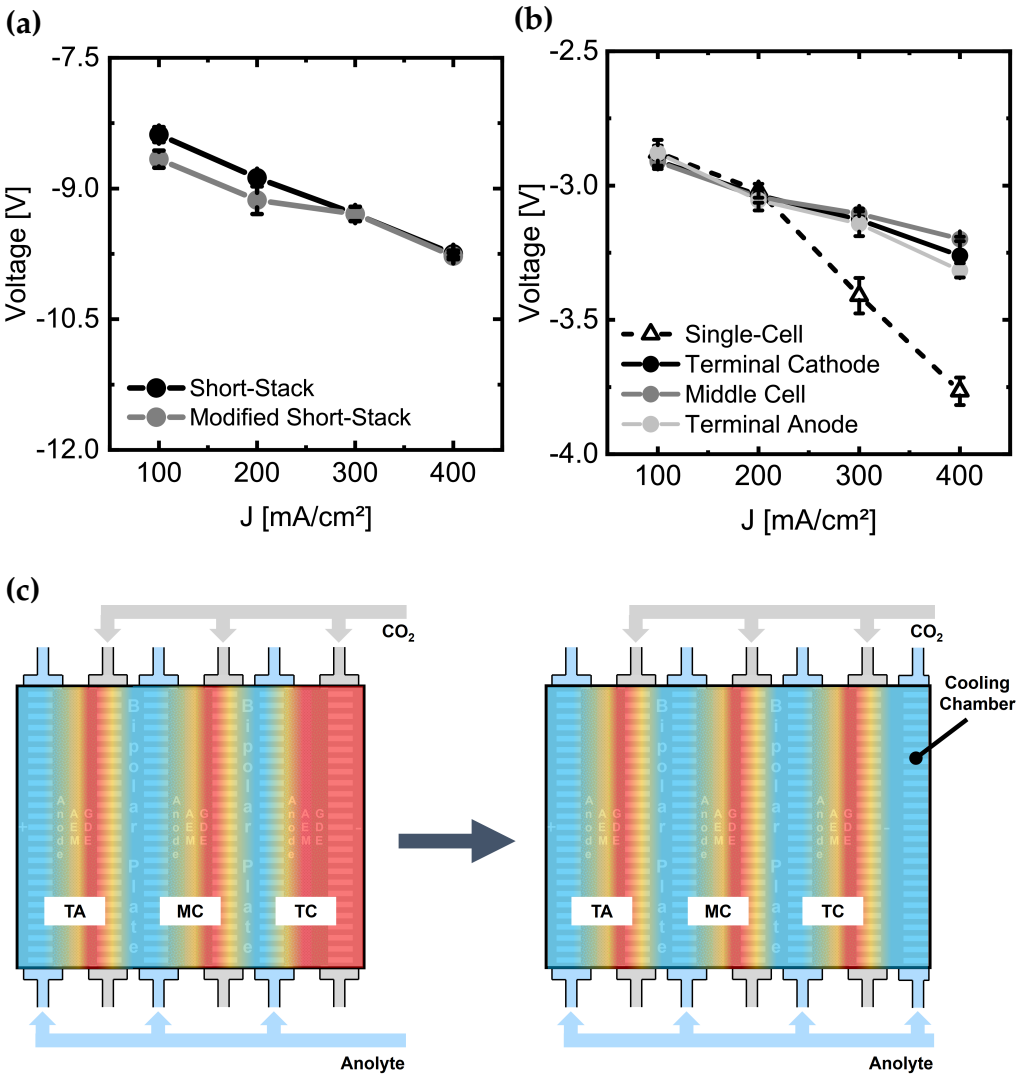

Figure 4.21: (a) Voltages obtained with modified short-stack and short-stack, (b) Cell voltages of individual cells in the modified short-stack over different current densities, (c) Possible heat distribution in short-stack (left) and in modified short-stack (right) with neglected cooling by gas. Temperatures that are higher than the electrolyte temperature are colored in red and the electrolyte temperature is colored in blue. The figure is adapted from [2].

the modified short-stack can mitigate the temperature development in the short-stack, which leads to the increase in voltage observed in Figure 4.21(a). In terms of the individual cells, between 100-300 mA/cm^2

the voltage of the modified short-stack is more evenly distributed on the individual cells compared to the short-stack without the additional cooling (Figure 4.18(b)). The additional chamber enables a heat removal at the TC similar to the other individual cells and thereby generates a more symmetrical heat distribution in the short-stack. In Figure 4.21(c), the anticipated heat distributions in the short-stack and the modified short-stack are illustrated. Colored in red are temperatures higher than the electrolyte temperature, colored in blue. While the asymmetrical heat distribution in the short-stack can reduce the cell voltage of the TC, thereby enhancing its performance, we emphasize, that an asymmetrical heat distribution within the short-stack can lead to different degradation processes in the individual cells. Considering this, the asymmetrical heat distribution is not beneficial, specifically in terms of a possible long-term operation. However, this degradation behavior would be highly dependent on the specific materials used in the electrodes and membranes and thus not explored in this study.

Due to symmetrical heat distribution, the individual cells operate at similar temperatures in the modified short stack, hence, similar cell voltages are obtained between 100 and 300 mA/cm^2. It is noteworthy that at 400 mA/cm^2, the individual cell voltages diverge within the standard deviations ($\pm$ 0.3 V). However, it is plausible that shunt currents form in the short stack, which can lead to an uneven voltage distribution within the short stack. As temperature effects in the modified short stack no longer dominate the voltage distribution in the short stack, the observation of shunt currents at higher current densities is possible and needs, therefore, to be investigated.

Quantification of Shunt Currents

In this work, the short-stack operates with a combined anolyte circuit. The media flow channels connecting the cathodes in parallel are filled with a non-conductive medium (CO_2 gas). Thus, the shunt currents can only form in the anolyte circuit.

In Figure 4.22, I_{Cell} and I_{SA} flowing through the short-stack and the anolyte are depicted. Displayed is the bottom half of the short-stack as the bubble formation (O_2/CO_2) appearing at the anode prevents the formation of shunt currents toward the exit of the anolyte.

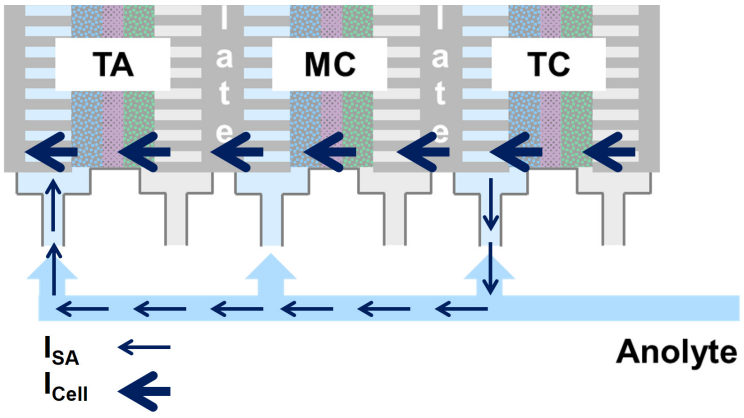

Figure 4.22: Illustration of shunt current formation in the anolyte for investigated short-stack. The figure is adapted from [2].

The individual cell voltages observed in the experiments with the modified short-stack at 400 mA/cm² (Figure 4.21(b)) display a possible voltage distribution expected for scenario (b) (Figure 4.14(b)), that has already been discussed in chapter 4.3. Here, at 400 mA/cm² a lower cell voltage is observed for the MC compared to the TA and TC.

To investigate and quantify the formation of shunt currents in the short-stack, the MEAs in the short-stack are replaced with PTFE sheets, which are electrically and ionically insulating. The plates are therefore only connected via the ionically conductive anolyte (10 mM $KHCO_3$) which was circulated with 150 ml/min through the cell. A UI curve was plotted by performing cyclic voltammetry between 0 V and 10 V to cover the entire range of voltages determined in experiments with the short-stack. As shunt currents are only expected in the anolyte, the voltage was applied between the anode plate of the TC and the anode plate of the TA. With a scan rate of 200 mV/s, ten scans were performed and plot-

ted to a UI curve. The experiment was performed at 30, 37.5, and 45 °C as the short-stack operates at different temperatures. The same experiments were performed with 100 mM $KHCO_3$ at 30, 37.5, and 45 °C and with 1 M KOH at 45 °C to investigate the shunt current formation when operating with more conductive electrolytes.

The UI curves determined from the experiments are illustrated in Figure 4.23.

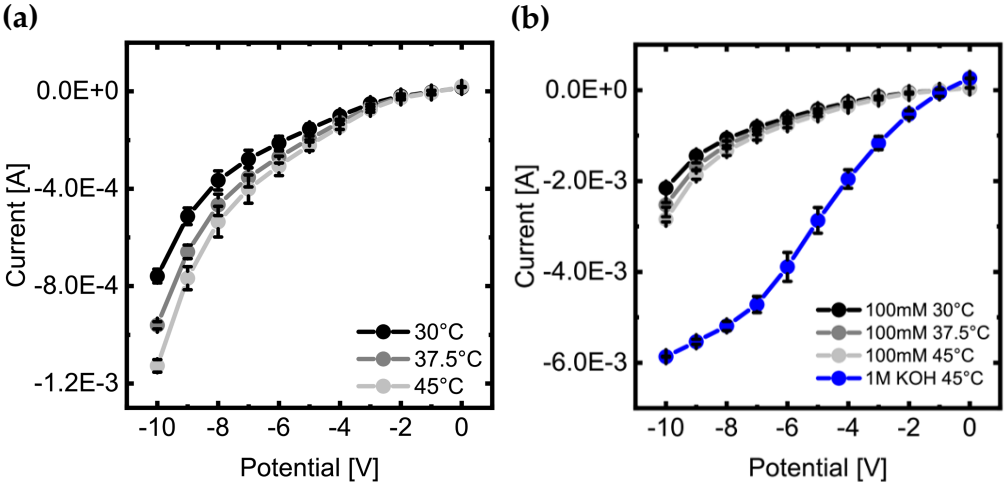

Figure 4.23: (a) UI curves at different temperatures for experiment with short-stack containing PTFE sheets instead of MEAs, operating with 10 mM $KHCO_3$. (b) UI curves at different temperatures for experiments with short-stack containing PTFE sheets instead of MEAs, operating with 100 mM $KHCO_3$ and 1 M KOH. The figure is adapted from [2].

In experiments with the 10 mM $KHCO_3$ solution, the current increased with increasing temperature and increasing potential. The increase of current with increasing temperature is related to the increasing ionic conductivity of the anolyte with increasing temperature. In experiments with the short-stack, the voltage between the anode of the TC and the anode of the TA was determined to increase from 5.64 V at 100 mA/cm² to 6.6 V at 400 mA/cm². For these voltages, currents of 0.3 mA and 0.4 mA were observed at 45 °C. Hence, the experiments validate, that shunt currents appear in the short-stack. However, considering the ratio of the determined shunt current and the applied currents in ex-

periments with the short-stacks, the shunt current formation is negligible.

In experiments with the electrolytes providing higher ionic conductivity, the current increases with increasing potential and increasing temperature. At 5.6 V and 6.6 V, currents of 0.75 mA and 1 mA were observed in experiments with 100 mM $KHCO_3$ at 45 °C. Currents of 4 mA and 3.5 mA were determined in the experiment with 1 M KOH at 45 °C at the same voltages.

Derived from the results, the shunt current formation intensifies with increasing ionic conductivity of the anolyte. In terms of the applied currents in the short-stack experiments, the shunt currents observed in the experiments are comparatively low, even with the increased ionic conductivity of the anolyte. However, the formation of shunt currents is not completely suppressed, hence the effects of shunt currents on degradation mechanisms and the stack performances need to be considered in scaled systems.

Conclusion on the Modular Short-Stack Design

In this study, the design of a three-cell short-stack for the CO_2-to-CO electrolysis operating with MEA cells is reported. Its performance is compared to the equivalent single-cell. The short-stack was assembled with modular bipolar-plates, allowing the measurement of the individual cell voltages within the short-stack, thereby enabling the comparison of the individual cells' performances to the single-cell performance.

A difference between the performance of the individual cells and the single-cell is observed and the underlying effects are elucidated. While the FE(CO) of the short-stack and the single-cell are similar, the cell voltages for the individual cells are lower than for the single-cells. It was demonstrated, that elevated temperatures occurring in the short-stack enhanced the ionic conductivity of the membrane, and led to decreasing individual cell voltages compared to the single-cell. This effect is more pronounced with increasing current densities.

It is noteworthy, that the measurement of the individual cell voltages

revealed the correlation between each cell's performance and its position in the short-stack. By taking advantage of the flexibility of the short-stack design, the cell voltage reduction of the TC could be traced to uneven heat distribution within the short-stack.

Information for Appendix:

Appendix C provides an overview of the stack's and the single-cell's performances in terms of the performance indicators. In Appendix B, results of the ^{1}H NMR measurement of the anolyte and the results of the impedance measurements with the single-cell and the short-stack are provided.

4.5 Extending the Role of End- and Bipolar-Plates

The functions of end-plates and bipolar-plates are oftentimes reduced to manage the distribution of media flow on catalyst surfaces and to provide electrical connection and mechanical support to the other components. However, these backing-plates offer a surface area, which can potentially participate in the electro-catalytic conversion process. By implementing catalytically active backing-plates, the area of the catalytic active surface can be increased leading to a reduction of cell voltage, and hence to a reduction of the short-stack voltage. Further, such catalytically active coating might prevent oxidation of the surface and thus improve electrical conductivity. The modular short-stack provides the opportunity to swap end-plates as well as to modify the bipolar-plates by exchanging half-plates. Taking advantage of this opportunity, end-plates and bipolar half-plates were coated with Ir-MMO by ©Metakem with a loading of approximately 1 mg/cm² and were implemented into the short-stack. The bipolar-plates were assembled with a plain-Ti half-plate with an Ir-MMO coated half-plate. Experiments were performed similarly to the experimental protocol presented in Chapter 3.5. The performance of the modified short-stack is compared to the short-stack containing plain-Ti plates only and to its equivalent single-cell.

Short-Stack Assembly with Coated Plates

As illustrated in Figure 4.24(a), the two-material bipolar-plates and a coated end-plate were implemented with the Ir-MMO side facing the anode side of the individual cells. The function of the components was thus extended to increase the catalyst´s surface area and to participate in the OER reaction at the anode. In Figure 4.24(b) an image of the short stack containing three cells and the Ir-MMO coated plates is presented.

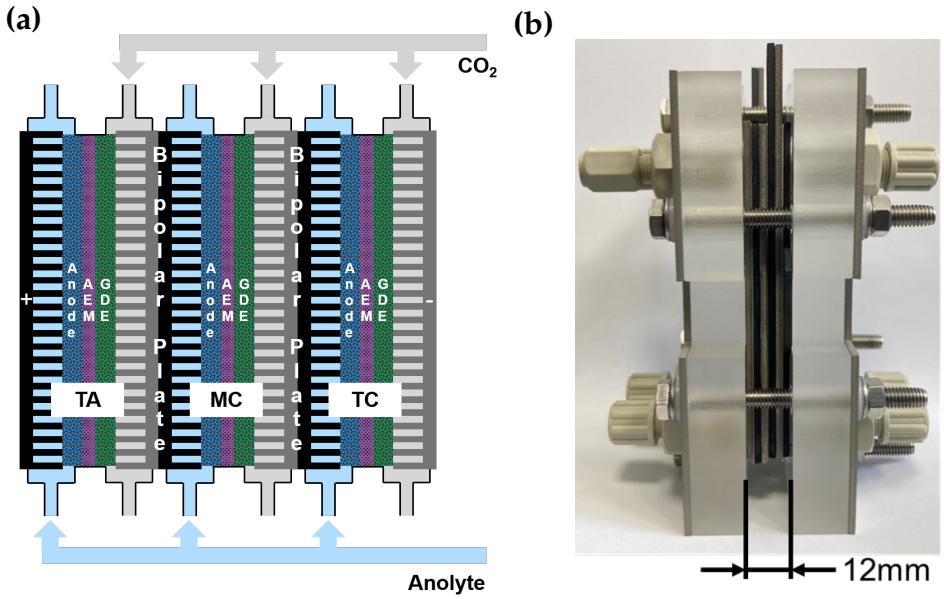

Figure 4.24: (a) Illustration of three-cell short-stack with Ir-MMO coated plates at the anode side of each cell; Illustration of the position of the individual cells: TA, MC, and TC, (b) Image of the three-cell short-stack with Ir-MMO coated plates.

Impact in Short-Stack

The results of the electrochemical experiments with the short-stack containing the Ir-MMO plates at 200 mA/cm² are presented in Figure 4.25, together with the results obtained with the plain-Ti short-stack. The FE(CO) evaluated from the experiments is illustrated in figure 4.25(a), the stack voltage in figure 4.25(b), and the voltage of the individual cells in figure 4.25(c).

After an initial phase, FE(CO) remains $\geq 90\,\%$ for the entire time of the experiment for both short-stacks. For the Ir-MMO short stack, FE(CO) increases from 89 % at the beginning of the to 94 % at the end of the experiment. For the plain-Ti short-stack, FE(CO) increases more rapidly at the beginning to 95 % but aligns with the values of the short-stack with the Ir-MMO plates toward the end of the experiment. The short-stack with the Ir-MMO plates operates, similar to the plain-Ti short-stack, at a stack voltage of 9 V. For the individual cells in the short-stacks, cell volt-

ages of about 3 V were determined, while the lowest cell voltages were consistently observed for the TC.

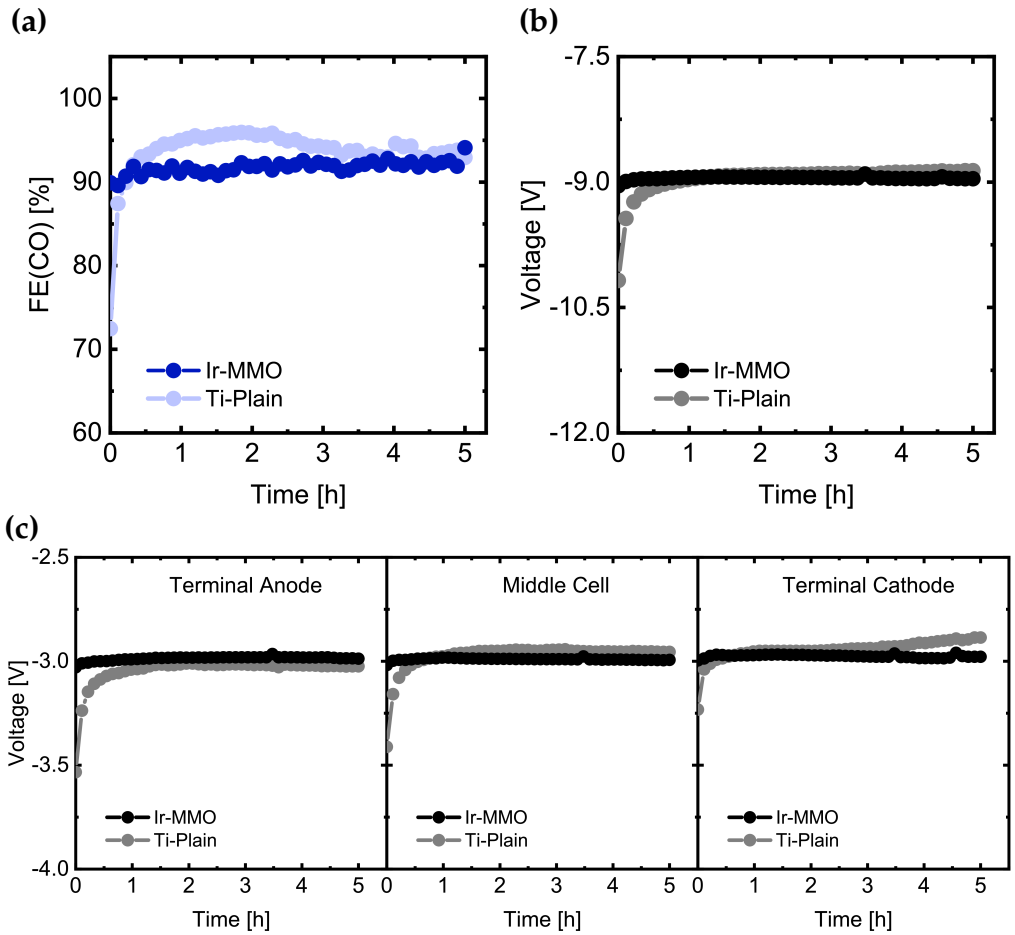

Figure 4.25: Results of experiments with short-stacks at 200 mA/cm² over time: (a) FE(CO) of short-stack with Ir-MMO coated plates and of short-stack with plain-Ti plates, (b) Stack voltage of short-stack with Ir-MMO coated plates and of short-stack with plain-Ti plates, and (c) Voltages of individual cells in short-stack with Ir-MMO coated plates and in short-stack with plain-Ti plates.

The performance indicators in Figure 4.25 show linear trends over the time of the experiment, displaying a stable process for the short-stack with the catalyst-coated plates. Comparing the overall performance of the plain-Ti short-stack and the short-stack with the Ir-MMO plates, similar trends and values of the performance indicators can be observed. The

results demonstrate that the two-material bipolar-plates do not diminish the short-stack performance. On the other hand, the increase in the catalyst surface area does not lead to a visible enhancement of the performance. It is plausible, that stacking-related effects such as the formation of shunt currents and temperature gradients may suppress the visibility of a performance-enhancing effect by the catalyst surface increase. To demonstrate, that the effect is not absent due to the stacking of the flow-cell, the same experiments are performed with a single-cell containing an Ir-MMO coated end-plate at the anode side.

Impact in Single-Cell

In Figure 4.26(a,b) the results of the electrochemical experiments with the single-cells at 200 mA/cm^2 are illustrated over time. In Figure 4.26(a) the FE(CO), and in Figure 4.26(b) the cell voltages of the single-cells are presented.

Constant FE(CO) $\geq$ 90 % were determined for the Ir-MMO and the plain-Ti single-cell. For the single-cell with the catalyst-coated end plate, a constant cell voltage of 3.05 V was observed, while the single-cell with the plain-Ti plates operated at 3.01 V. To enable the comparison of the single-cell performances to the short-stack performances, ΔVoltage is calculated with the absolute values of three times the single-cell voltage minus the short-stack voltage are illustrated in figure 4.26(c) over time. ΔVoltage for the short-stack and the single-cell with the Ir-MMO coated plates was according to the calculation at a value of 0.3 V. For the systems with the plain-Ti plates, ΔVoltage increased from a negative to a positive value to reach a steady state at 0.14 V, as found previously. For both short stacks, a positive ΔVoltage is determined, which indicates, that the individual cells in the short stack operate on average at lower cell voltages than the equivalent single-cells.

The obtained results of the single-cell with the catalyst coated flow-field indicate a stable process over five hours. In comparison to the single-cell with the plain-Ti plates, the single-cell with the Ir-MMO

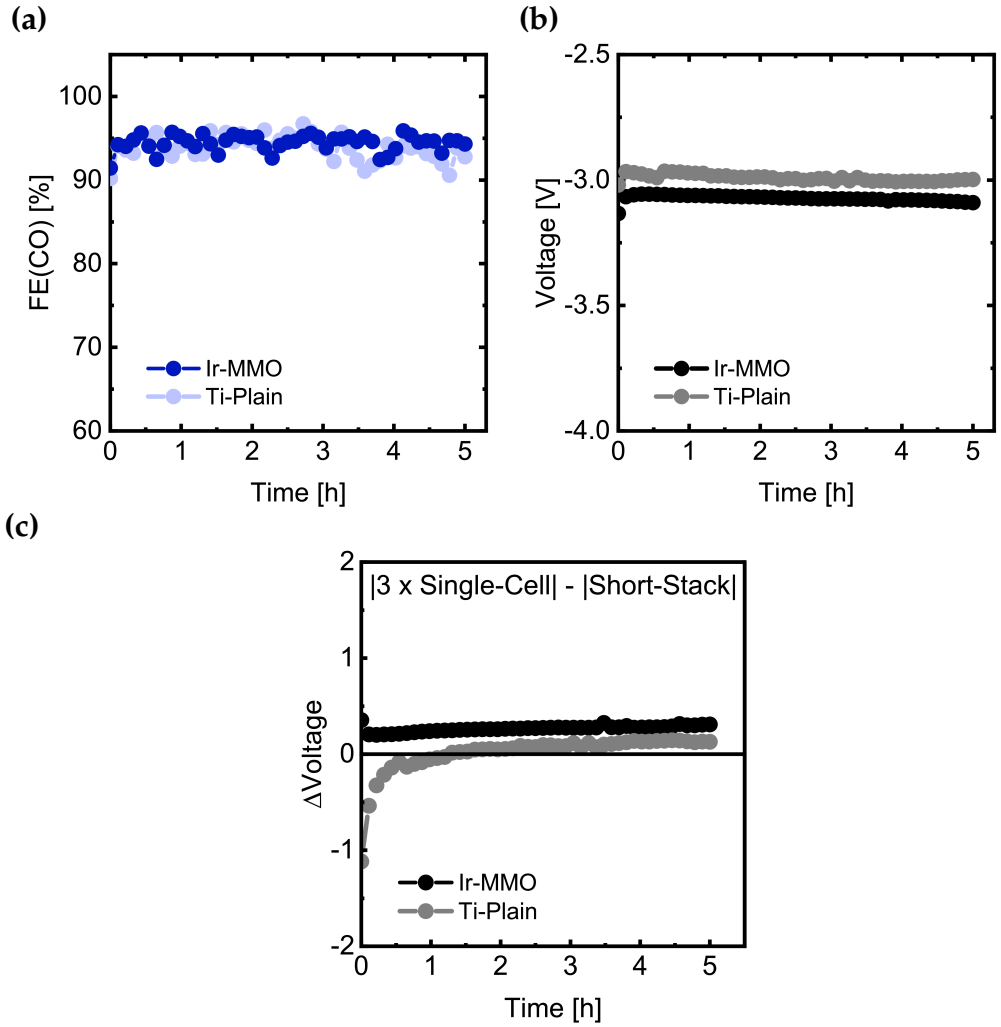

Figure 4.26: Results of experiments with single-cells at 200 mA/cm² over time: (a) FE(CO) of single-cell with Ir-MMO coated End-Plate and of single-cell with plain-Ti plates, (b) Stack voltage of single-cell with Ir-MMO coated End-Plate and of single-cell with plain-Ti plates, and (c) differential voltage (ΔVoltage) between the absolute value of three times single-cell voltage minus short-stack voltage.

coated flow-field operates at marginal higher cell voltages, however similar FE(CO) were obtained. Higher cell voltages for the single-cell with the catalyst-coated coated flow-field are therefore not resulting from an insufficient suppression of the HER. Possible is a reduced electric conductivity of the anode end-plate by the Ir-MMO coating, which has been ob-

served for coated flow-fields in the field of PEM-water electrolysis.[36,105] However, the difference of 0.04 V in the measurement of the single-cell voltage falls into the standard deviations of the experiments, as also shown in further experiments.

Furthermore, the trends of the ΔVoltages for the plain-Ti and the Ir-MMO systems converge toward the end of the experiments. Both reach a steady state at a positive value, indicating that the individual cells in the short-stacks operate on average at lower cell voltages. This effect can be traced to heating effects in the short-stack and has already been discussed.

Summed up, the performance indicators obtained for the single-cells show similar values and both single-cells behave analogs to their equivalent short-stack. Hence, the observations in the short-stack were yet again confirmed in the single-cell. We consistently observed a detrimental effect of a catalyst-coated anode flow-field as opposed to the expected reduction in anode overpotential.

In the obtained results, neither in the short stack nor in the single-cell an effect of the Ir-MMO coated plates and the related increase of the catalyst surface area is visible. First and foremost, the functionality of the two-material bipolar plates at current densities at 200 mA/cm² can be derived from these results. Regarding the expected reduction of the cell's voltages due to the catalyst surface increase two possibilities preventing an effect can be considered:

- Due to the low ionic conductivity of the anolyte, the Ir-MMO catalyst on the anode plates is isolated from the ionically conductive area and can not take part in the reaction.

- The increase of catalyst surface is negligible as the anode in the MEA already provides a porous structure with a significantly larger catalytic active surface area, than the geometric area provided by the flow fields.

To investigate the first assumption, the ionic conductivity of the anolyte is increased to prevent potential isolation of the Ir-MMO end plate. A 100 mM $KHCO_3$ solution with a conductivity of 8.55 mS/cm (25 °C) is used instead of the 10 mM $KHCO_3$ solution with conductivity of 1.09 mS/cm (25 °C). An experiment with the more concentrated anolyte is performed at 200 mA/cm^2 with the single-cell containing an Ir-MMO coated end plate.

The obtained cell voltage and FE(CO) of this experiment are illustrated in Figure 4.27, together with the values obtained in experiments with the 10 mM $KHCO_3$ solution and the single-cell with the Ir-MMO plate as well as the single-cell with the plain-Ti plates. A cell voltage of 3 V and a FE(CO) = 93 % was obtained with the 100 mM $KHCO_3$ solution in the single-cell with the Ir-MMO plate. As previously discussed, the single-cell with the Ir-MMO plate operates at 3.05 V and the plain-Ti single-cell at 3 V at 200 mA/cm², while in both experiments a FE(CO) of 95 % was observed.

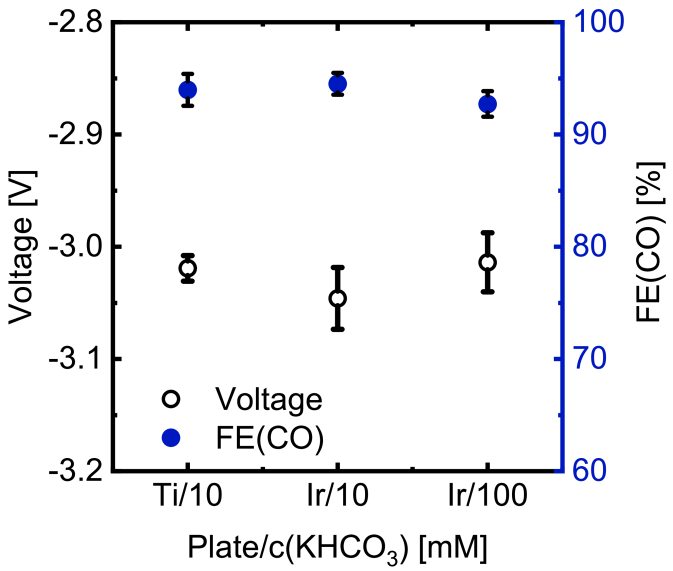

Figure 4.27: Cell voltage (left) and FE(CO) (right) for single cells containing a Ti Anode-Plate (Ti) or the Ir-MMO coated Anode plate (Ir) at 200 mA/cm^2. Comparison of experiments with 10 mM $KHCO_3$ and 100 mM $KHCO_3$ solution as anolyte.

The presented values of FE(CO) for the different experiments show minor differences, which are within the standard deviations ($\pm$ 3 %). Regarding the cell voltages, the increase of ionic conductivity via the $KHCO_3$ concentration in the anolyte led to lower cell voltages in the single-cell with the Ir-MMO plate. It appears, that the higher conductivity of the concentrated anolyte compensates for a loss of electrical conductivity by the Ir-MMO coating. Thus the Ir-MMO single-cell operates with the more concentrated anolyte at an identical cell voltage compared to the plain-Ti single-cell. However, considering the standard deviations ($\pm$ 0.03 V), the effect of the Ir-MMO end plate on the cell voltage is minor to not visible at all. This indicates, that the low conductive anolyte is not causing the absence of the voltage-reducing effect by the catalyst surface increase. More likely is the hypothesis, that the the catalyst surface increase is negligible compared to the existing catalyst surface area provided by the porous anode used in the MEA setup.

Impact of Current Density

In terms of the applied current density, beneficial effects of the catalyst surface increase may occur at higher loads. To investigate this hypothesis, experiments with the short-stack containing the catalyst-coated plates were performed at current densities of 300, 400 mA/cm², and additionally at 100 mA/cm². The results of the experiments at different current densities are illustrated in Figure 4.28(a)-(c). Figure 4.28(a) provides the FE(CO) for the short stacks, Figure 4.28(b) illustrates the obtained stack voltages, and in Figure 4.28(c) the voltage of the individual cells is shown. FE(CO) decreases from 95 % at 100 mA/cm^2 for both short-stacks to 83 % at 400 mA/cm^2 with the plain-Ti short stack and to 80 % with the short-stack containing the catalyst-coated plates. The voltage of the short-stacks decreases with increasing current density from 8.5 V at 100 mA/cm^2 to 9.8 V at 400 mA/cm^2. The voltages determined for the individual cells in the short-stacks with the Ir-MMO plates increase from voltages of 2.83 V at 100 mA/cm^2 to cell voltages of 3.27 V,(for TA and

MC) and 3.23 V (for TC) at 400 mA/cm^2. The lowest cell voltages were consistently observed for the TC.

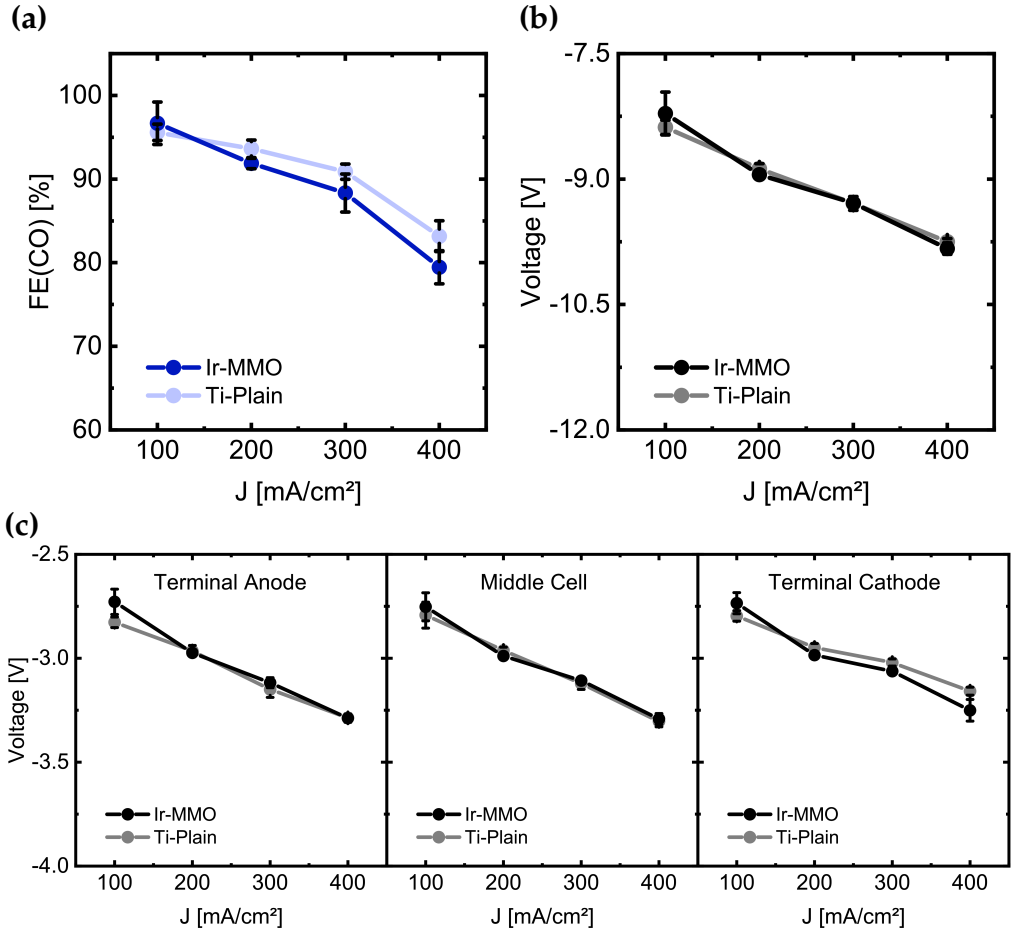

Figure 4.28: Results of experiments with short-stacks at different current densities: (a) FE(CO) of short-stacks over different current densities, (b) stack voltages over different current densities, and (c) voltages of individual cells in the short-stacks over different current densities.

Similar to the previous experiment no beneficial effect of the Ir-MMO coated plates of the FE(CO) could be determined. While FE(CO) reported for the plain-Ti short stack are higher compared to the short-stack containing the catalyst-coated plates, the values are within the standard deviations ($\pm$ 3 %) of the measurements. Almost identical behavior of the short-stacks regarding the stack voltages and the voltages of

the individual cells can be observed. For both short-stacks, the load increase by the current density increase leads to higher stack voltages, which is in the same way reflected by voltages determined for the individual cells. Analog to the plain-Ti short stack, the formation of temperature gradients leads in the short-stack with the Ir-MMO plates to a reduction of cell voltage in the TC. The almost identical behavior of the two short-stacks indicates that the Ir-MMO plates do not affect the short-stack performance.

Again a complementary study was conducted in a single-cell. The results of the electrochemical experiments with the single-cells at different current densities are illustrated in Figure 4.29 over the current densities. The obtained FE(CO) is visualized in Figure 4.29(a), and in Figure 4.29(b) the cell voltages are shown. For both single-cells, FE(CO) decreases with increasing current densities, starting from 95 % at 100 mA/cm² to 85 % and 83 % at 400 mA/cm² for the plain-Ti single cell and the Ir-MMO single cell. The cell voltages increase in both experiments from 2.8 V at 100 mA/cm² to 3.75 V and 3.65 V at 400 mA/cm² for the plain-Ti single-cell and the Ir-MMO single-cell.

Regarding the results displayed in Figure 4.29, a similar behavior of the single-cells at current densities between 100 mA/cm² and 300 mA/cm² can be derived. At 400 mA/cm², minor differences between the FE(CO) and the cell voltage can be observed. Compared to their equivalent short-stacks, the single-cells match the FE(CO) of the short-stacks and the cell voltage of the individual cells at current densities between 100 and 200 mA/cm². At higher current densities, the single-cells operate at higher voltages compared to the individual cells, as found previously.

Overall, a voltage reduction by the additional catalyst layer on the backing-plates was not observed. Nonetheless, the coating of anode backing-plates can prevent the formation of passive oxide layers on the backing-plates' surface. While a study concerning the effect of these lay-

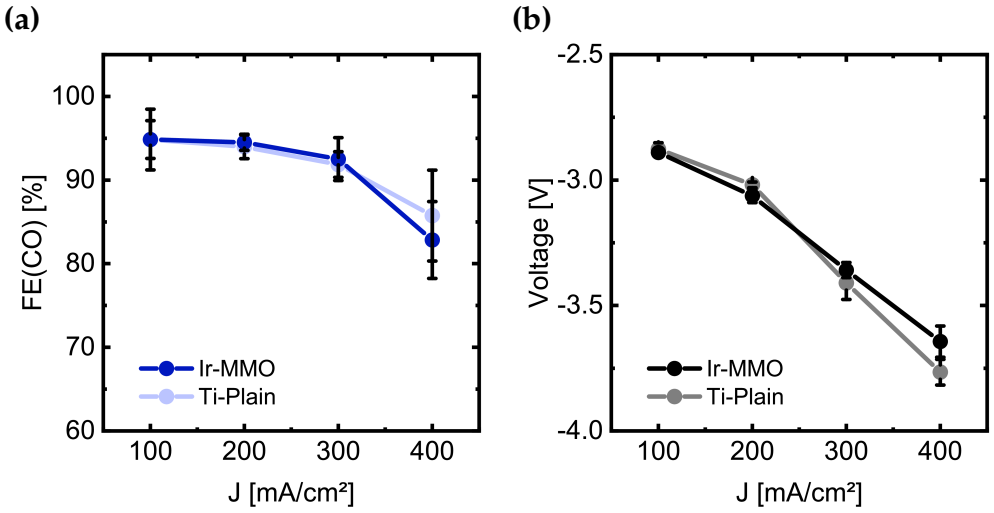

Figure 4.29: Results of experiments with single-cells at different current densities: (a) FE(CO) of single-cells over different current densities, (b) single-cell voltages over different current densities.

ers and the coating's impact in this context is not in the scope of this work, we emphasize, that materials other than Ir should be considered for backing-plate coating, since Ir is too rare and expensive to serve this function alone.

Conclusion on the Extended Role of End- and Bipolar-Plates

In this study, the modularity of the short stack design presented in Chapter 4.4 was further exploited by performing a study concerning the catalyst surface increase at the anode side of the CO_2-to-CO electrolyzer. In the three-cell short-stack with MEA cells, Ir-MMO coated backing-plates were implemented to enhance the OER at the anode sides of the cells. A two-material bipolar-plate was introduced to provide the catalyst to the anode sides only. This increase in the catalyst surface area did not lead to an expected reduction of the cell voltage, in neither the short-stack nor the equivalent single-cell. The increase of the catalyst surface area was regarding the catalyst surface area, which was already provided by the

porous anode in the MEA, negligible. However, experiments highlighted the value of the modular short-stack design. It enables addressing anodic or cathodic-specific challenges in a system that is closer to a scaled system than a single-cell.

Information for Appendix:

Appendix C provides an overview of the stack's and the single-cell's performances in terms of the performance indicators.

Chapter 5

Conclusion

In this work, stack designs with two distinct flow-cell concepts for the CO_2-to-CO electrolysis are presented and examined. Challenges originating from essential components for stacking are addressed entailing the modification of media flow compartments. Proposed are component designs that enhance cell performances, and enable the investigation of stack-related phenomena such as shunt currents and temperature effects, all while maintaining flexibility in the stacked system.

In an initial study, the most promising cell concepts for the CO_2-to-CO electrolysis were identified from the literature, examined within the same setup, and evaluated based on the figures of merit: Faraday efficiency, cell voltage, energy efficiency, and the formation of CO_2 at the anode. The cell configurations were compared to determine which flow-cell merits the investigation concerning the stacking. The examined cell designs entailed a flow-cell with an MEA, and a GDE-flow-cell. The MEA was assembled with an AEM. The GDE-flow-cell was tested with an AEM, a BPM in reverse bias, and a PEM. In alignment with the results presented in the literature, the GDE-flow-cells suffered from the large electrode distance, which led to higher cell voltages and lower energy efficiency compared to the flow-cell with the MEA.

Based on these results, and in the context of developing a stackable flow-cell design with mechanical integrity, the media flow-compartments

in the GDE-flow-cell were studied, which significantly contribute to the electrode distance. For this study, the GDE-flow-cell with the PEM was chosen, as it demonstrates the most promising potential of the investigated GDE-flow-cell configurations in terms of the defined figures of merit. First, a zero gap anode was implemented reducing the electrode distance and hence the cell voltage. An interdigitated gas flow-field combined with an ionically conductive spacer was introduced, to complete the force closure through the cell. These modifications on the GDE-flow-cell enhanced the performance in terms of the defined figures of merit and enabled the stacking of the cell which was demonstrated with a two-cell short stack.

In the short-stack, the stack voltage increases proportionally to the number of cells. However, lower FE(CO) was determined for the short-stack than for the single-cells. Despite the promising results, the short-stack concept was limited in terms of media flow management and thus in possibilities to investigate stack-specific effects such as shunt currents or individual cell behavior.

To overcome these limitations, a modular short-stack design was developed and tested with MEAs based on AEMs. Performance-enhancing effects appearing in a three-cell short-stack could be traced to the temperature development in the short-stack by exploiting the modularity of the short-stack. Temperature gradients were identified within the short-stack, leading to a position-dependent behavior of the individual cells in the short-stack. Furthermore, a detailed investigation of shunt current formation indicated a negligible effect of shunt-currents in the system.

Moreover, the modular design allows the investigation of anodic and cathodic-specific challenges in a stack. This was demonstrated in a study in which the role of the end- and bipolar-plates was expanded to participate in the OER at the anode to reduce the stack voltage. Catalyst-coated end-plates and two material bipolar-plates were implemented in the short-stack. The performance of the modified short-stack was compared to its equivalent single-cell and to the short-stack with the plain Ti plates. It was demonstrated, that the additional catalyst surface area was

negligible to the surface area that was already provided by the GDE-type anode in the MEA. The net effect of the catalyst coatings was detrimental in the examined time scale, as the coating added ohmic resistance to the cell.

In the presented work a solution is proposed for the key enabling step from single-cell to a stack, thus allowing an initial estimation of the flow-cells' behaviors in a system, that corresponds more to a scaled system than a single-cell. However, long-term experiments with the stacks are required to evaluate degradation processes and asses long-term performances. Coupling the scaling of the flow-cells in size with the scaling of the process by stacking needs to be considered in future research, to determine if the behavior of smaller cells in stacks translates.

Appendix A

Supplementary Information and Results for GDE-Flow-Cell with PEM

Preparation of Ion Exchange Resin and Conductivity Measurement

The ion exchange resin Amberlite IR-120 from Acros Organics was used to fill the catholyte chamber. Before use, the IER was saturated with a 1M $KHCO_3$ solution to minimize the acidic characteristics of the IER. The solution was exchanged with a fresh solution when bubble formation stopped. The process was repeated until no more bubbles formed in a fresh solution.
The conductivity of the IER was measured with a conductivity meter. A 20 ml test tube was filled with the IER (Figure A.1). Either distilled water or a 1M $KHCO_3$ solution was added to the test tube and conductivity was measured by inserting the conductivity probe (Figure A.1). A conductivity of 30 mS/cm was measured with the IER in distilled water. The conductivity increased to 55.3 mS/cm for the IER in 1M $KHCO_3$.

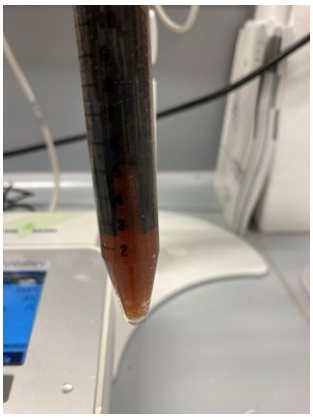

Figure A.1: Conductivity probe in a test tube filled with IER and 1M $KHCO_3$. The figure is adapted from [1].

Effect of IER on Differential Pressure in the Catholyte Chamber

The differential pressure in the catholyte chamber between the cell's entrance and exit was measured with a differential pressure transmitter (Table 3.1). The differential pressure was measured for a cell with and without the implemented spacer. Without the spacer, a differential pressure of 28(+/- 2.2) mbar was measured. The differential pressure increased to 120(+/- 2.2) mbar when the spacer was implemented in the cell.

Temperature Development in GDE-Flow-Cell

In figure A.2 the measured temperature of the catholyte is illustrated over time for different λ for an experiment with the cell containing M1 and the spacer. The cell operated at 100 mA/cm^2 with diluted and reduced CO_2 supply. The temperature was measured with the Metrohm Unitrode (Table 3.1) simultaneously with the pH values. The temperature of the catholyte at the cell's entrance increases from 25 °C to 27.8 °C after five hours. Behind the cell a temperature of 28 °C was determined after five hours. The temperatures increased more rapidly toward the beginning

of the experiment. Both curves flatten after one hour.

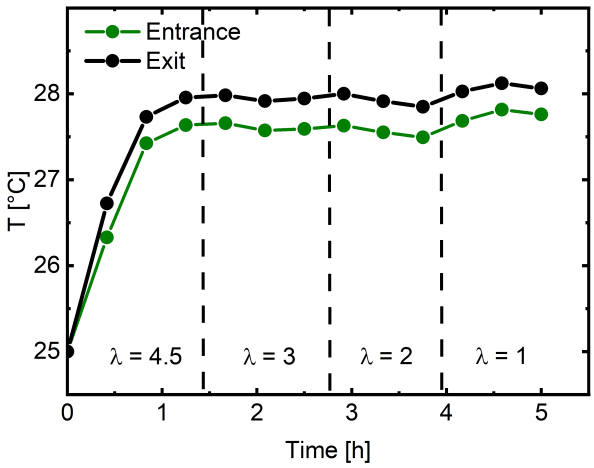

Figure A.2: Measurement of temperature in the catholyte in front and behind the cell in an experiment with the cell containing Meander and the spacer. The cell operated at 100 mA/cm^2 with diluted and reduced CO_2 supply. The figure is adapted from [1].

Measurement of pH Value

The pH value was measured in all experiments with the Metrohm Unitrode (Table 3.1) in the catholyte in front and behind the cell. In figure A.3 the measured pH of the catholyte is illustrated over time for different λ for an experiment with the cell containing M1 and the spacer. The cell operated at 100 mA/cm^2 with diluted and reduced CO_2 supply. The pH value of the catholyte at the cell entrance and the cell's exit is illustrated over time for different λ. At the cell's entrance, the pH of the catholyte increases from 8.55 at the start of the experiment to 9.6 after five hours. At the cell's exit, the pH value increases faster, reaching a value of 9.9 after five hours. The pH values increase faster at the beginning of the experiment. Both curves flatten towards the end of the experiment.

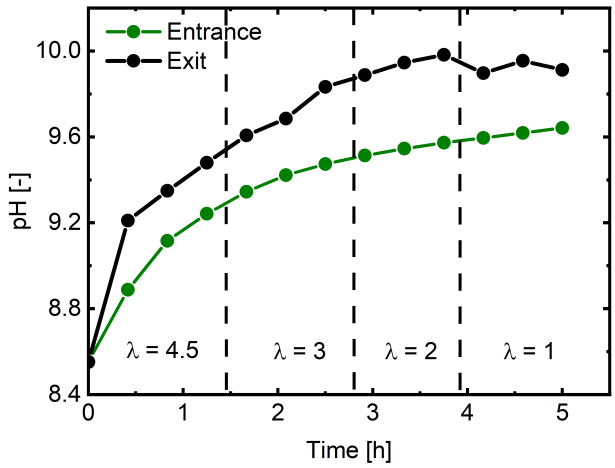

Figure A.3: Measurement of pH in the catholyte in front and behind the cell in an experiment with the cell containing M1 and the spacer. The cell operated at 100 mA/cm^2 with diluted and reduced CO_2 supply. The figure is adapted from [1].

Process Design for Stack Experiment

Figure A.4 illustrates the flowsheet of the experiment with the stack assembly. The catholytes (1M $KHCO_3$) were contained in the same reservoir and cycled parallel to the catholyte chambers with a volume flow of 50 ml/min. The anolytes (1M H_2SO_4) were also contained in the same reservoir and cycled via the same tube into the stack with a volume flow of 100 ml/min. Via the internal manifold, the feed gas was humidified and fed parallel into the stack. The gases appearing in the catholyte were separated from the catholyte in the reservoir and transported to the GC via a sweep gas (Ar). The product gas and the gas from the catholyte were analyzed with the GC and the gas counters.

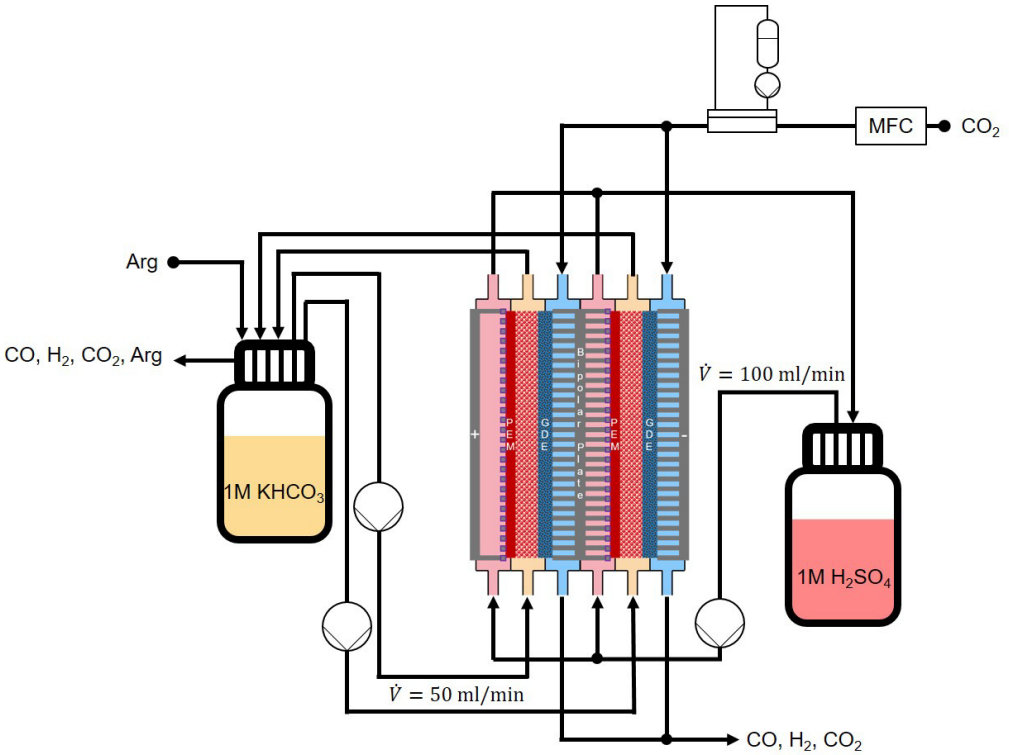

Figure A.4: Flowsheet of the process design for the experiment with the stack assembly. The figure is adapted from [1].

Appendix B

Supplementary Information and Results for Modular Short-Stack Design for MEAs

NMR-Spectroscopy Measurement of Anolyte

A sample of the anolyte was taken after a 48-hour experiment at 400 mA/cm² with the short-stack. The sample was analyzed via ^{1}H-NMR at 800MHz with water suppression using excitation sculpting with perfect echo in Bruker Avance III HD spectrometer (Bruker BioSpin GmbH, Rheinstetten, Germany). A 1 mM stock solution of trimethylsilyl propionate-d4 (TSP) in D_2O was added to the samples to serve as an internal standard for the chemical shift and quantification.

The NMR spectrum depicted in Figure B.1 depicts the presence of formate (8.2919 ppm) in a concentration of 0.5 mM in the anolyte sample. This amount corresponds to a Faraday efficiency of 0.04 % for formate, which is found to be negligible for the presented study. As previously discussed, a higher formate formation is possible, however its oxidation at the anode to CO_2 prevents its accumulation in the anolyte.

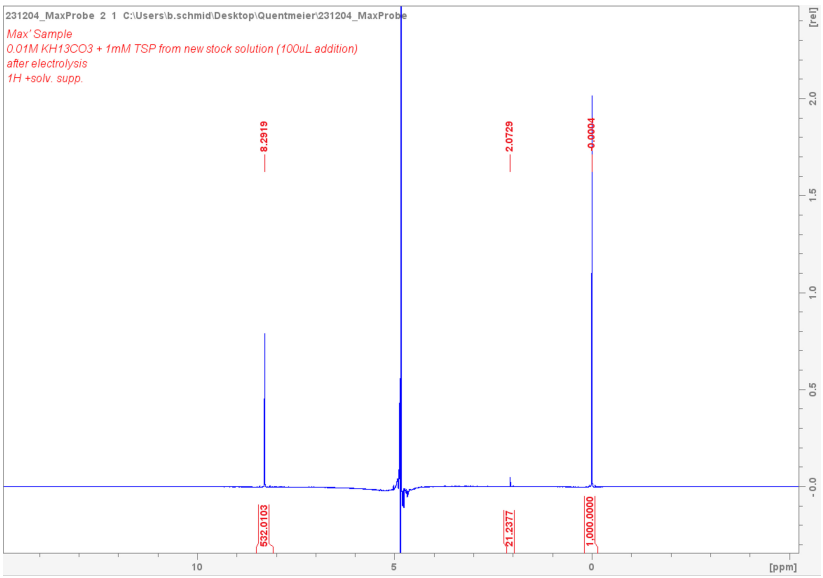

Figure B.1: Results of 1H NMR measurements with anolyte solution.

Impedance Measurements

In Figure B.2 (a)-(d) the Nyquist plots obtained with the single-cell in the experiments at ambient conditions and in experiments with the heated electrolyte are presented. The different Figures depict the plots obtained at the different current densities. For each current density step, a shift of the high-frequency resistance and the low-frequency resistance toward lower values can be observed, when increasing the temperature.

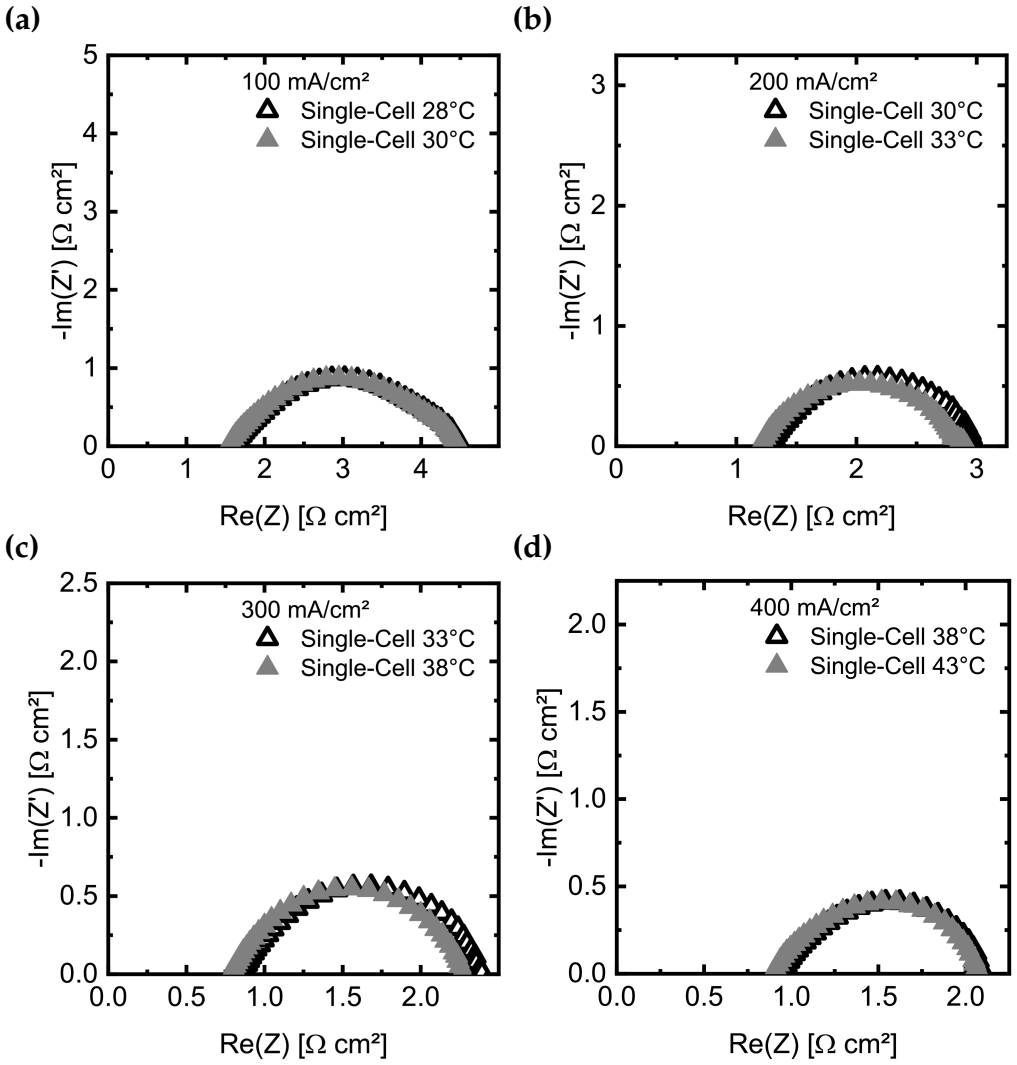

Figure B.2: Nyquist plots obtained with single-cell at different temperatures and different current densities; (a) 100 mA/cm² at 28 °C and 30 °C, (b) 200 mA/cm² at 30 °C and 33 °C, (c) 300 mA/cm² at 33 °C and 38 °C, (d) 400 mA/cm² at 36 °C and 43 °C. The figure is adapted from [2].

In Figure B.3(a), the Nyquist plots obtained with the short-stack at different current densities are presented. Similar to the plots obtained with the single-cell, a decrease in high-frequency resistance and low-frequency resistance can be observed with increasing current density. Figure B.3(b) depicts the Nyquist plots for the individual cells in the short-stack operating at 300 mA/cm². Minor variations in high-frequency resistances and low-frequency resistances can be observed between the individual cells.

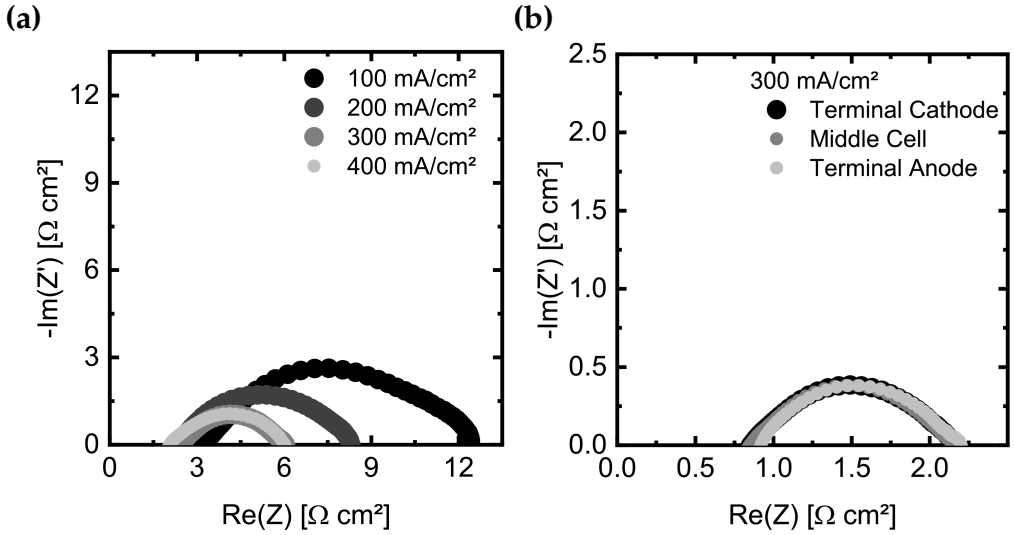

Figure B.3: (a) Nyquist plots obtained with short-stack at different current densities; (b) Nyquist plots obtained at 300 mA/cm² for the individual cells in the short-stack. The figure is adapted from [2].

Appendix C

Overview of Flow-Cell Performances

Performance GDE-flow-cell

In Table C.1 the performances of the GDE-flow-cell (Chapter 4.2) in different stages of modification are given by the performance indicators, to highlight the impact of each modification made to the cell. Additionally, the performance of the two-cell short-stack is listed. As extensively discussed in Chapter 4.1 and 4.2, the switch from the Ir-plate to a zero gap anode reduces the U_{Cell}. Subsequently, it increases the energy efficiency, the implementation of the spacer leads to an increase of U_{Cell} and a decrease of energy efficiency, and the implementation of the Rake_1 flow-field enhances U_{Cell} and thus increases the energy efficiency. While FE(CO) was similar for the listed GDE-flow-cells, the value of FE(CO) dropped for the two-cell short-stack, leading to a decrease in energy efficiency.

Table C.1: GDE-Flow-cell stack vs. single-cell performance

No. of Cells	j [mA/cm²]	Flowfield	Anode	Spacer	FE(CO) [%]	U [V]	$\epsilon_{(CO)}$ [%]	EPC [$\frac{kWh}{Nm}$]
1	100	Chamber_1	Ir-Plate	-	93.63	-4.69	26.36	10.98
1	100	Chamber_1	Zero-Gap	-	95.47	-4.11	30.69	9.43
1	100	Chamber_1	Zero-Gap	IER	94.25	-4.12	30.23	9.58
1	100	Rake_1	Zero-Gap	IER	94.3	-3.88	32.12	9.01
2	100	Rake_1	Zero-Gap	IER	77.30	-7.75	26.53	10.91

Performance Single Flow-Cell with MEA

In Table C.2 the performance of the single-cells containing the MEA at $= 100\,\text{mA/cm}^2$ are listed. Compared are the single-cells operating with the old flow-field presented in Chapter 4.2 and the new flow-field described in Chapter 4.4. In terms of the performances, the cell with the new flow-field demonstrated lower U_{Cell} at the same current density, which increased the energy efficiency. The differing performances of the cells are based on the architecture of flow-fields (Figure C.1) The old flow-field directs the media flows along the front side of the flow-field (Figure C.1a). The media flow channels thereby reduce the contact area of the current collector to the electrodes, which leads to a larger U_{Cell}. Furthermore, the sealing of the MEA flow-cells with the old flow-fields was insufficient, meaning that leakage of electrolyte was observed while operating the cell. With the new flow-field, these limitations could be overcome by directing the media flows from the rear side of the plates (Figure C.1b). Thus, the enhanced sealing and the increased contact area of the electrodes to the current collectors increased the performances in terms of U_{Cell} and consequently in terms of energy efficiency.

Table C.2: Singe-cell with MEA performance; old vs. new flowfield design

No. of Cells	Flow-field	j [mA/cm²]	FE(CO) [%]	U_{Cell} [V]	$\epsilon_{th(CO)}$ [%]	EPC [$\frac{kWh}{Nm}$]
1	Old (Chapter 4.1)	100	93.74	-2.99	41.39	6.99
1	New (Chapter 4.4)	100	94.85	-2.88	43.52	6.65

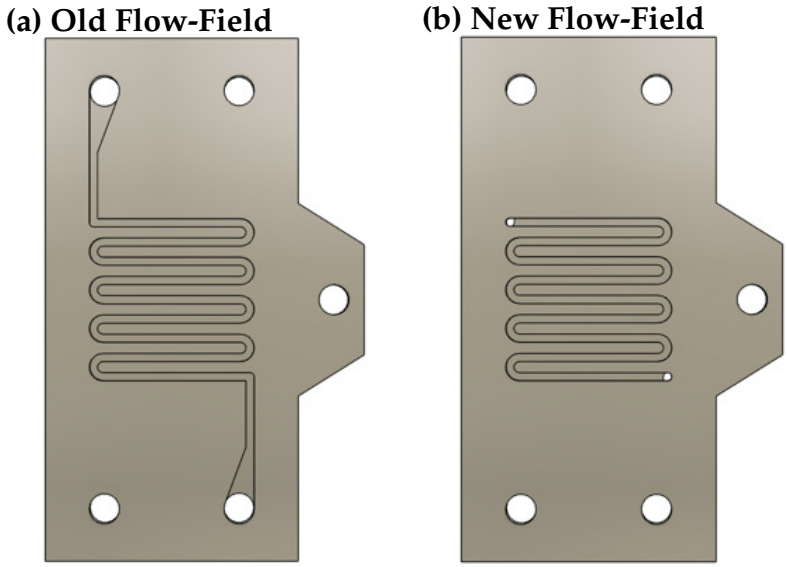

Figure C.1: Illustrations of (a) old and (b) new flow-field. The media flow enters old flow-field from the front side, the media flow enters the new flow-field from the rear side.

Overview of Performances for Single-Cell and Short-Stacks with MEA

In Table C.3 the performances of the single-cell with the MEA as well as the performances of the short-stacks are listed for different j in terms of the performance indicators. The effects of the stacking on the cell performances have been extensively discussed in Chapter 4.4, thus Table C.3 is provided to facilitate the comparison of the performances. In a nutshell, the energy efficiencies decreased with increasing j due to the higher load. Higher energy efficiencies were obtained with the short-stacks due to temperature effects, which decrease U_{Cell} of the individual cells in the short-stacks. An increase of the catalyst surface area at the anodes by implementing Ir-MMO coated flow-field did not lead to a performance, as the supplementary catalyst surface was negligible to the already existing catalyst surface.

Table C.3: Flow-cell with MEA; stacks and single-cell performance at different j

No. of Cells	Anode-Plate	j [mA/cm²]	FE(CO) [%]	U [V]	$\epsilon_{(CO)}$ [%]	EPC [$\frac{kWh}{Nm}$]
1	Ti	100	94.85	-2.88	43.52	6.65
1	Ti	200	93.97	-3.01	41.25	7.01
1	Ti	300	91.85	-3.41	35.59	8.13
1	Ti	400	85.75	-3.77	30.06	9.63
3	Ti	100	95.85	-8.38	45.34	6.38
3	Ti	200	93.61	-8.87	41.84	6.92
3	Ti	300	90.97	-9.29	38.82	7.46
3	Ti	400	83.17	-9.75	33.82	8.56
3	Ir-MMO	100	96.66	-8.21	46.67	6.20
3	Ir-MMO	200	91.85	-8.95	40.68	7.11
3	Ir-MMO	300	88.33	-9.29	37.69	7.68
3	Ir-MMO	400	79.45	-9.83	32.04	8.56

Abbreviations and Symbols

Abbreviations

CO_2	Carbon Dioxide
CO	Carbon Monoxide
H_2	Hydrogen
$KHCO_3$	Potassium Bicarbonate
H_2SO_4	Sulfuric Acid
H_2O	Water
Ar	Argon
KOH	Potassium Hydroxide
CH_3OH	Methanol
CH_3COOH	Acetic Acid
Cl_2	Chlorine
$COCl_2$	Phosgene
C_2H_4	Ethen
$C_3H_6O_2$	Propionic Acid
C_4H_6	Butadien
$HO_2C(CH_2)_4CO_2H$	Adipic Acid
$C_2H_4O_2$	Methyl formate
HCO_3^-	Bicarbonate

Abbreviations

CO_3^{2-}	Carbonate
OH^-	Hydroxide Ions
H^+	Protons
K^+	Potassium Ions
MEA	Membrane Electrode Assembly
GDE	Gas Diffusion Electrode
AEM	Anion Exchange Membrane
PEM	Proton Exchange Membrane
BPM	Bipolar Membrane
OER	Oxygen Evolution Reaction
HER	Hydrogen Evolution Reaction
IER	Ion Exchange Resin

Symbols

λ	Feed Gas Parameter	[-]
η	Overpotential	[V]
FE	Faraday Efficiency	[%]
F	Faraday Constant	[C/mol]
I	Current	[A]
j	Current Density	[mA/cm²]
U_{Cell}	Cell Voltage	[V]
ΔVoltage	Differential Voltage	[V]
z	Number of Exchanged Electrons	[-]
R	Ideal Gas Constant	[J/mol·K]
T	Temperature	[K]
c	Concentration	[mol/L]
φ	Concentration	[%]
p	Pressure	[Pa]
EPC	Electrical Power Consumption	[%]
ϵ	Energy Efficiency	[%]
ΔG	free Gibbs energy	[kJ/mol]
E	Reversible Cell Voltage	[V]
E^0	Equilibrium Cell Potential	[V]
$\dot{V}$	Volume flow	[ml/min]
$\dot{n}$	Molar flow	[mol/min]
$V_{CO_{mol}}$	Molar Volume of CO	[L/mol]
U_{act}	Activation Overpotential	[V]
U_{tran}	Mass Transport Overpotential	[V]
U_{ohm}	Ohmic Overpotential	[V]
α	Charge Transfer Coefficient	[-]
V_m	Molar Volume	[l/mol]

Bibliography

[1] M. Quentmeier, B. Schmid, H. Tempel, H. Kungl, R.-A. Eichel, *ACS Sustainable Chemistry & Engineering* **2023**, *11*, 679–688.

[2] M. Quentmeier, B. Schmid, H. Tempel, R.-A. Eichel, *ACS Sustainable Chemistry & Engineering* **2024**, *12*, 3876–3885.

[3] L. M. Aeshala, R. Uppaluri, A. Verma, *Physical chemistry chemical physics : PCCP* **2014**, *16*, 17588–17594.

[4] N. Berghout, S. McCulloch, A. Baylin-Stern, *International Energy Agency* **2020**.

[5] S. Nitopi, E. Bertheussen, S. B. Scott, X. Liu, A. K. Engstfeld, S. Horch, B. Seger, I. E. L. Stephens, K. Chan, C. Hahn, J. K. Nørskov, T. F. Jaramillo, I. Chorkendorff, *Chemical reviews* **2019**, *119*, 7610–7672.

[6] R. G. Grim, Z. Huang, M. T. Guarnieri, J. R. Ferrell, L. Tao, J. A. Schaidle, *Energy & Environmental Science* **2020**, *13*, 472–494.

[7] Y. Cheng, P. Hou, X. Wang, P. Kang, *Accounts of chemical research* **2022**, *55*, 231–240.

[8] M. Jouny, W. Luc, F. Jiao, *Industrial & Engineering Chemistry Research* **2018**, *57*, 2165–2177.

[9] R. I. Masel, Z. Liu, H. Yang, J. J. Kaczur, D. Carrillo, S. Ren, D. Salvatore, C. P. Berlinguette, *Nature Nanotechnology* **2021**, *16*, 118–128.

[10] R. Krause, D. Reinisch, C. Reller, H. Eckert, D. Hartmann, D. Taroata, K. Wiesner–Fleischer, A. Bulan, A. Lueken, G. Schmid, *Chemie Ingenieur Technik* **2020**, *92*, 53–61.

[11] B. Endrődi, E. Kecsenovity, A. Samu, F. Darvas, R. V. Jones, V. Török, A. Danyi, C. Janáky, *ACS Energy Letters* **2019**, *4*, 1770–1777.

[12] E. V. Kondratenko, G. Mul, J. Baltrusaitis, G. O. Larrazábal, J. Pérez-Ramírez, *Energy & Environmental Science* **2013**, *6*, 3112.

[13] J.-M. Savéant, *Chemical reviews* **2008**, *108*, 2348–2378.

[14] J. Kim, W. Guo, H. Kim, S. Choe, S. Y. Kim, S. H. Ahn, *ACS Sustainable Chemistry & Engineering* **2022**, *10*, 14092–14111.

[15] W. A. Smith, T. Burdyny, D. A. Vermaas, H. Geerlings, *Joule* **2019**, *3*, 1822–1834.

[16] D. Bell, D. Rall, M. Großeheide, L. Marx, L. Hülsdünker, M. Wessling, *Electrochemistry Communications* **2020**, *111*, 106645.

[17] H. Yang, J. J. Kaczur, S. D. Sajjad, R. I. Masel, *Journal of CO2 Utilization* **2017**, *20*, 208–217.

[18] Y. Hori, H. Wakebe, T. Tsukamoto, O. Koga, *Electrochimica Acta* **1994**, *39*, 1833–1839.

[19] J. Choi, M. J. Kim, S. H. Ahn, I. Choi, J. H. Jang, Y. S. Ham, J. J. Kim, S.-K. Kim, *Chemical Engineering Journal* **2016**, *299*, 37–44.

[20] S. Verma, Y. Hamasaki, C. Kim, W. Huang, S. Lu, H.-R. M. Jhong, A. A. Gewirth, T. Fujigaya, N. Nakashima, P. J. A. Kenis, *ACS Energy Letters* **2018**, *3*, 193–198.

[21] E. Robens, B. Hecker, H. Kungl, H. Tempel, R.-A. Eichel, *ACS Applied Energy Materials* **2023**, *6*, 7571–7577.

[22] J.-B. Vennekoetter, R. Sengpiel, M. Wessling, *Chemical Engineering Journal* **2019**, *364*, 89–101.

[23] E. R. Corson, A. Subramani, J. K. Cooper, R. Kostecki, J. J. Urban, B. D. McCloskey, *Chemical communications (Cambridge England)* **2020**, *56*, 9970–9973.

[24] C. P. O'Brien, R. K. Miao, A. Shayesteh Zeraati, G. Lee, E. H. Sargent, D. Sinton, *Chemical Reviews* **2024**, *124*, 3648–3693.

[25] B. Endrődi, G. Bencsik, F. Darvas, R. Jones, K. Rajeshwar, C. Janáky, *Progress in Energy and Combustion Science* **2017**, *62*, 133–154.

[26] J.-P. Jones, G. K. S. Prakash, G. A. Olah, *Israel Journal of Chemistry* **2014**, *54*, 1451–1466.

[27] X. Zhang, S.-X. Guo, K. A. Gandionco, A. M. Bond, J. Zhang, *Materials Today Advances* **2020**, *7*, 100074.

[28] J.-B. Vennekötter, T. Scheuermann, R. Sengpiel, M. Wessling, *Journal of CO2 Utilization* **2019**, *32*, 202–213.

[29] R. Küngas, *Journal of The Electrochemical Society* **2020**, *167*, 044508.

[30] J. A. Rabinowitz, M. W. Kanan, *Nature Communications* **2020**, *11*, 5231.

[31] M. G. Kibria, J. P. Edwards, C. M. Gabardo, C.-T. Dinh, A. Seifitokaldani, D. Sinton, E. H. Sargent, *Advanced Materials* **2019**, *31*, 1807166.

[32] B. Endrődi, E. Kecsenovity, A. Samu, T. Halmágyi, S. Rojas-Carbonell, L. Wang, Y. Yan, C. Janáky, *Energy & Environmental Science* **2020**, *13*, 4098–4105.

[33] H.-R. ". Jhong, S. Ma, P. J. Kenis, *Current Opinion in Chemical Engineering* **2013**, *2*, Nanotechnology / Separation engineering, 191–199.

[34] T. Reichbauer, B. Schmid, K.-.-M. Vetter, D. Reinisch, N. Martić, C. Reller, A. Grasruck, R. Dorta, G. Schmid, *Electrochemical Science Advances* **2023**, e2300024.

[35] B. Han, S. M. Steen, J. Mo, F.-Y. Zhang, *International Journal of Hydrogen Energy* **2015**, *40*, 7006–7016.

[36] M. Carmo, D. L. Fritz, J. Mergel, D. Stolten, *International Journal of Hydrogen Energy* **2013**, *38*, 4901–4934.

[37] J. E. Nutting, J. B. Gerken, A. G. Stamoulis, D. L. Bruns, S. S. Stahl, *The Journal of Organic Chemistry* **2021**, *86*, 15875–15885.

[38] C. Delacourt, P. L. Ridgway, J. B. Kerr, J. Newman, *Journal of The Electrochemical Society* **2008**, *155*, B42.

[39] K. P. Kuhl, E. R. Cave, D. N. Abram, T. F. Jaramillo, *Energy & Environmental Science* **2012**, *5*, 7050.

[40] S. Liang, N. Altaf, L. Huang, Y. Gao, Q. Wang, *Journal of CO2 Utilization* **2020**, *35*, 90–105.

[41] W. H. Lee, C. Lim, S. Y. Lee, K. H. Chae, C. H. Choi, U. Lee, B. K. Min, Y. J. Hwang, H.-S. Oh, *Nano Energy* **2021**, *84*, 105859.

[42] J. P. Edwards, T. Alerte, C. P. O'Brien, C. M. Gabardo, S. Liu, J. Wicks, A. Gaona, J. Abed, Y. C. Xiao, D. Young, A. Sedighian Rasouli, A. Sarkar, S. A. Jaffer, H. L. MacLean, E. H. Sargent, D. Sinton, *ACS Energy Letters* **2023**, *8*, 2576–2584.

[43] K. Fernández-Caso, G. Díaz-Sainz, M. Alvarez-Guerra, A. Irabien, *ACS Energy Letters* **2023**, *8*, 1992–2024.

[44] P.-F. Mar, E. Tzimas, *Publications Office of the European Union: Luxemburg* **2016**.

[45] Z. Yuan, M. R. Eden, R. Gani, *Industrial & Engineering Chemistry Research* **2016**, *55*, 3383–3419.

[46] J. J. Kaczur, H. Yang, Z. Liu, S. D. Sajjad, R. I. Masel, *C — Journal of Carbon Research* **2020**, *6*, 33.

[47] S. van Bavel, S. Verma, E. Negro, M. Bracht, *ACS Energy Letters* **2020**, *5*, 2597–2601.

[48] T. Haas, R. Krause, R. Weber, M. Demler, G. Schmid, *Nature Catalysis* **2018**, *1*, 32–39.

[49] W. Reutemann, H. Kieczka in *Ullmann's Encyclopedia of Industrial Chemistry*, John Wiley & Sons, Ltd, **2000**.

[50] J. Bierhals in *Ullmann's Encyclopedia of Industrial Chemistry*, John Wiley & Sons, Ltd, **2001**.

[51] H. Cheung, R. S. Tanke, G. P. Torrence in *Ullmann's Encyclopedia of Industrial Chemistry*, John Wiley & Sons, Ltd, **2000**.

[52] B. Kim, S. Ma, H.-R. Molly Jhong, P. J. Kenis, *Electrochimica Acta* **2015**, *166*, 271–276.

[53] Y. C. Li, D. Zhou, Z. Yan, R. H. Gonçalves, D. A. Salvatore, C. P. Berlinguette, T. E. Mallouk, *ACS Energy Letters* **2016**, *1*, 1149–1153.

[54] M. T. Musser in *Ullmann's Encyclopedia of Industrial Chemistry*, John Wiley & Sons, Ltd, **2000**.

[55] D. Reinisch, B. Schmid, N. Martić, R. Krause, H. Landes, M. Hanebuth, K. J. Mayrhofer, G. Schmid, *Zeitschrift für Physikalische Chemie* **2019**, *0*.

[56] D. Reinisch, T. Reichbauer, K. M. Vetter, N. Martić, K. J. J. Mayrhofer, G. Schmid, *Catalysis Science & Technology* **2022**, *12*, 5829–5840.

[57] J. E. Huang, F. Li, A. Ozden, A. Sedighian Rasouli, F. P. García de Arquer, S. Liu, S. Zhang, M. Luo, X. Wang, Y. Lum, Y. Xu, K. Bertens, R. K. Miao, C.-T. Dinh, D. Sinton, E. H. Sargent, *Science (New York N.Y.)* **2021**, *372*, 1074–1078.

[58] J. Baessler, T. Oliveira, R. Keller, M. Wessling, *ACS Sustainable Chemistry & Engineering* **2023**, *11*, 6822–6828.

[59] D. Li, J. Yang, J. Lian, J. Yan, S. (Frank) Liu, *Journal of Energy Chemistry* **2023**, *77*, 406–419.

[60] J.-H. Guo, W.-Y. Sun, *Applied Catalysis B: Environmental* **2020**, *275*, 119154.

[61] X. Jiang, Le Ke, K. Zhao, X. Yan, H. Wang, X. Cao, Y. Liu, L. Li, Y. Sun, Z. Wang, D. Dang, N. Yan, *Nature Communications* **2024**, *15*.

[62] C.-T. Dinh, F. P. García de Arquer, D. Sinton, E. H. Sargent, *ACS Energy Letters* **2018**, *3*, 2835–2840.

[63] E. J. Dufek, T. E. Lister, M. E. McIlwain, *Journal of Applied Electrochemistry* **2011**, *41*, 623–631.

[64] M. Heßelmann, B. C. Bräsel, R. G. Keller, M. Wessling, *Electrochemical Science Advances* **2023**, *3*, 2100160.

[65] D. Higgins, C. Hahn, C. Xiang, T. F. Jaramillo, A. Z. Weber, *ACS Energy Letters* **2019**, *4*, 317–324.

[66] N. Gao, C. Quiroz-Arita, L. A. Diaz, T. E. Lister, *Journal of CO2 Utilization* **2021**, *43*, 101365.

[67] A. Gawel, T. Jaster, D. Siegmund, J. Holzmann, H. Lohmann, E. Klemm, U.-P. Apfel, *iScience* **2022**, *25*, 104011.

[68] M. Großeheide, D. Schaffeld, R. Keller, M. Wessling, *Electrochemistry Communications* **2023**, *150*, 107487.

[69] S. Garg, C. A. Giron Rodriguez, T. E. Rufford, J. R. Varcoe, B. Seger, *Energy & Environmental Science* **2022**, *15*, 4440–4469.

[70] T. Luo, S. Abdu, M. Wessling, *Selectivity of ion exchange membranes: A review*, *Vol. 555*, **2018**.

[71] H. Strathmann, *Desalination* **2010**, *264*, Special Issue to honour the previous editor Miriam Balaban, 268–288.

[72] Z. Qiu, Y. Yun, M. He, L. Wang, *Chemical Engineering Journal* **2023**, *456*, 140942.

[73] Z. Liu, H. Yang, R. Kutz, R. I. Masel, *Journal of The Electrochemical Society* **2018**, *165*, J3371–J3377.

[74] N. T. Nesbitt, T. Burdyny, H. Simonson, D. Salvatore, D. Bohra, R. Kas, W. A. Smith, *ACS Catalysis* **2020**, *10*, 14093–14106.

[75] C. Lee, B. Zhao, J. K. Lee, K. F. Fahy, K. Krause, A. Bazylak, *iScience* **2020**, *23*, 101094.

[76] M. Ma, E. L. Clark, K. T. Therkildsen, S. Dalsgaard, I. Chorkendorff, B. Seger, *Energy & Environmental Science* **2020**, *13*, 977–985.

[77] J. Lee, J. Lim, C.-W. Roh, H. S. Whang, H. Lee, *Journal of CO2 Utilization* **2019**, *31*, 244–250.

[78] S. Ren, D. Joulié, D. Salvatore, K. Torbensen, M. Wang, M. Robert, C. P. Berlinguette, *Science (New York N.Y.)* **2019**, *365*, 367–369.

[79] K. Torbensen, D. Joulié, S. Ren, M. Wang, D. Salvatore, C. P. Berlinguette, M. Robert, *ACS Energy Letters* **2020**, *5*, 1512–1518.

[80] Á. Vass, A. Kormányos, Z. Kószó, B. Endrődi, C. Janáky, *ACS Catalysis* **2022**, *12*, 1037–1051.

[81] L.-C. Weng, A. T. Bell, A. Z. Weber, *Energy & Environmental Science* **2019**, *12*, 1950–1968.

[82] G. O. Larrazábal, P. Strøm-Hansen, J. P. Heli, K. Zeiter, K. T. Therkildsen, I. Chorkendorff, B. Seger, *ACS applied materials & interfaces* **2019**, *11*, 41281–41288.

[83] D. Salvatore, C. P. Berlinguette, *ACS Energy Letters* **2020**, *5*, 215–220.

[84] N. Ziv, D. R. Dekel, *Electrochemistry Communications* **2018**, *88*, 109–113.

[85] L. Ge, H. Rabiee, M. Li, S. Subramanian, Y. Zheng, J. H. Lee, T. Burdyny, H. Wang, *Chem* **2022**, *8*, 663–692.

[86] G. A. El-Nagar, F. Haun, S. Gupta, S. Stojkovikj, M. T. Mayer, *Nature Communications* **2023**, *14*, 2062.

[87] Z. Yin, H. Peng, X. Wei, H. Zhou, J. Gong, M. Huai, L. Xiao, G. Wang, J. Lu, L. Zhuang, *Energy & Environmental Science* **2019**, *12*, 2455–2462.

[88] P. Mardle, S. Cassegrain, F. Habibzadeh, Z. Shi, S. Holdcroft, *The Journal of Physical Chemistry C* **2021**, *125*, 25446–25454.

[89] M. R. Thorson, K. I. Siil, P. J. A. Kenis, *Journal of The Electrochemical Society* **2013**, *160*, F69–F74.

[90] A. Reyes, R. P. Jansonius, B. A. W. Mowbray, Y. Cao, D. G. Wheeler, J. Chau, D. J. Dvorak, C. P. Berlinguette, *ACS Energy Letters* **2020**, *5*, 1612–1618.

[91] M. R. Singh, Y. Kwon, Y. Lum, J. W. Ager, A. T. Bell, *Journal of the American Chemical Society* **2016**, *138*, 13006–13012.

[92] D. A. Salvatore, C. M. Gabardo, A. Reyes, C. P. O'Brien, S. Holdcroft, P. Pintauro, B. Bahar, M. Hickner, C. Bae, D. Sinton, E. H. Sargent, C. P. Berlinguette, *Nature Energy* **2021**, *6*, 339–348.

[93] M. A. Blommaert, R. Sharifian, N. U. Shah, N. T. Nesbitt, W. A. Smith, D. A. Vermaas, *Journal of Materials Chemistry A* **2021**, *9*, 11179–11186.

[94] M. Heßelmann, J. K. Lee, S. Chae, A. Tricker, R. G. Keller, M. Wessling, J. Su, D. Kushner, A. Z. Weber, X. Peng, *ACS Applied Materials & Interfaces* **2024**, *16*, 24649–24659.

[95] M. Wrobel, S. Kriescher, T. Schiffer, R. Keller, M. Wessling, *Chemical Engineering Journal* **2023**, *474*, 145335.

[96] D. A. Vermaas, W. A. Smith, *ACS Energy Letters* **2016**, *1*, 1143–1148.

[97] D. M. Weekes, D. A. Salvatore, A. Reyes, A. Huang, C. P. Berlinguette, *Accounts of chemical research* **2018**, *51*, 910–918.

[98] D. A. Salvatore, D. M. Weekes, J. He, K. E. Dettelbach, Y. C. Li, T. E. Mallouk, C. P. Berlinguette, *ACS Energy Letters* **2018**, *3*, 149–154.

[99] E. W. Lees, M. Goldman, A. G. Fink, D. J. Dvorak, D. A. Salvatore, Z. Zhang, N. W. X. Loo, C. P. Berlinguette, *ACS Energy Letters* **2020**, *5*, 2165–2173.

[100] T. Li, E. W. Lees, M. Goldman, D. A. Salvatore, D. M. Weekes, C. P. Berlinguette, *Joule* **2019**, *3*, 1487–1497.

[101] P. Millet, R. Ngameni, S. A. Grigoriev, N. Mbemba, F. Brisset, A. Ranjbari, C. Etiévant, *International Journal of Hydrogen Energy* **2010**, *35*, 5043–5052.

[102] S. Siracusano, V. Baglio, N. Briguglio, G. Brunaccini, A. Di Blasi, A. Stassi, R. Ornelas, E. Trifoni, V. Antonucci, A. S. Aricò, *International Journal of Hydrogen Energy* **2012**, *37*, 1939–1946.

[103] M. Goldman, A. Prajapati, E. Duoss, S. Baker, C. Hahn, *Current Opinion in Electrochemistry* **2023**, *39*, 101248.

[104] S. Subramanian, J. Middelkoop, T. Burdyny, *Sustainable Energy & Fuels* **2021**, *5*, 6040–6048.

[105] H. Teuku, I. Alshami, J. Goh, M. S. Masdar, K. S. Loh, *International Journal of Energy Research* **2021**, *45*, 20583–20600.

[106] J. J. Kaczur, H. Yang, Z. Liu, S. D. Sajjad, R. I. Masel, *Frontiers in chemistry* **2018**, *6*, 263.

[107] J. Na, B. Seo, J. Kim, C. W. Lee, H. Lee, Y. J. Hwang, B. K. Min, D. K. Lee, H.-S. Oh, U. Lee, *Nature Communications* **2019**, *10*, 5193.

[108] T. F. O'Brien, T. V. Bommaraju, F. Hine, *Handbook of chlor-alkali technology*, Springer, New York, **2005**.

[109] C. Rozain, E. Mayousse, N. Guillet, P. Millet, *Applied Catalysis B: Environmental* **2016**, *182*, 123–131.

[110] M. Rizwan, V. Alstad, J. Jäschke, *Design considerations for industrial water electrolyzer plants*, *Vol. 46*, **2021**.

[111] H. S. Burney, R. E. White, *Journal of The Electrochemical Society* **1988**, *135*, 1609–1612.

[112] R. B. Kutz, Q. Chen, H. Yang, S. D. Sajjad, Z. Liu, I. R. Masel, *Energy Technology* **2017**, *5*, 929–936.

[113] M. E. Leonard, L. E. Clarke, A. Forner-Cuenca, S. M. Brown, F. R. Brushett, *ChemSusChem* **2020**, *13*, 400–411.

[114] P. Dlugolkecki, J. Dabrowska, K. Nijmeijer, M. Wessling, *Journal of Membrane Science* **2010**, *347*, 101–107.

[115] J.-H. Han, K.-s. Hwang, H. Jeong, S.-Y. Byeon, J.-Y. Nam, C.-S. Kim, H. Kim, S. Yang, J. Y. Choi, N. Jeong, *Journal of Applied Electrochemistry* **2019**, *49*, 517–528.

[116] B. Zhang, H. Gao, Y. Chen, *Environmental science & technology* **2015**, *49*, 14717–14724.

[117] E. Dejean, E. Laktionov, J. Sandeaux, R. Sandeaux, G. Pourcelly, C. Gavach, *Desalination* **1997**, *114*, 165–173.

[118] D. V. Golubenko, J. Křivčík, A. B. Yaroslavtsev, *Petroleum Chemistry* **2015**, *55*, 769–775.

[119] E. Korngold, *Desalination* **1975**, *16*, 225–233.

[120] P. Fortin, T. Khoza, X. Cao, S. Y. Martinsen, A. Oyarce Barnett, S. Holdcroft, *Journal of Power Sources* **2020**, *451*, 227814.

[121] P. Dlugolkecki, P. Ogonowski, S. J. Metz, M. Saakes, K. Nijmeijer, M. Wessling, **2010**, *349*, 369–379.

[122] P. Mardle, A. Gangrade, T. Saatkamp, Z. Jiang, S. Cassegrain, N. Zhao, Z. Shi, S. Holdcroft, *ChemSusChem* **2023**, *16*, e202202376.

[123] A. C. Lazanas, M. I. Prodromidis, *ACS measurement science au* **2023**, *3*, 162–193.

List of Figures

1.1 Objective of the thesis 2

2.1 Overview of CO_2 electrolysis process in aqueous media . . 6
2.2 Illustrations of architecture, component position 17
2.3 Illustration of ion transport through PEM 20
2.4 Illustration of ion transport through AEM 22
2.5 Illustration of ion transport through a BPM 24
2.6 Illustration of Meander and Interdigitated flow-field. . . . 27

3.1 Flowsheet of test bench for testing cell configurations . . . 37

4.1 pH values of catholyte over the time 47
4.2 Illustration of a flow-cell assembled with a zero-gap anode, 53
4.3 (a) Images of the first generation of the current collector . . 55
4.4 FE(CO) (left) and cell voltage (right) over different λ-values 57
4.5 (a-c) Schematic illustration of the electrical resistances . . . 59
4.6 FE(CO) (left) and cell voltage (right) over different λ-values 61
4.7 Illustration of the force closure through the cell 63
4.8 Voltage measurements and averaged U_{Cell} over time 63
4.9 (a) Illustration of the current flow through the cell 65
4.10 FE(CO) (left) and U_{Cell} (right) over λ 66
4.11 Concentration of CO (φ_{CO}) (left) and concentration of CO_2 68
4.12 Illustration of the two-cell short-stack including 72
4.13 FE(CO) (left y-axis) and U_{Cell} (right y-axis) over time . . . 73
4.14 Circuit diagrams and graphs describing behavior 75

4.15 Illustration of the front and rear side of end-plates 80
4.16 (a) Illustration of the short-stack in the test bench 81
4.17 Over time at 200 mA/cm²: Cell voltage and FE(CO) 82
4.18 Over different current densities: (a) FE(CO) of single-cell . 84
4.19 (a) Electrolyte temperature in experiments with single-cell and short-stack at 200 mA/cm^2 over time, (b) electrolyte . 87
4.20 Modified short-stack with a half-plate of the bipolar plate on the adjacent side of the TC. 90
4.21 (a) Voltages obtained with modified short-stack and short-stack 91
4.22 Illustration of shunt current formation in the anolyte . . . 93
4.23 (a) UI curves at different temperatures for experiment . . . 94
4.24 (a) Illustration of three-cell short-stack, (b) Image 98
4.25 Results of experiments with short-stacks at 200 mA/cm^2 . 99
4.26 Results of experiments with single-cells at 200 mA/cm^2 . . 101
4.27 Cell voltage (left) and FE(CO) (right) for single cells containing a Ti Anode-Plate (Ti) or the Ir-MMO coated Anode plate (Ir) at 200 mA/cm^2. Comparison of experiments with 10 mM $KHCO_3$ and 100 mM $KHCO_3$ solution as anolyte. . 103
4.28 Results of experiments with short-stacks at different current densities: (a) FE(CO) of short-stacks over different current densities, (b) stack voltages over different current densities, and (c) voltages of individual cells in the short-stacks over different current densities. 105
4.29 Results of experiments with single-cells at different current densities: (a) FE(CO) of single-cells over different current densities, (b) single-cell voltages over different current densities. 107

A.1 Conductivity probe in a test tube filled with IER and 1M $KHCO_3$. The figure is adapted from [1]. 114

A.2 Measurement of temperature in the catholyte in front and behind the cell in an experiment with the cell containing Meander and the spacer. The cell operated at 100 mA/cm^2 with diluted and reduced CO_2 supply. The figure is adapted from [1]. 115
A.3 Measurement of pH in the catholyte in front and behind the cell in an experiment with the cell containing M1 and the spacer. The cell operated at 100 mA/cm^2 with diluted and reduced CO_2 supply. The figure is adapted from [1]. . 116
A.4 Flowsheet of the process design for the experiment with the stack assembly. The figure is adapted from [1]. 117

B.1 Results of 1H NMR measurements with anolyte solution. . 120
B.2 Nyquist plots obtained with single-cell at different temperatures and different current densities; (a) 100 mA/cm² at 28 °C and 30 °C, (b) 200 mA/cm² at 30 °C and 33 °C, (c) 300 mA/cm² at 33 °C and 38 °C, (d) 400 mA/cm² at 36 °C and 43 °C. The figure is adapted from [2]. 121
B.3 (a) Nyquist plots obtained with short-stack at different current densities; (b) Nyquist plots obtained at 300 mA/cm² for the individual cells in the short-stack. The figure is adapted from [2]. 122

C.1 Illustrations of (a) old and (b) new flow-field. The media flow enters old flow-field from the front side, the media flow enters the new flow-field from the rear side. 125

List of Tables

2.1 Products produced with pure CO, the chemical reaction of CO to the desired product, and the industry in which the product is used. 12

3.1 Instruments 34
3.2 Analytical materials 36

4.1 Flow-cell configurations and performances 45
4.2 GDE-flow-cell configurations and performances 69

C.1 GDE-Flow-cell stack vs. single-cell performance 124
C.2 Singe-cell with MEA performance 124
C.3 Flow-cell with MEA; stacks and single-cell performance at different j 126